

https://dspace.org/

Analysis and modelling of residence time distribution in a high speed gas reactor

Rabbitts, M C

2015-07-02
http://hdl.handle.net/10539/18044

Downloaded from a DSpace repository. https://dspace.org/

ANALYSIS AND MODELLING OF RESIDENCE TIME DISTRIBUTION IN A HIGH SPEED GAS REACTOR

M C Rabbitts

A Dissertation Submitted to the Faculty of Engineering, University of the Witwatersrand Johannesburg, for the Degree of Master of Science (Chemical Engineering)

Johannesburg, 1982

ABSTRACT

Flow patterns and the associated residence time distribution are important factors affecting the performance of a chemical reactor. This dissertation investigates the flow patterns in a scale-model of a gas reactor where opposing inlet jets are used to create mixing. The effects of different vessel geometries and gas flow-rates are investigated.

The residence time distribution (RTD) was measured by means of radioactive tracer techniques. The extremely short mean residence time in the vessel necessitated the use of sharp tracer pulses and a computerised digital recording system. Flow visualisation experiments were also performed to aid interpretation of the results.

The results were analysed using the method of frequency analysis, in which the coefficients of the Fourier Series are used to characterise the RTD curves. It was found that the shape of the RTD curve is unaffected by change in flowrate; i.e. the flow patterns are independent of flowrate over the range investigated. The geometry of the vessel however plays a major role. The effect of reducing the length/diameter ratio of the reactor is an increase in the mixedness in the vessel. Internal recirculation patterns are well-defined at a higher length/diameter ratio.

The RTD curves were also used to set up mathematical flow models. Simple multi-parameter models were used, where the vessel was viewed as consisting of interconnected flow regions such as plug flow, stirred tank, and axial dispersion. Close fits of the mathematical models to the experimental RTD curves were obtained.

DECLARATION

I declare that this dissertation is my own unaided work, and has not been submitted before for any degree or examination in any other University.



15th day of September, 1982.

ACKNOWLEDGEMENTS

I would like to thank the following people:

My supervisors, Profs D.Glasser and A.W.Bryson, for their valuable guidance and assistance.

AECI Limited, for sponsoring this work, and particularly Mr A.D. Engelbrecht and Mr G.J.van den Houten for their support during the project.

Mr L.Schwartz and Mr A.C.Harris for their excellent workmanship in the construction of the apparatus.

Mr T.L.Nam of NPRU, Wits University, and Mr I.D.Hill of AECI Limited for advice concerning the use of radioisotopes.

Mrs A.L.Theron, Mrs M.D.Knodell and Mrs J.Bowley for the production of the manuscript.

CONTENTS

CHAPTER		PAGE
1.	INTRODUCTION	1
2.	EXPERIMENTAL APPARATUS AND PROCEDURE	4
	2.1 Reactor Models	4
	2.2 Flow system	5
	2.3 Residence Time Measurement Equipment	7
	2.3.1 Selection of a Tracer	7
	2.3.2 Tracer Injection	7
	2.3.3 Tracer Monitoring System	9
	2.3.4 Statistical Errors of Radiation Measurement	13
3.	EXPERIMENTAL RESULTS	18
	3.1 Input Curves	18
	3.2 Output Curves	23
	3.3 Experimental Tail Fitting and Conversion to Dimensionless Time Units	30
	3.4 Flow Visualization	48
4.	FREQUENCY ANALYSIS	50
	4.1 Introduction	50
	4.2 Theory	51
	4.3 Results of Frequency Analysis	54
5.	MATHEMATICAL MODELS	64
	5.1 Proposed Flow Models	64
	5.2 Laplace Transforms	66
	5.3 Model Fourier Coefficients	68
	5.4 Fitting of Mathematical Models	72
	5.4.1 Least Squares Fit of Fourier coefficients	72

	5.4.2 Regeneration of the RTD Curve	73
	5.4.3 Variation of Model Parameters with Frequency	73
6.	RESULTS OF MATHEMATICAL MODEL FITTING	74
	6.1 Long Reactor	74
	6.2 Short Reactor	95
7.	CONCLUSIONS	110
NOMENCLATURE		113
REFERENCES		115
APPENDIX I :	Calibration Curves	118
APPENDIX II :	Graphs of the Output Curves for the Long Reactor	121
APPENDIX III :	Graphs of the Output Curves for the Short Reactor	132
APPENDIX IV :	Graphs of the Fourier Coefficients, Amplitude Ratio and Phase Angle for the Output Curves of the Long Reactor	143
APPENDIX V :	Graphs of the Fourier Coefficients, Amplitude Ratio and Phase Angle for the output curves of the Short Reactor	159
APPENDIX VI :	Equations associated with Normalisation and Exponential Tail Fitting of Experimental Data	175
APPENDIX VII :	Time Domain Solutions and Moments for the Mathematical Models.	177

APPENDIX VIII :	Derivation of the Fourier Coefficient Equations for the Recycle Model	185
APPENDIX IX :	Derivation of the Fourier Coefficient Equations for the Bypass Model	193
APPENDIX X :	Significance of the Shape of the Amplitude Ratio Plot of the Long Reactor	195
APPENDIX XI :	Computer Programs.	201

1. INTRODUCTION

For the design or modelling of a chemical reactor, one not only needs information describing the reaction kinetics, but also a knowledge of the flow patterns in the reactor. The flow patterns determine the length of time spent in the reactor by each element of the fluid, and are also important in determining the heat and mass transfer. The purpose of this work is to investigate the flow patterns in a scale-model of a gas reactor with a certain geometry, where opposing inlet jets are used to create mixing. The effect of flowrate on two different length vessels is investigated.

The transport of material through the vessel is governed by the conservation equations for mass, momentum and energy. With appropriate boundary conditions, these equations can in theory be solved to generate a complete velocity distribution for the fluid within the vessel. Apart from a few simple geometries, this approach generally leads to a complicated set of differential equations, where the effort expended to obtain useful solutions generally far exceeds potential benefits. This method has been applied to combustion systems by Oran (1), who concluded that the technique is limited to one dimensional systems in most cases.

The concept of residence time distribution (RTD) of the fluid in a vessel developed by Dankwerts (2) is a convenient way of characterising the overall flow behaviour in a vessel. The theory relating to residence time distributions is described in references (3), (4) and (5). The RTD curve is specially useful for diagnosing possible flow problems such as bypassing, channelling, recycling and stagnancy. Stimulus-response techniques are used to determine the residence time distribution experimentally, where the stimulus is a tracer input into the fluid entering the vessel and the response is a time record of tracer leaving the vessel. In this work a pulse input is used, as it is simple to implement and provides the most useful information. The extremely short mean residence time in the vessel (0,4 to 2 seconds) caused many

experimental problems and it was necessary to use very sharp pulses of tracer. A radio-isotope (Krypton-85) was chosen as a tracer, and a technique of automatic digital radiation counting was used to record the response at the vessel outlet.

The residence time distribution was analysed using the method of frequency analysis, in which the coefficients of the Fourier series are used to characterise the RTD curves. This technique is described in references (6) and (7). This method has also been used to analyse other transient processes (8,9).

For first order reactions, the RTD curve can be used directly to predict conversion in the reactor. For more complex reactions it is necessary to first set up a model for the flow patterns in the vessel, before an estimate of conversion can be made. The next step is therefore to fit simple non-ideal flow models to the RTD curves. Selection of a flow model is based on the physical configuration of the reactor, visual observations of the flow patterns where possible, and the shape of the RTD curve. The model is fitted to the RTD curve by comparing the theoretical model Fourier coefficients with those of the experimental RTD curve. The parameters of the theoretical flow model are varied until the closest fit between the theoretical and experimental Fourier coefficients is obtained. The method of least-squares may be used for this fitting procedure. This method of using frequency analysis for the fitting of flow models has many advantages over the more commonly used method of moments or the method of RTD curve fitting in the time domain (see section 4.1).

For vessels with complex flow patterns the ideal plug flow and stirred tank (CSTR) models, as well as the two-parameter models (e.g. axial dispersion, stirred tanks in series) which describe simple deviations from the ideal models, are inadequate. Multi-parameter models must therefore be employed. The most generally used multi-parameter models are the combined models (3,4,5,10), in which the vessel is viewed as consisting of interconnected flow regions with various types of flow in and between the regions.

Each of the individual small regions is usually restricted to one of the following: (a) plug flow, (b) perfectly mixed (CSTR), (c) axial dispersion, (d) dead space. Types of flow streams included are (a) cross flow or exchange of fluid elements, (b) by-pass flow, (c) recycle flow.

No work has previously been published on RTD models for the type of reactor used here. Clegg (11) has modelled the flow of water through a filled cylindrical vessel with one inlet jet. He used a recycle model with a number of mixed tanks in series in each loop (similar to that used here), and computed the parameters of his model by trial and error. Various types of recycle models have been used in the literature, mainly to describe mixing in stirred tanks. Gibilaro (12) gives a summary of the work done on recycle models prior to 1970. The most popular recycle model has been one with instantaneous recycle (13,14), i.e. no time delay in the recycle stream, as the analysis of this model is far simpler. Instantaneous recyle is, however, unrealistic for most flow systems. A comprehensive and more general mathematical treatment of recycle systems has recently been presented by Mann (15).

Each of the individual small regions is usually restricted to one of the following: (a) plug flow, (b) perfectly mixed (CSTR), (c) axial dispersion, (d) dead space. Types of flow streams included are (a) cross flow or exchange of fluid elements, (b) by-pass flow, (c) recycle flow.

No work has previously been published on RTD models for the type of reactor used here. Clegg (11) has modelled the flow of water through a filled cylindrical vessel with one inlet jet. He used a recycle model with a number of mixed tanks in series in each loop (similar to that used here), and computed the parameters of his model by trial and error. Various types of recycle models have been used in the literature, mainly to describe mixing in stirred tanks. Gibilaro (12) gives a summary of the work done on recycle models prior to 1970. The most popular recycle model has been one with instantaneous recycle (13,14), i.e. no time delay in the recycle stream, as the analysis of this model is far simpler. Instantaneous recyle is, however, unrealistic for most flow systems. A comprehensive and more general mathematical treatment of recycle systems has recently been presented by Mann (15).

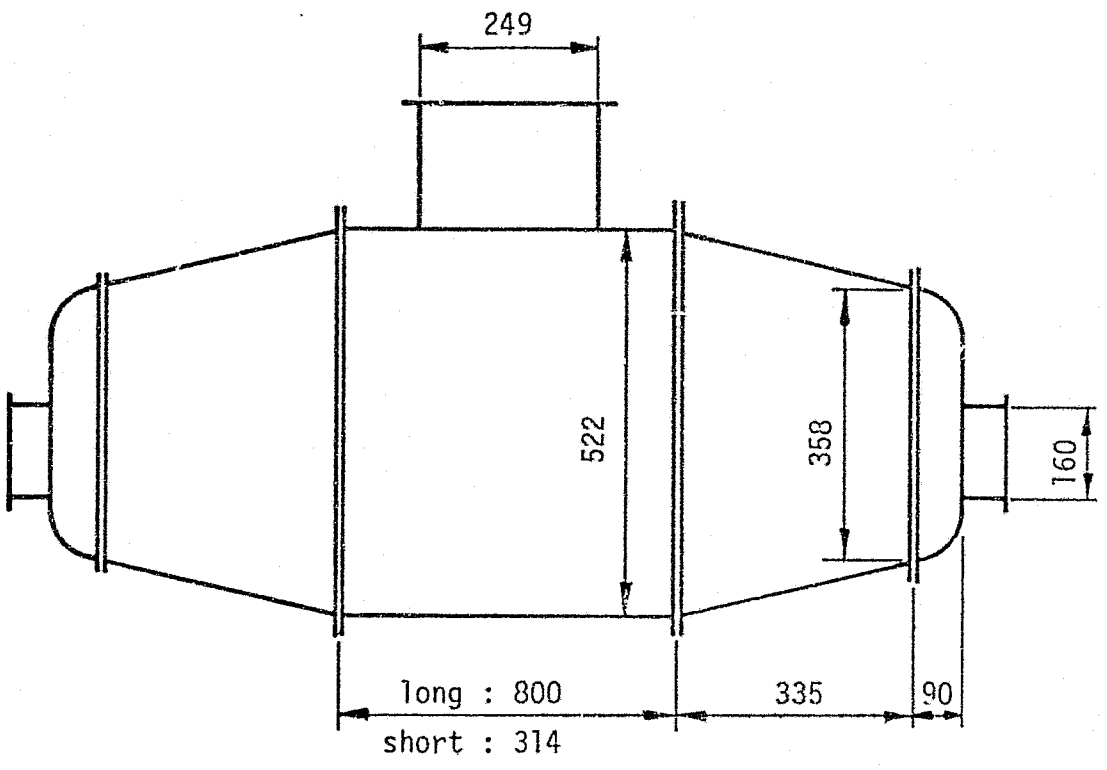
Each of the individual small regions is usually restricted to one of the following: (a) plug flow, (b) perfectly mixed (CSTR), (c) axial dispersion, (d) dead space. Types of flow streams included are (a) cross flow or exchange of fluid elements, (b) by-pass flow, (c) recycle flow.

No work has previously been published on RTD models for the type of reactor used here. Clegg (11) has modelled the flow of water through a filled cylindrical vessel with one inlet jet. He used a recycle model with a number of mixed tanks in series in each loop (similar to that used here), and computed the parameters of his model by trial and error. Various types of recycle models have been used in the literature, mainly to describe mixing in stirred tanks. Gibilaro (12) gives a summary of the work done on recycle models prior to 1970. The most popular recycle model has been one with instantaneous recycle (13,14), i.e. no time delay in the recycle stream, as the analysis of this model is far simpler. Instantaneous recyle is, however, unrealistic for most flow systems. A comprehensive and more general mathematical treatment of recycle systems has recently been presented by Mann (15).

2. EXPERIMENTAL APPARATUS AND PROCEDURE

2.1 REACTOR SCALE-MODELS

The reactor scale-model is moulded from 6mm perspex sheet. It consists essentially of a cylindrical centre section with conical end sections. Two centre sections of different lengths are used in this study. Flanged connections are provided on either end for inlet pipes and the outlet is above the centre of the vessel. The vessel dimensions are shown in figure 2.1.



Vessel volume: Long model : 288 ℓ
Short model : 184 ℓ

FIGURE 2.1. REACTOR MODEL (SIDE ELEVATION).

2.2 FLOW SYSTEM

The flow system is shown schematically in figure 2.2. A Howden L-2 fan provides the air flow of up to 20 000 m^3/h. Flowrates of between 470 and 1650 m^3/h are required for the tests, the rest being bypassed through a 34cm x 21cm rectangular duct and used for dilution of the radioactive tracer gas from the reactor. A further 30 000 m^3/h of air is used for final dilution to acceptable levels (10^{-5} $\mu Ci/cm^2$ for Kr-85) before venting to atmosphere. The air to the reactor is split into two streams in 80mm pipes, the flowrates being controlled by gate valves as well as a butterfly valve on the bypass line. The flowrate to each inlet nozzle of the model is measured by means of an orifice plate flowmeter, designed according to the British Standard (BS 1042, Part 1,1964 - see appendix I for calibration curve). A straight length of 1,4m is allowed for the inlet nozzles so as to stabilize the flow. The pipe diameter at the inlet is 105mm . The radioactive tracer gas is injected into one of the inlet nozzles at a point 30 cm upstream from the reactor.

A 500 l/min vacuum pump (Edwards ED 500) is used to draw a sample continuously at high velocity from the reactor outlet. The sample pipe is constructed so that it can traverse the cross-section of the reactor outlet in two directions. The air sample flows via a 10 mm rubber tube to the radiation detection cell where the concentration of the tracer gas is monitored. A gate valve is used to regulate the sample flowrate, which is measured by a rotameter (Appendix I). From the vacuum pump the sampled air is fed back into the main stream from the reactor to prevent escape of radioactive gas. A further sampling point is located at the entrance to the reactor so that the input pulse can also be measured, and used for correction of the output to obtain the true RTD.

Feeders are mounted on the two 76 mm pipes leading to the reactor for introducing powder/beads for the flow visualisation experiments.

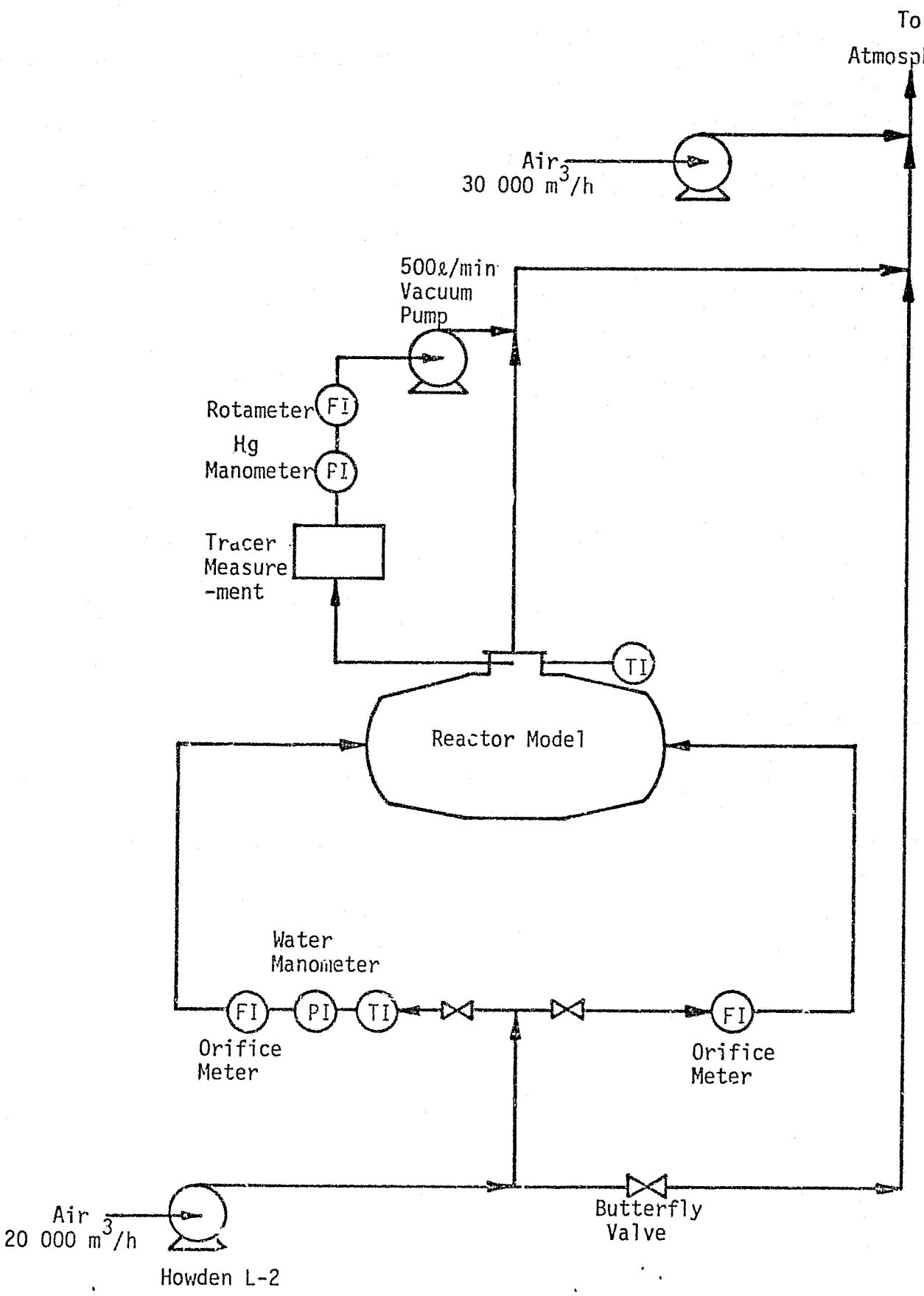


FIGURE 2.2. DIACRAM OF EXPERIMENTAL SET-UP

2.3 RESIDENCE TIME MEASUREMENT EQUIPMENT

2.3.1 Selection of a Tracer

Any material that does not disturb the flow pattern and behaves in the same way as the working fluid except that it can be detected can be used as a tracer. Radioisotopes are particularly suitable because only very small quantities are required and only negligible disturbance results. Also, because of the small quantity, very fast injection can be achieved. This is of great importance in this study where the shortest mean residence time is 0,4 seconds. Radiation measuring equipment with very fast response times can be used, which is equally important. A further advantage is that tracer concentration can be measured from outside the pipe (for γ-emitters), should this be required.

There are also many factors to be considered when selecting a suitable radio-isotope. Krypton-85 is chosen here chiefly because it is a high activity beta emitter (0,67 MeV), having only a small gamma emission. This is important from a safety aspect, as beta rays are easily absorbed by even a 6 mm perspex sheet. The disadvantage is naturally that detection of β-rays cannot take place through the wall, and sampling is necessary. The half-life of the isotope must be long enough (ten years for Kr-85) to allow storage for a sufficient period. Other important factors are the availability, price and maximum specific activity. Disposal or recovery of the isotope sometimes presents a problem. In this work in order to satisfy the emission limit a maximum of 10 mCi of krypton could be used per test.

2.3.2 Tracer Injection

High speed injection of the tracer is achieved by means of a specially constructed syringe (see Fig. 2.3). The cylinder is of

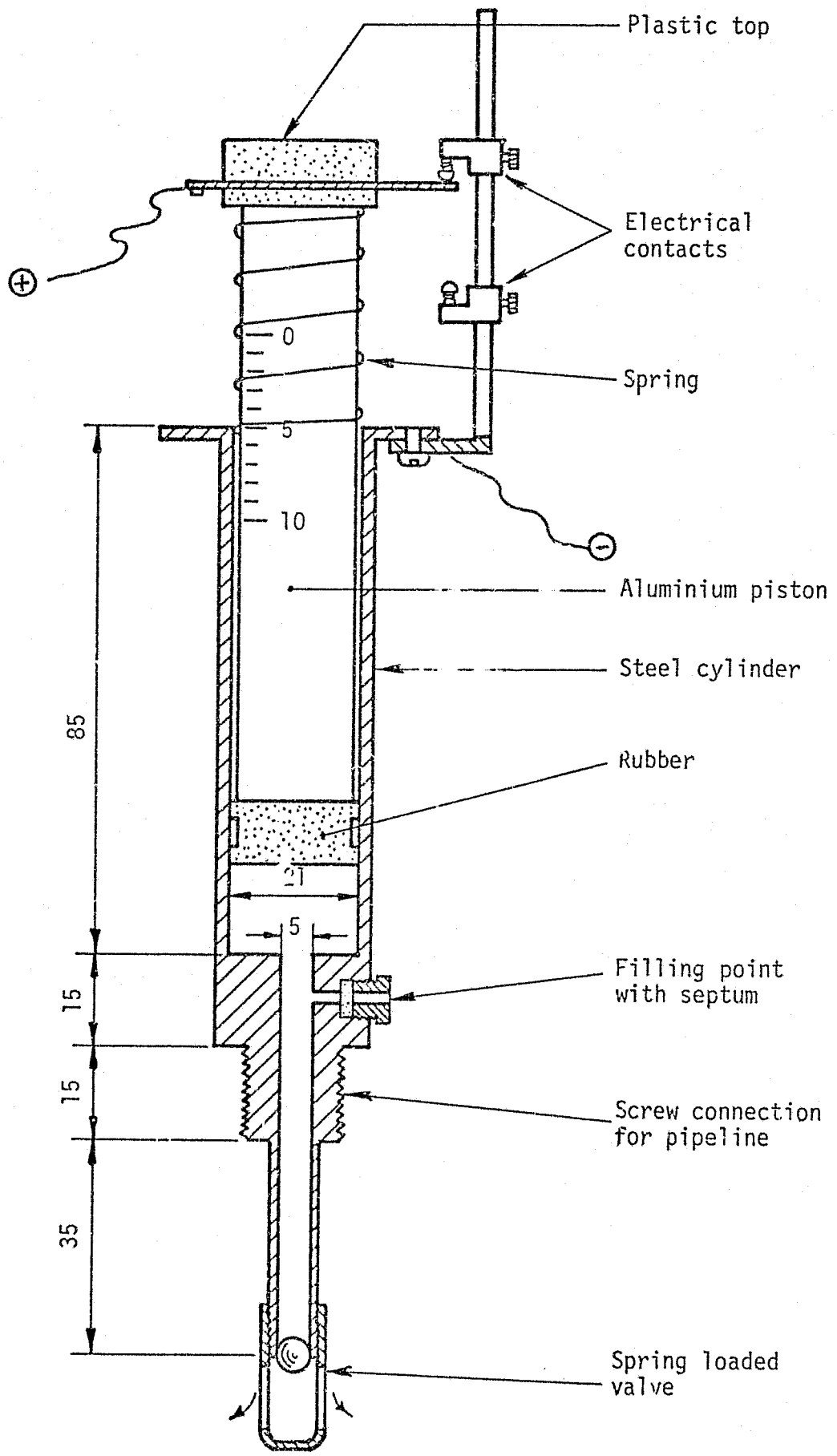


FIGURE 2.3. INJECTOR SYRINGE

steel, with a light aluminium piston and rubber seal. The syringe is mounted on the inlet nozzle, its tip extending into the centre of the pipe. The krypton gas (approx. 8 cm^3) is transferred from the atmospheric pressure storage vessel in an ordinary syringe with needle. The needle is pushed through a special rubber septum on the injector syringe for filling. A shut-off valve on the tip of the injector syringe prevents tracer from leaking into the system both before and after injection. It also helps to disperse the tracer into the air flow in the pipe.

Electrical contacts are provided for the up and down positions of the piston so as to record the time of injection as well as the duration of the piston downstroke. By keeping the length of travel of the piston short and the syringe spout wide, an acceptable injection time of five milliseconds could be achieved using a hammer stroke.

2.3.3 Tracer Monitoring System

A continuous sampling technique to monitor tracer concentration at the outlet is used, for two reasons : so that a beta emitting radio-isotope can be used, and because a detector on the outside would lack spatial resolution.

The sample is drawn through a hollow cylindrical flow cell which is machined out of plastic phosphor scintillator material (Nuclear Enterprises NE102A). The nozzles of the flow cell are offset so as to swirl the gas through the cell and thus eliminate dead space (see Fig. 2.4). The flow characteristics of the cell are shown to approximate a well-mixed vessel (CSTR), with mean residence time of between 12 and 14 milliseconds.

Two independent systems are used to monitor the concentration in the flow cell: an analogue and a digital system (see Fig. 2.5). Two photomultiplier tubes, 50 mm for the digital System and 38 mm for the analogue system, are coupled to either end of the flow

steel, with a light aluminium piston and rubber seal. The syringe is mounted on the inlet nozzle, its tip extending into the centre of the pipe. The krypton gas (approx. 8 cm^3) is transferred from the atmospheric pressure storage vessel in an ordinary syringe with needle. The needle is pushed through a special rubber septum on the injector syringe for filling. A shut-off valve on the tip of the injector syringe prevents tracer from leaking into the system both before and after injection. It also helps to disperse the tracer into the air flow in the pipe.

Electrical contacts are provided for the up and down positions of the piston so as to record the time of injection as well as the duration of the piston downstroke. By keeping the length of travel of the piston short and the syringe spout wide, an acceptable injection time of five milliseconds could be achieved using a hammer stroke.

2.3.3 Tracer Monitoring System

A continuous sampling technique to monitor tracer concentration at the outlet is used, for two reasons : so that a beta emitting radio-isotope can be used, and because a detector on the outside would lack spatial resolution.

The sample is drawn through a hollow cylindrical flow cell which is machined out of plastic phosphor scintillator material (Nuclear Enterprises NE102A). The nozzles of the flow cell are offset so as to swirl the gas through the cell and thus eliminate dead space (see Fig. 2.4). The flow characteristics of the cell are shown to approximate a well-mixed vessel (CSTR), with mean residence time of between 12 and 14 milliseconds.

Two independent systems are used to monitor the concentration in the flow cell: an analogue and a digital system (see Fig. 2.5). Two photomultiplier tubes, 50 mm for the digital System and 38 mm for the analogue system, are coupled to either end of the flow

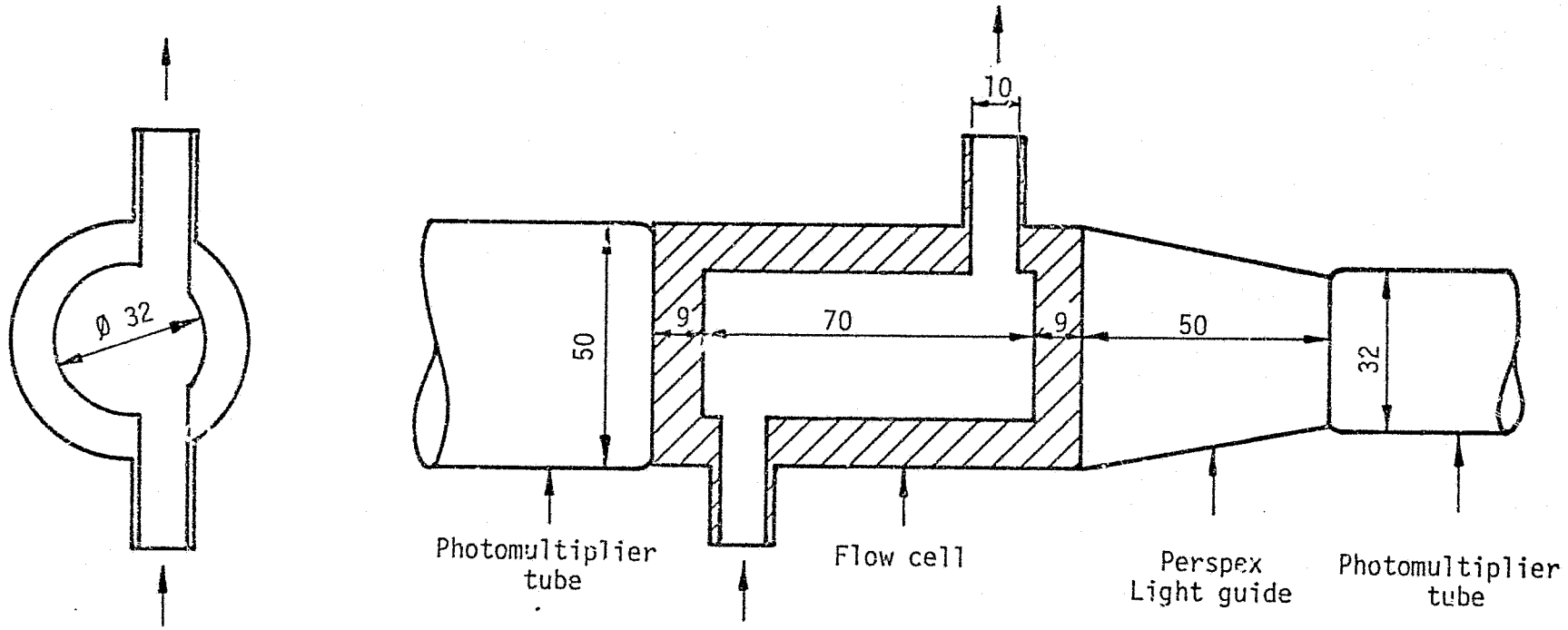


FIGURE 2.4. RADIATION DETECTION FLOW CELL

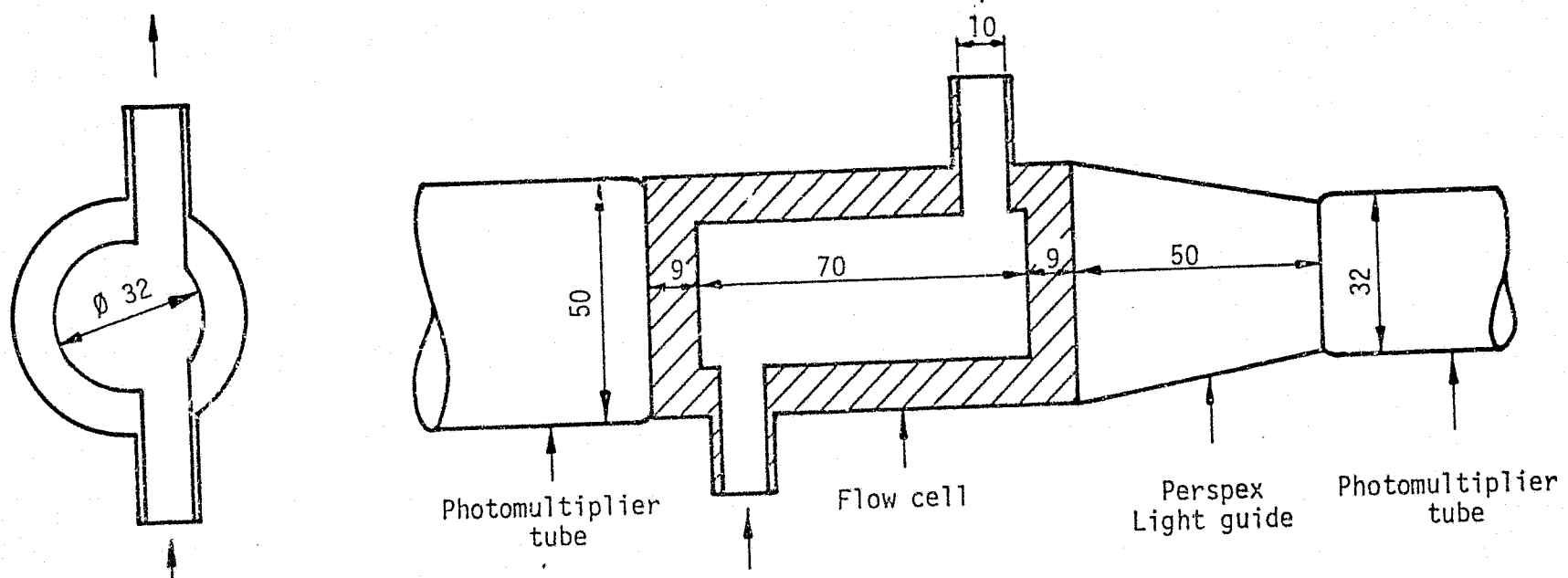


FIGURE 2.4. RADIATION DETECTION FLOW CELL

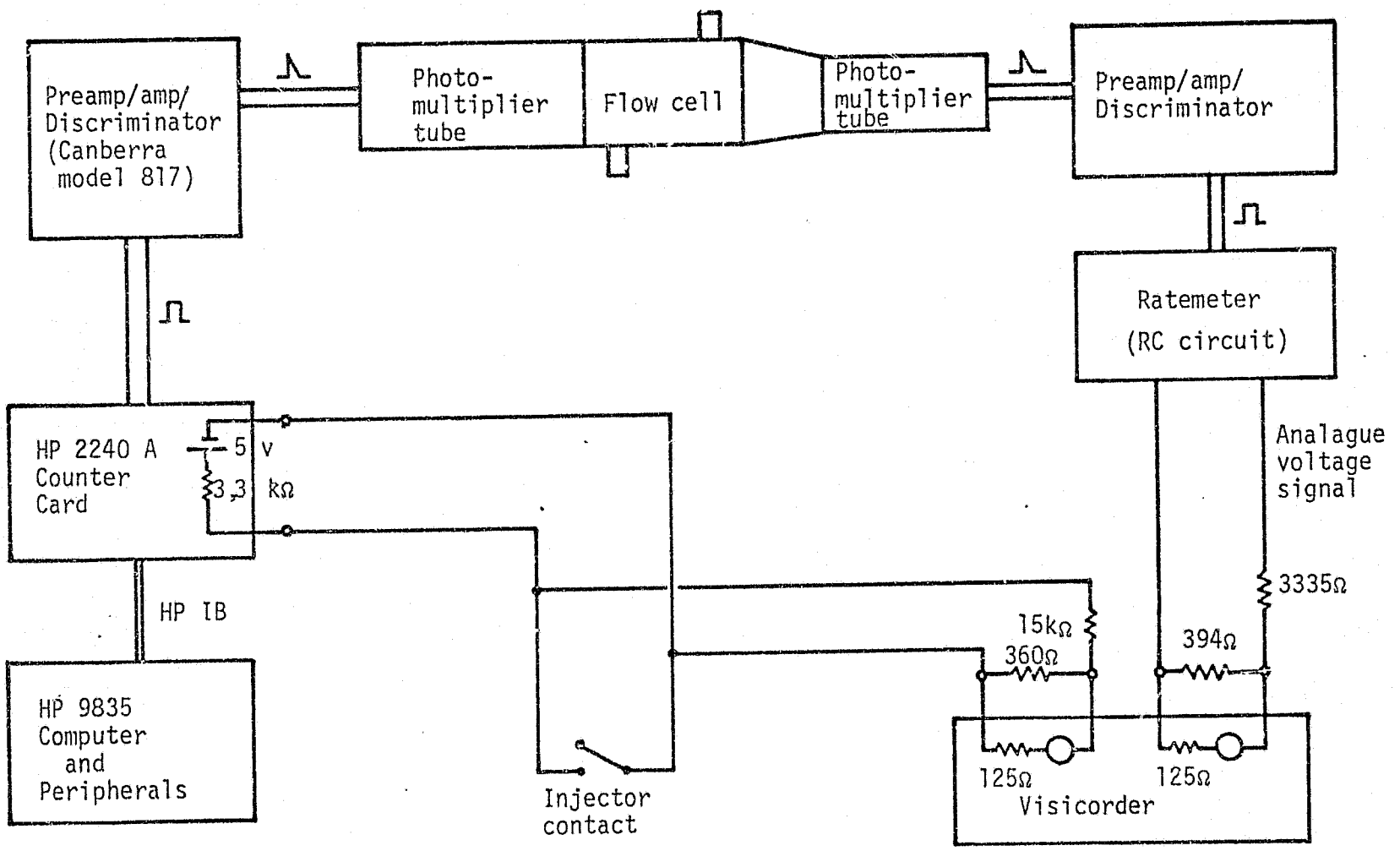


FIGURE 2.5. RADIATION MONITORING CIRCUIT

cell. A conical perspex light guide is used to reflect the scintillated light internally from the flow cell to the smaller photomultiplier, perspex having a similar refractive index (1,50) to the polyvinyl toluene (1,58) base material of the scintillator. The flat surfaces are coupled with optical grease, and the flow cell and photomultipliers are housed in a light-tight copper cylinder.

Light photons are emitted by the phosphor in the scintillator material when struck by the beta radiation. These photons are collected in the photomultiplier tubes and converted to voltage pulses which are fed into preamplifiers and amplifiers for pulse shaping and amplification. The bipolar Gaussian pulses from the amplifiers are fed into single channel pulse height analysers (or discriminators). Here most of the pulses resulting from background radiation are eliminated by accepting only pulses above a set minimum voltage. Ten volt logic pulses (positive rectangular pulses) are produced by the discriminator and fed either to a pulse counter (digital system) or a ratemeter (analogue system).

The more conventional analogue system was set up initially. The linear count-ratemeter is essentially a resistance in parallel with a capacitance which produces a continuous output of voltage proportional to the count rate of the input pulses (16,17). The ratemeter results are somewhat in error due to the first order time lag of the R-C circuit.

It can be shown (17) that for a ratemeter:

$$E_1 = E_2 + RC \frac{dE_2}{dt}$$

where E_1 is the true steady state voltage corresponding to the count rate, and E_2 is the indicated voltage. The transfer function for the ratemeter is thus:

$$F(s) = \frac{E_2(s)}{E_1(s)} = \frac{1}{1+\tau s}$$

where $\tau = RC$ (resistance x capaci ance).

The ratemeter time constant τ is adjustable and is set according to the speed of response required. The output voltage from the ratemeter is recorded on an ultra-violet recorder (Honeywell Visicorder model 2106). The connecting resistors shown in figure 2.5 are for impedance matching and optimum damping of the Visicorder galvanometer response. The Visicorder response is fast enough for the lag to be ignored. Another channel of the Visicorder is used to record the time of injection.

The heart of the digital recording system is a Hewlett-Packard 9835A desktop computer and HP 2240A Measurement and Control Processor. The processor is interfaced with the Canberra Model 817 preamplifier/amplifier/discriminator via the HP 22905A Counter/-Stepper Card. The taking of readings is thus controlled by a computer program (see Appendix XI.1). The electrical contacts of the tracer injector are connected to another channel of the Counter/Stepper Card, and the computer program arranged so that when the injector contact is broken, the gathering of readings automatically begins. The number of pulses are counted by the counter, and the total count is read repeatedly at fixed intervals, with the aid of a built-in timer in the processor. The number of readings can be varied up to 230, and the interval length can be varied according to the time scale of the experiment. The count rate can therefore be calculated which, after correction for the instrument dead-time (see Section 2.3.4), is proportional to the tracer concentration in the flow cell. Data is stored on magnetic tape and used for subsequent computations without requiring manual recording. A line-printer and x-y plotter are also connected to the computer for displaying results.

2.3.4 Statistical Errors of Radiation Detection

Due to the statistical nature of radioactive decay, there is an uncertainty associated with radiation counting. It has been

shown that a radiation count has a Poisson distribution (18) :

$$P_N = \frac{e^{-\bar{N}} \bar{N}^N}{N!}$$

where N = radiation count
(discrete stochastic variable)
$\bar{N}$ = mean of the distribution of N

The standard deviation is given by:

$$\sigma = \sqrt{\bar{N}}$$

Therefore, the interval N + 1,65 has a confidence level of 90% (18); i.e. we are 90% confident that the percentage error of a reading will be within:

$$\pm \frac{1{,}65\sqrt{\bar{N}}}{\bar{N}} 100\%$$

$$\approx \pm \frac{165}{\sqrt{R\,\Delta t}} \% \qquad (2.1)$$

where R = count rate
Δt = count interval (for digital system)
Δt = 2 x ratemeter time constant (for analogue system).

Equation (2.1) clearly shows that a compromise must be made between accuracy and speed of response. For greater statistical accuracy t must be made large, but this results in a slower response with a smoothening out of some detail in the curve.

A further error associated with radiation detection is what is known as the dead time of the instruments (18). This is due to the effect of two or more pulses arriving so close together that they are seen as one pulse by either the amplifier or the counter. Effectively, the counter is "dead" for a period corresponding to

the length of one pulse. Therefore, over a period of one second, the counter will be dead for $r\,\tau_D$ seconds, and receptive for $(1 - r\,\tau_D)$ seconds.

Therefore,

$$R = \frac{r}{1 - \tau_D\, r}$$

where R = true count rate
r = observed count rate
τ_D = dead time

The effect of dead time is thus to produce a non-linear response, but it can easily be corrected for (in program "READ"), once the dead time is known.

The two-source test is used to determine the dead time. In this test, one radiation source is placed close to the detector and the count rate measured (r_A). A second source is then also placed near the detector without disturbing the first source and the combined count rate measured (r_{AB}).

The first source is then removed without disturbing the second source and the count rate from the second source measured (r_B). The background count rate is also measured with both sources removed (r_b).

The subscripts refer as follows:

A - source A
B - source B
AB - both sources A and B
b - background radiation

The following equations can thus be written :

$$R_A = \frac{r_A}{1 - r_A\tau_D} - R_b$$

$$R_B = \frac{r_B}{1 - r_A\tau_D} - R_b$$

$$R_{AB} = \frac{r_{AB}}{1 - r_{AB}\tau_D} - R_b$$

$$R_b = \frac{r_b}{1 - r_b\tau_D}$$

$$R_{AB} = R_A + R_B$$

Therefore

$$\frac{r_{AB}}{1 - r_{AB}\tau_D} = \frac{r_A}{1 - r_A\tau_D} + \frac{r_B}{1 - r_B\tau_D} - \frac{r_b}{1 - r_b\tau_D}$$

The above equation can now be solved for τ_D.

When repeating the above τ_D measurement at different count rates, the calculated value of τ_D remained constant, showing that the corrected count rate is linear with source activity (or tracer concentration).

The amplifier used in the analogue system showed a dead time of 26.5×10^{-6} seconds. Because of this long dead time, this system could only be used for count rates up to about 10 000 counts per second, for which the statistical error is still too great (eq 2.1). The analogue system was therefore only used to check the digital system during commissioning of the latter, and to measure the computer delay time between injection of the tracer and the start of the reading cycle.

The dead time of the digital system was $1{,}85 \times 10^{-6}$ seconds, allowing count rates of up to 150 000 counts per second to be used. It

was found that the best compromise between accuracy and speed of response was then made with a reading interval Δt such that 230 readings were taken in a period of 6,5 times the mean residence time. With this system the statistical error was reduced to values comparable with other errors in the system.

3. EXPERIMENTAL RESULTS

Input and output curves were recorded at five different flowrates (denoted as runs 1 to 5 in the following) for each of the two different lengths of the reactor.

3.1 INPUT CURVES

The input curves were recorded by simply shifting the sampling point to the vessel inlet, the opening of the sample pipe being placed in the centre of the vessel inlet nozzle, downstream of the injection syringe. The input curves are the same for the two reactor lengths, as the same set of flowrates are used in both. The flowrates used are tabulated in tables 3.1 and 3.2.

TABLE 3.1. REACTOR FLOWRATES

RUN	ORIFICE ΔP ($cm\ H_2O$)	ORIFICE P UPSTREAM ($cm\ H_2O$)	ORIFICE T (°C)	REACTOR $\dot{V}$ TOTAL (m^3/h)	NOZZLE VELOCITY (m/s)
1	85	56,5	32	1650	26,4
2	60	39,8	34	1380	22,0
3	30	25,0	29	972	15,6
4	15	16,4	28	686	11,0
5	7	10,5	28	469	7,5

There are two time delays associated with the recording of the input and output curves, viz. the time taken for the pulse of tracer to travel down the inlet pipe from its point of injection, and the time taken for the sampled gas to reach the detection flow cell from the sampling point. All flowrates and time delays are

calculated in the program "READ" (Appendix XI). The time delays are based on the average velocities in the pipes, and are summarised in table 3.3

TABLE 3.2. SAMPLING FLOWRATES

RUN	ROTAMETER READING	ROTAMETER P (cm Hg)	ROTAMETER T (°C)	SAMPLE PIPE v (m/s)	FLOWCELL $\dot{V}$ (m^3/h)
1	23	7,2	31	55,8	16,6
2	23	7,2	32,5	56,2	16,7
3	23	7,4	28	55,8	16,6
4	20	5,7	27	48,9	14,4
5	20	5,8	26	48,8	14,3

TABLE 3.3. TIME DELAYS

RUN	NOZZLE DELAY TIME (sec)	SAMPLE PIPE DELAY TIME (sec)	TOTAL DELAY TIME (sec)	FLOW CELL MEAN RESIDENCE TIME (sec)
1	0,0114	0,0111	0,0224	0,0122
2	0,0136	0,0110	0,0246	0,0121
3	0,0193	0,0111	0,0303	0,0122
4	0,0273	0,0126	0,0400	0,0141
5	0,0399	0,0127	0,0526	0,0141

As described in section 2.3.3, the radiation count rates are calculated in program "READ" by reading the total count rate repeatedly at fixed intervals. Each count rate is then associated with a time corresponding to the middle of that reading interval. Radiation counting begins at time zero and thus the first reading is at a time of one half of an interval. The time scale is corrected in the program by subtracting the total delay time from the time of the first reading. A further correction is made by adding 20 milliseconds to the time of the first reading; this is the measured execution time of the program from the instant when the injector contact is broken till the counting begins.

In order that the high frequency content of the output signal is not lost, the input pulse must be as sharp as possible, i.e. as close as possible to an ideal impulse. For this reason, the distance between the injector and the vessel is kept short (300 mm) and the sampling pipe is kept as short as possible (618 mm).

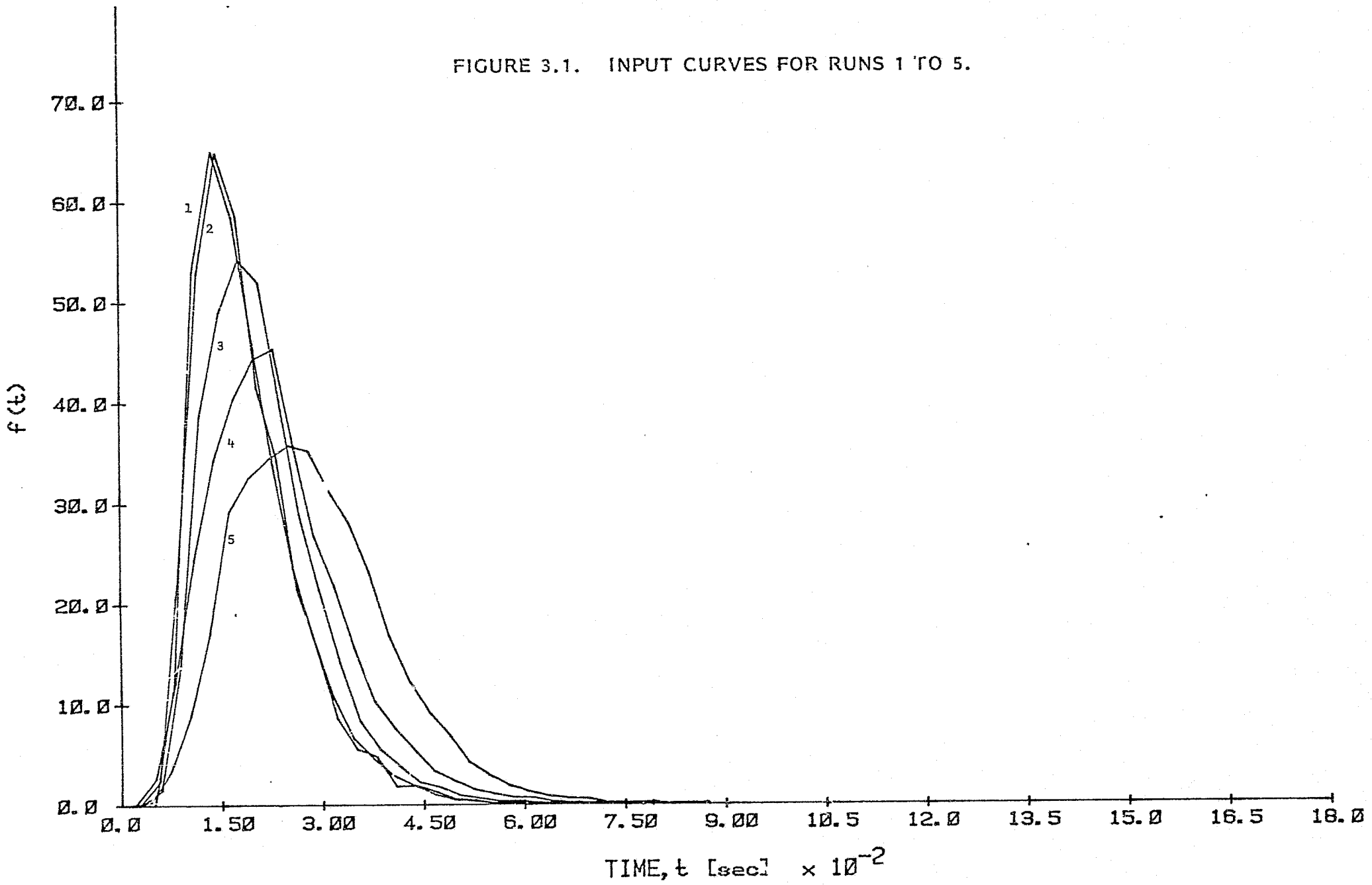
At each flowrate three recordings of the input count rate vs time curve are made. Intervals of 3 msec between readings are used to achieve a fast enough response. After subtraction of the background count rate, the curves are normalised with respect to the Y axis (i.e. unity area under the curve). The three curves are then averaged, to reduce the statistical error associated with the radiation counting (see program "RTD-AV", appendix XI.2). Reproducibility was good and three curves are found to be sufficient to produce a good average. The averaged input curves (with corrected time scales) are shown in figure 3.1 and the calculated means and variances in table 3.4.

TABLE 3.4. CHARACTERISTICS OF INPUT CURVES

RUN	MEAN τ_{in} (sec)	VARIANCE σ_{in}^2 (sec^2)
1	0,0189	$5,8 \times 10^{-5}$
2	0,0190	$5,8 \times 10^{-5}$
3	0,0212	$6,9 \times 10^{-5}$
4	0,0234	$1,00 \times 10^{-4}$
5	0,0285	$1,28 \times 10^{-4}$

Besides accounting for dispersion in the inlet and sampling pipes, the "input" curves also include the effect of the detection flow cell (see par. 2.3.3). In figure 3.1 it can be seen how the variance of the input curves increases as the flowrate decreases, due to increased dispersion in the inlet pipe. Dispersion in the sample pipe has negligible effect ($\sigma^2 \simeq 1,7 \times 10^{-6}$ sec^2; $\sigma \simeq 1,3$ msec). For runs 1 and 2 the shapes of the input curves are due mainly to the flow cell response, and for the higher flowrates the inlet dispersion effect plays a greater role.

FIGURE 3.1. INPUT CURVES FOR RUNS 1 TO 5.



3.2 OUTPUT CURVES

The output (response) curves are recorded by sampling in the centre of the reactor outlet. By traversing the outlet in two directions with the sample pipe, it is found that its position has little effect on the results and sampling in the centre provides a good average. Information on the flowrates used is given in Tables 3.1 to 3.3. The method of correction for time delays is the same as for the input curves (section 3.1).

In the case of the long reactor model, about five recordings of the output curve are made at each flowrate, and about eight in the case of the short reactor. After subtraction of the background count rate the curves are normalised to unity area under the curve. The individual output curves are given in Appendix 2 for the long reactor and Appendix 3 for the short reactor and examples of these are reproduced in Figures 3.2 and 3.3. Graphs of the mean output curve and standard deviation between curves are also given in the Appendices. In these curves, each discrete reading is joined by straight lines. It can be seen from Figures 3.2 and 3.3 that the output curves are scattered, and the necessity for averaging is obvious. This scatter of the data can be attributed to large-scale fluctuating eddies in the vessel, i.e. a deviation from true steady-state conditions. The curves for the short reactor are more scattered, which is why it was necessary to average more curves. As would be expected, the standard deviation is greatest at points where the output curve has the highest slope, i.e. at the initial sharp drop after the first peak (see e.g. Fig II.8). The process of averaging also reduces the statistical error of radiation counting, which becomes relatively large for the low count rates in the tail region of the curve.

FIGURE 3.2. OUTPUT CURVES - LONG REACTOR RUN 4.

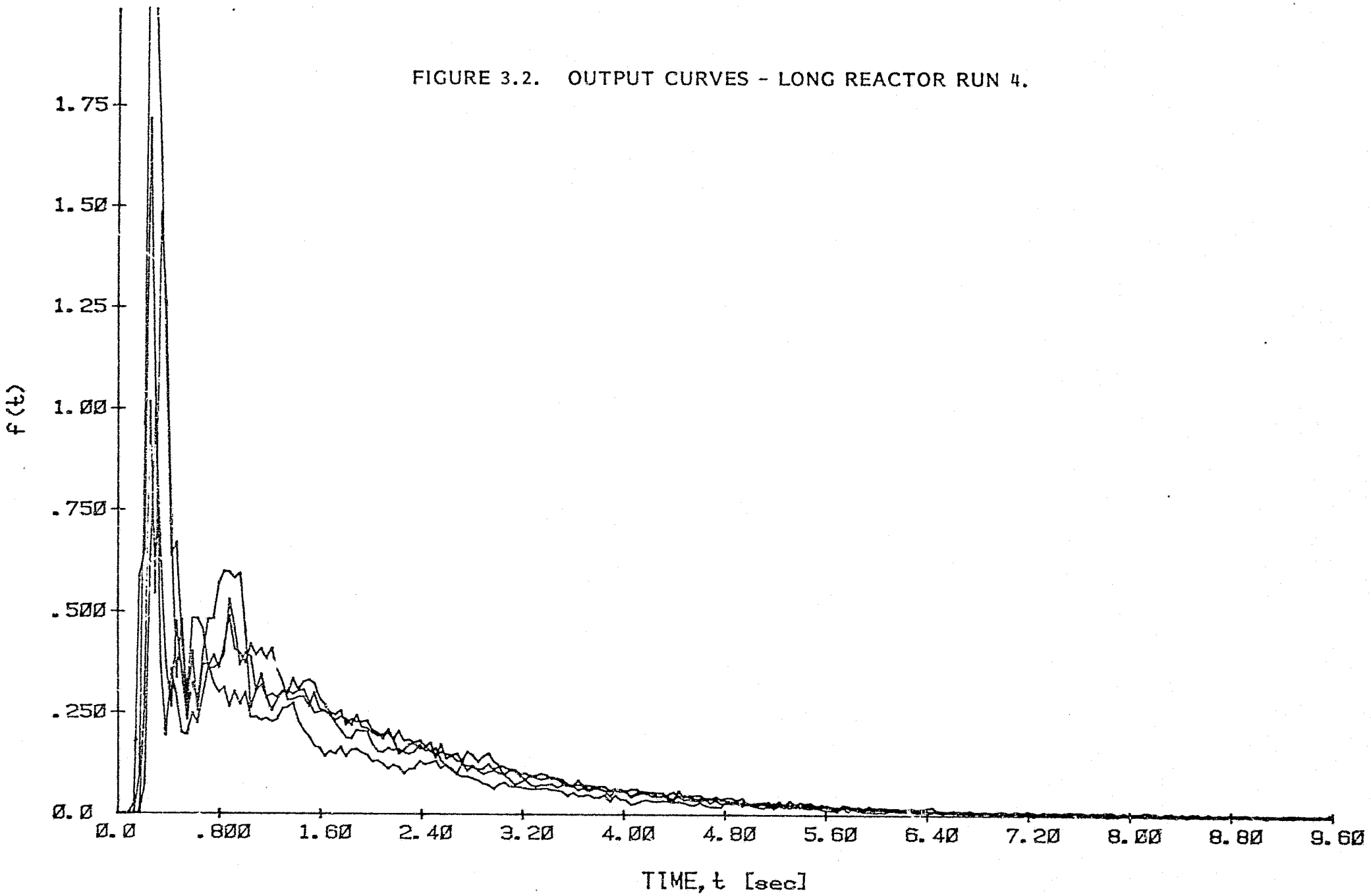


FIGURE 3.3. OUTPUT CURVES - SHORT REACTOR RUN 4.

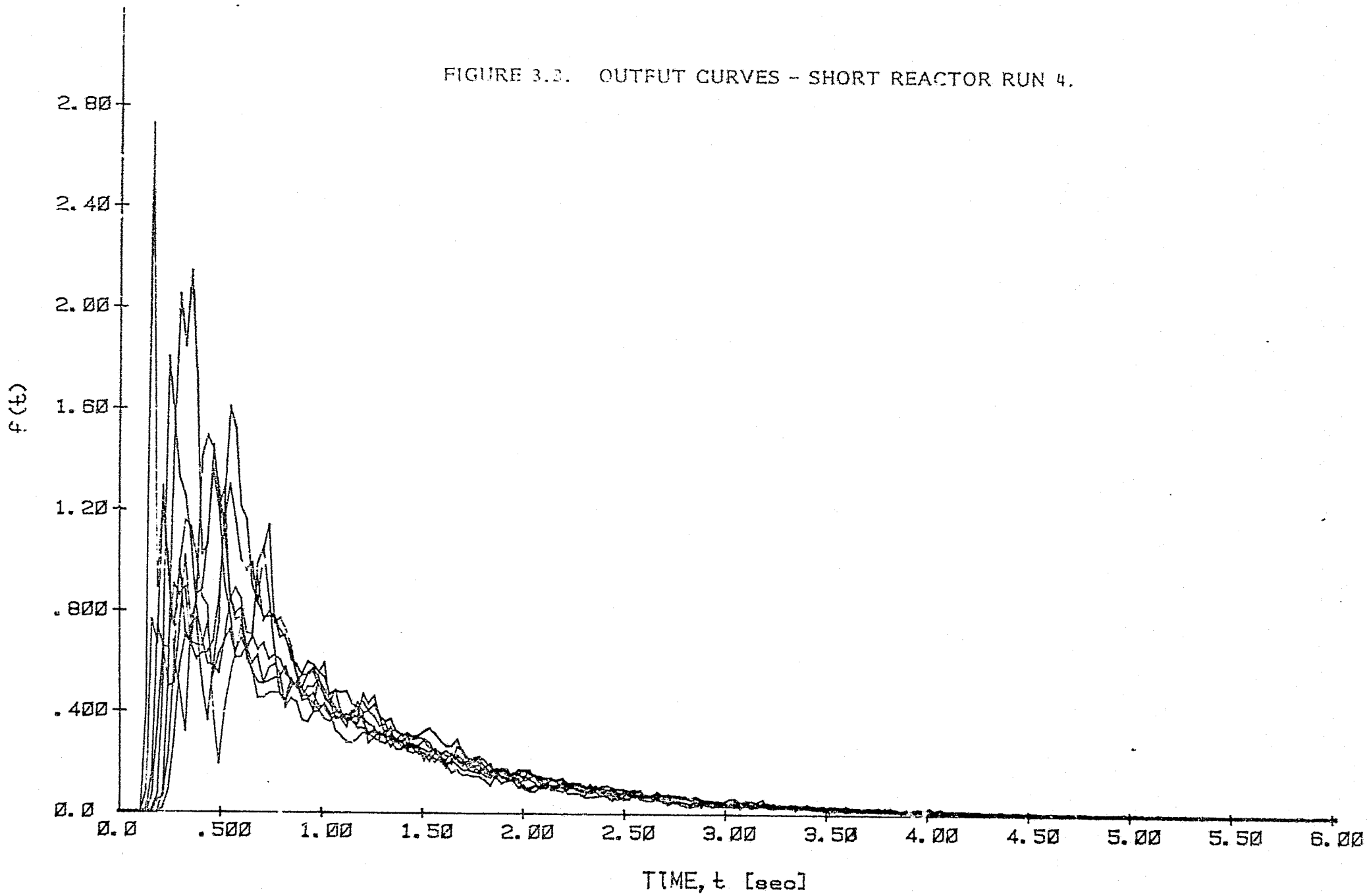


TABLE 3.5. CHARACTERISTICS OF THE OUTPUT CURVES OF THE LONG REACTOR

RUN	CORRECTED TIME OF FIRST READING (sec)	READING INTERVAL (sec)	NUMBER OF READINGS	Re	V/V̇ (sec)
1	0,00775	0,02037	245	31 800	0,63
2	0,00552	0,02037	245	26 100	0,75
3	0,00446	0,02961	230	18 900	1,07
4	0,00095	0,04183	230	13 300	1,51
5	-0,00202	0,06113	230	9 150	2,21

RUN	τ_{out} (sec)	σ_{out}^2 (sec^2)	$\bar{\tau}$ $(=\tau_{out}-\tau_{in})$ (sec)	AREA UNDER FIRST PEAK
1	0,620	0,279	0,601	0,36
2	0,828	0,531	0,809	0,30
3	1,213	1,153	1,192	0,29
4	1,593	2,054	1,570	0,28
5	2,266	4,494	2,238	0,34

The main characteristics of the average output curves are summarised in tables 3.5 and 3.6. The Reynolds number is calculated on the average vessel cross-sectional area and based on one side of the vessel. The reading intervals are selected such that 230 readings are taken over a period of about 6,5 times the mean residence time, for reasons discussed in section 2.3.4. The mean and variance of the output curves (τ_{out} and σ_{out}^2) are calculated by numerical integration. The mean residence time ($\bar{\tau}$) which is given by the difference between the means of the output and input

curves, is seen to be fairly close to the value predicted by (vessel volume)/(flowrate), though the former value is an average of 4% higher for the long reactor and 9% higher for the short reactor.

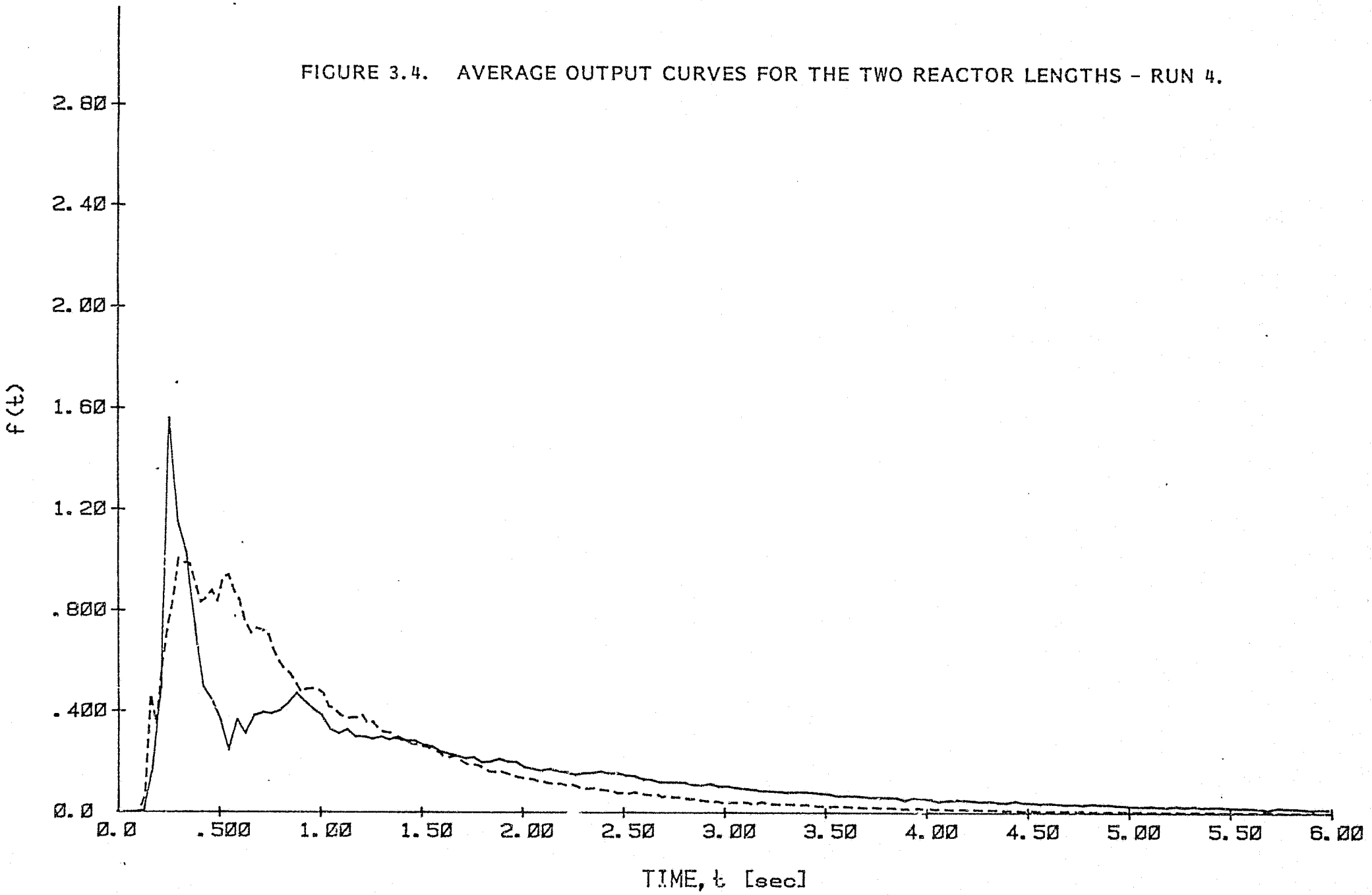
TABLE 3.6. CHARACTERISTICS OF THE OUTPUT CURVES OF THE SHORT REACTOR

RUN	CORRECTED TIME OF FIRST READING (sec)	READING INTERVAL (sec)	NUMBER OF READINGS	Re	$\dot{V}/V$ (sec)
1	0,00317	0,01115	230	33 300	0,40
2	0,00253	0,01426	230	27 800	0,48
3	-0,00060	0,01939	230	19 800	0,68
4	-0,00625	0,02750	230	13 950	0,96
5	-0,00261	0,04078	230	9 610	1,41

RUN	τ_{out} (sec)	σ_{out}^2 (sec^2)	τ ($=\tau_{out}-\tau_{in}$) (sec)
1	0,441	0,125	0,422
2	0,554	0,173	0,535
3	0,790	0,360	0,769
4	1,041	0,673	1,018
5	1,588	1,518	1,560

The average output curves in appendices II and III show that the shape of the response curves are affected drastically by vessel length. Figure 3.4 shows examples of these curves for the two

FIGURE 3.4. AVERAGE OUTPUT CURVES FOR THE TWO REACTOR LENGTHS - RUN 4.



reactor lengths plotted on the same axes, for the same flowrate (run 4). It can immediately be seen that in the case of the long reactor the RTD curve shows a series of peaks (two can clearly be seen), whilst the short reactor (dotted lines) has a smoother curve. The curves are however very similar for a particular reactor at different flowrates. This will be discussed fully in the next section.

3.3 EXPONENTIAL TAIL FITTING AND CONVERSION TO DIMENSIONLESS TIME UNITS

The natural logarithm of the output curves closely approximates a straight line from about twice the mean residence time onwards, as is shown for two runs in figures 3.5 and 3.6. This effect is to be expected from RTD curves of vessels with some mixing. An exponential curve of the form

$$f(t) = c \exp(-bt)$$

is therefore fitted to the tail of each output curve, from twice to six times the mean residence time. c and b are calculated from the intercept and slope of the ln f(t) vs t curves (see appendices VI and XI.3). The advantage of the tail fitting is to eliminate the noise associated with the low radiation count rates in the tail region.

After the exponential tail fitting, the output curves are again normalised to unit area under the curve, and then converted to dimensionless time units (denoted by θ, where $\theta = t/\tau$). Correction for background, exponential tail fitting, normalisation, and plotting of curves in done in computer program "NORM" (appendix XI.3), and the relevant equations are given in appendix VI. Some results are given in tables 3.7 to 3.10.

By comparing tables 3.7 and 3.8 with tables 3.5 and 3.6, it can be seen that the mean and variance of the output curves are increased by the exponential tail fitting. This is to be expected, as the integrals are now evaluated to infinity. The difference is greater for the variance, and would be even more pronounced for higher moments.

The dimensionless output curves of all runs are given in figures 3.7 to 3.16. The curves are truncated at θ=6, by which time the curve has dropped to about 0,001 of its maximum value and we have approx 99.9% of the total area under the curve.

FIGURE 3.5. LOG OF OUTPUT CURVE - LONG REACTOR RUN 3.

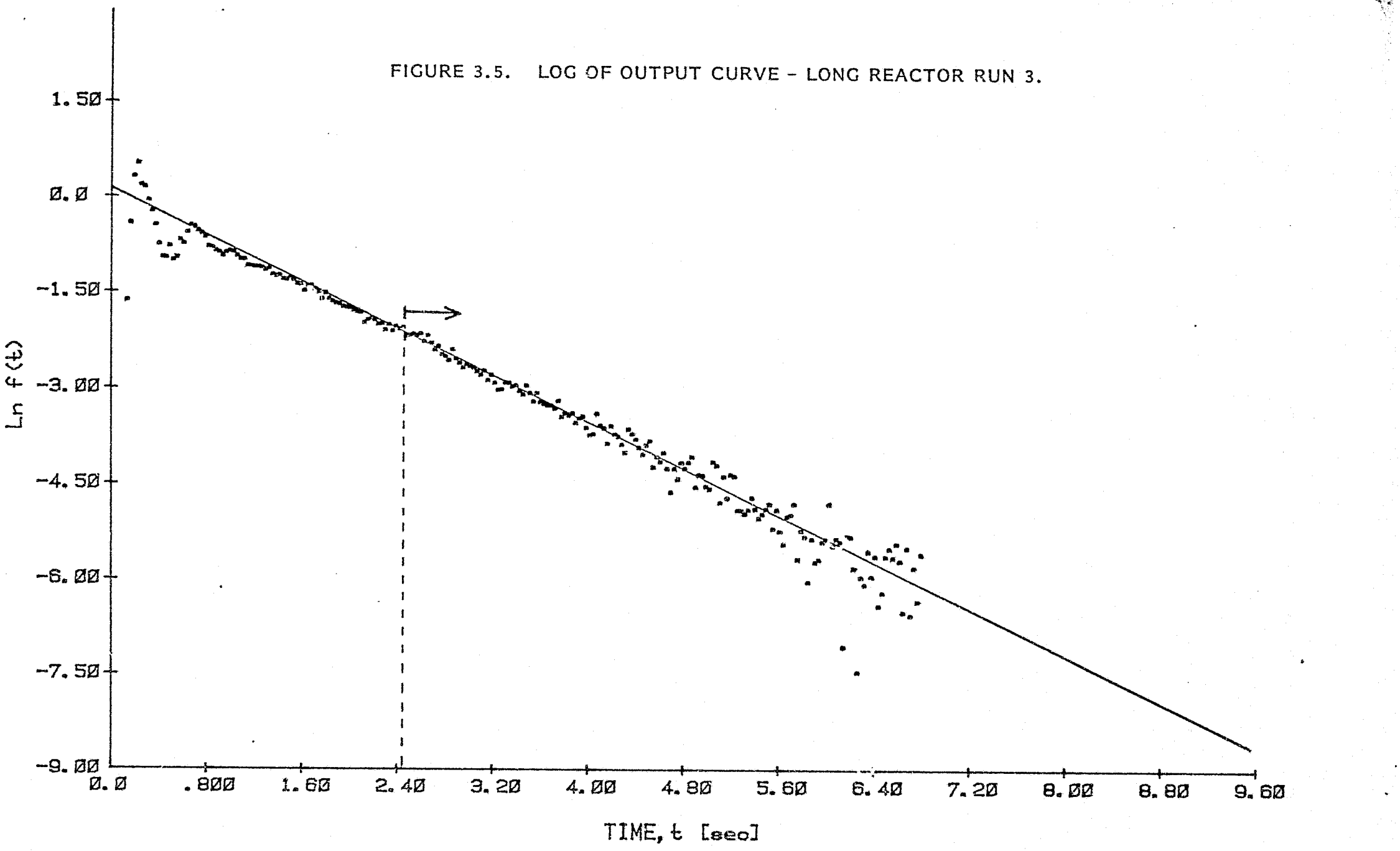


FIGURE 3.6. LOG OF OUTPUT CURVE - SHORT REACTOR RUN 3.

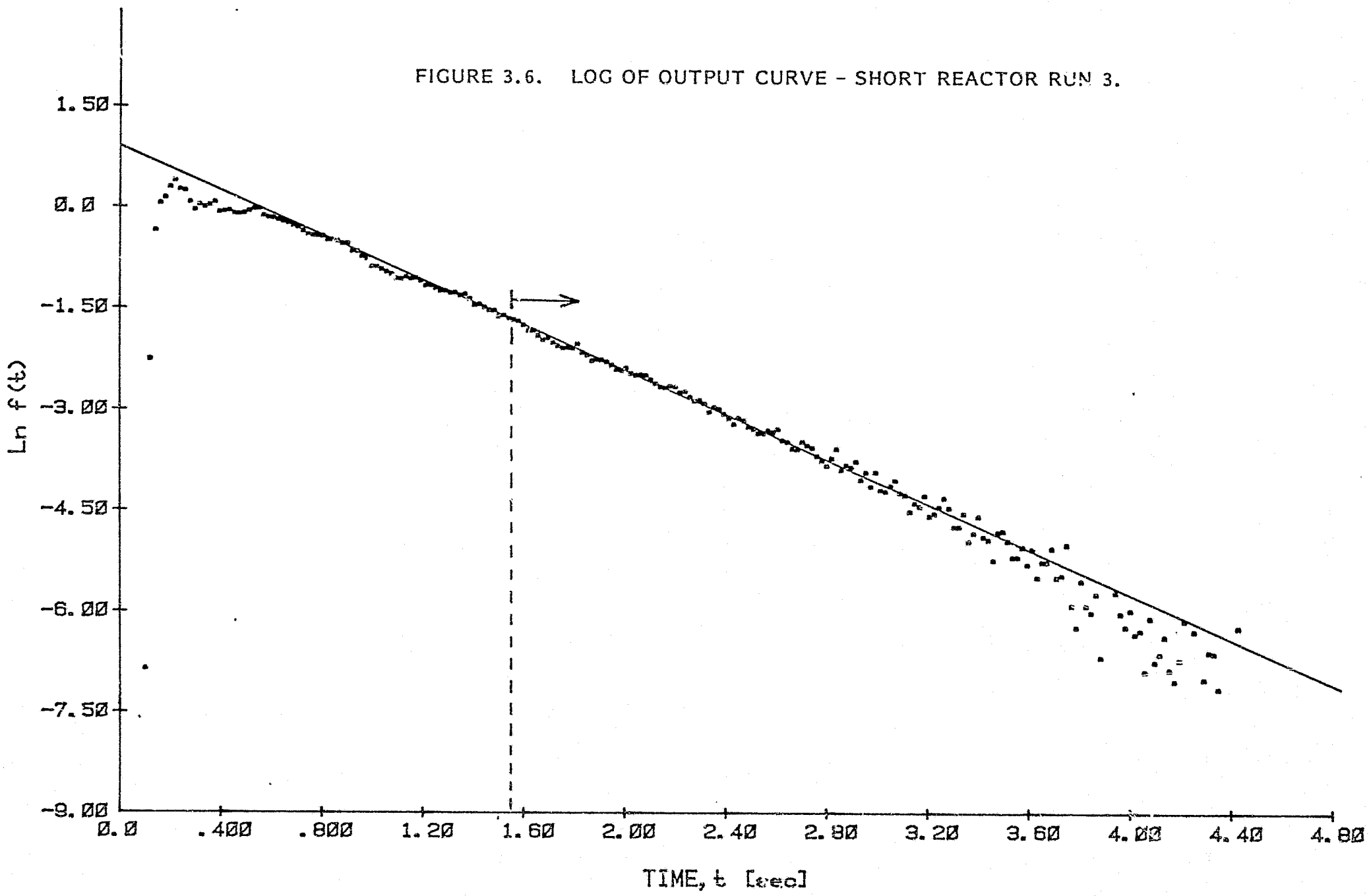


TABLE 3.7. EXPONENTIAL TAIL FITTING - LONG REACTOR

RUN	EXPONENTIAL TAIL (NORMALISED)		NEW VALUES FOR			$\frac{\sigma^2}{\tau^2}$
	b(sec^{-1})	c	τ_{out} (sec)	σ_{out}^2 (sec^2)	τ (sec)	
1	1,607	1,675	0,650	0,380	0,631	0,954
2	1,296	1,456	0,849	0,601	0,830	0,872
3	0,919	1,137	1,239	1,280	1,218	0,863
4	0,632	0,651	1,650	2,465	1,627	0,931
5	0,448	0,470	2,309	4,997	2,281	0,960

TABLE 3.8. EXPONENTIAL TAIL FITTING - SHORT REACTOR

RUN	EXPONENTIAL TAIL (NORMALISED)		NEW VALUES FOR			$\frac{\sigma^2}{\tau^2}$
	b(sec^{-1})	c	τ_{out} (sec)	σ_{out}^2 (sec^2)	τ (sec)	
1	2,773	3,676	0,446	0,136	0,427	0,746
2	2,369	3,430	0,562	0,188	0,543	0,638
3	1,658	2,361	0,795	0,384	0,774	0,640
4	1,160	1,400	1,049	0,720	1,026	0,684
5	0,804	1,133	1,605	1,631	1,577	0,656

TABLE 3.9. CHARACTERISTICS OF DIMENSIONLESS OUTPUT CURVES - LONG REACTOR

RUN	EXPONENTIAL TAIL (DIMENSIONLESS)		AREA UNDER CURVE UP TO $\theta=6$	$\frac{f(\theta=6)}{f(\theta)_{max}}$
	b	c		
1	1,045	1,089	0,9980	0,0010
2	1,100	1,236	0,9985	0,0009
3	1,139	1,409	0,9986	0,0008
4	1,043	1,075	0,9980	0,0008
5	1,035	1,086	0,9979	0,0008

TABLE 3.10. CHARACTERISTICS OF DIMENSIONLESS OUTPUT CURVES - SHORT REACTOR

RUN	EXPONENTIAL TAIL (DIMENSIONLESS)		AREA UNDER CURVE UP TO $\theta=6$	$\frac{f(\theta=6)}{f(\theta)_{max}}$
	b	c		
1	1,184	1,570	0,9989	0,0010
2	1,286	1,862	0,9994	0,0008
3	1,283	1,827	0,9993	0,0008
4	1,190	1,437	0,9991	0,0011
5	1,267	1,787	0,9993	0,0009

In figures 3.17 and 3.18 the output curves of each reactor are

plotted on one set of axes. It can be seen that in dimensionless time units the curves correspond closely, and that the differences between them are random. The dimensionless variances (tables 3.7 and 3.8) at the different flowrates also do not differ greatly. One can thus draw the conclusion that the flow patterns in the vessel are independent of flowrate over the range investigated; in other words a change in flowrate only changes the time scale of the system. The flow is turbulent for all runs done here, as can be seen from the Reynolds numbers in tables 3.5 and 3.6. It is expected that only at much lower flowrates, in the laminar flow regime, will the flow patterns be different.

FIGURE 3.7. DIMENSIONLESS OUTPUT CURVE - LONG REACTOR RUN 1.

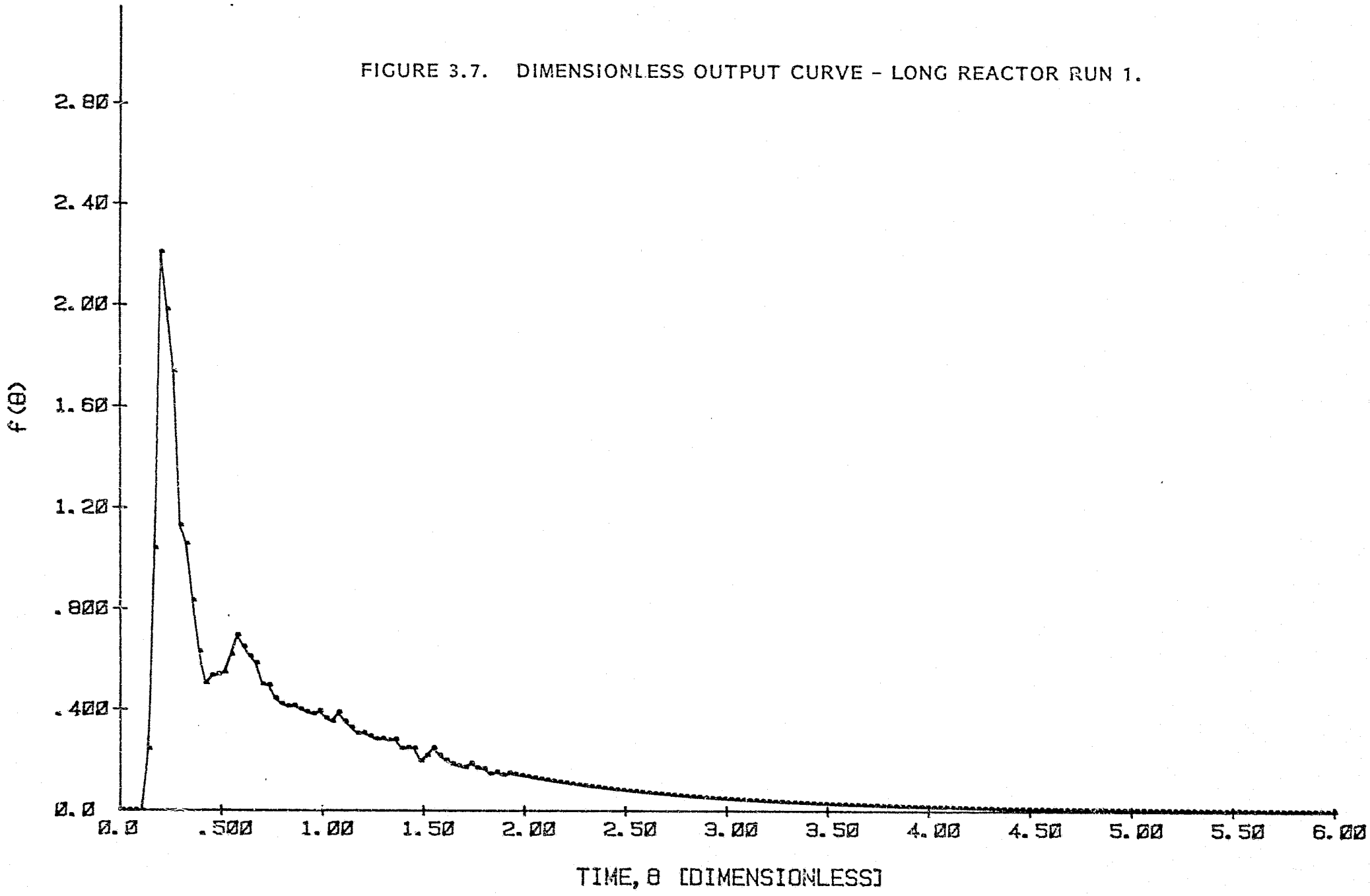


FIGURE 3.8. DIMENSIONLESS OUTPUT CURVE - LONG REACTOR RUN 2.

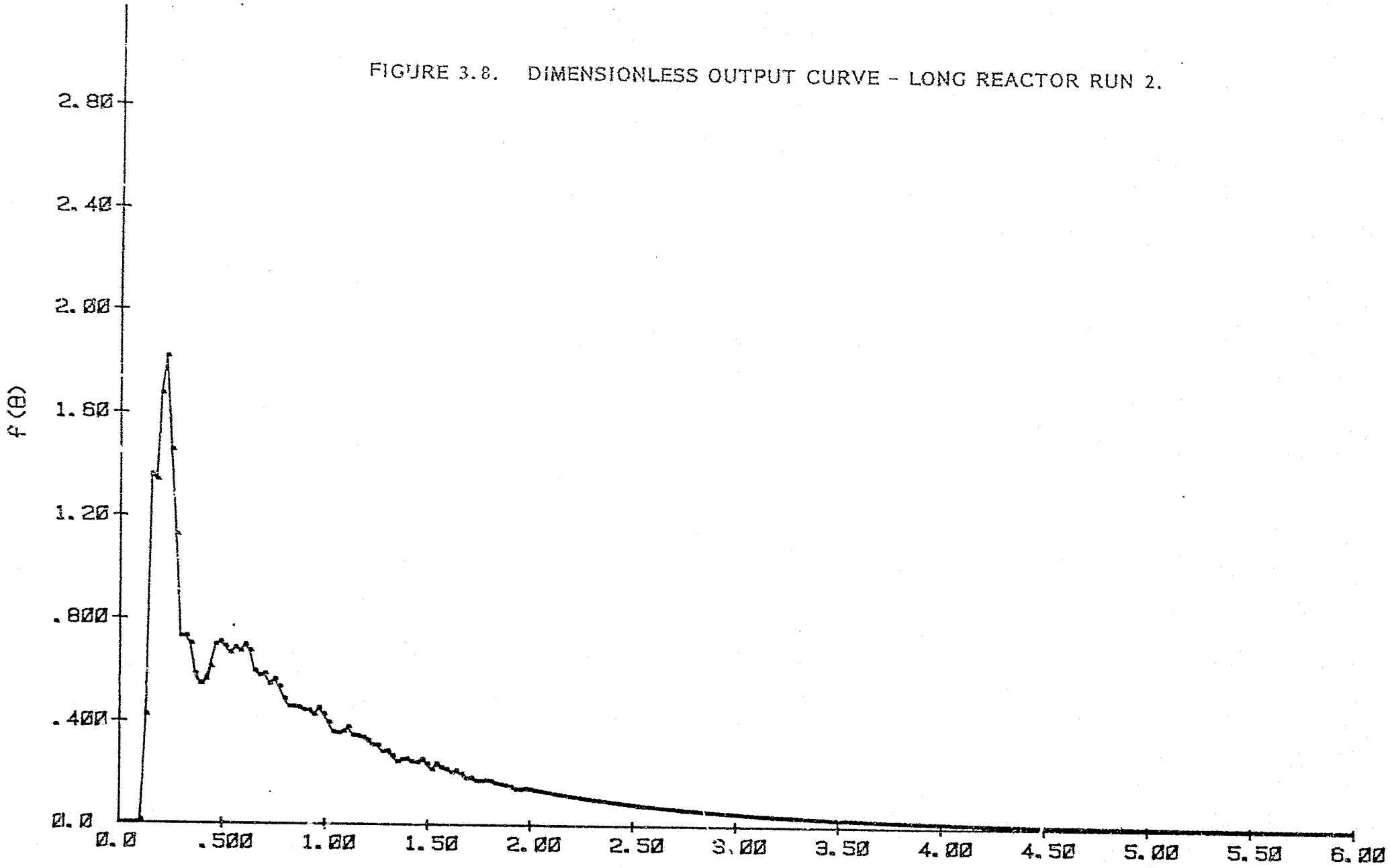


FIGURE 3.9. DIMENSIONLESS OUTPUT CURVE - LONG REACTOR RUN 3.

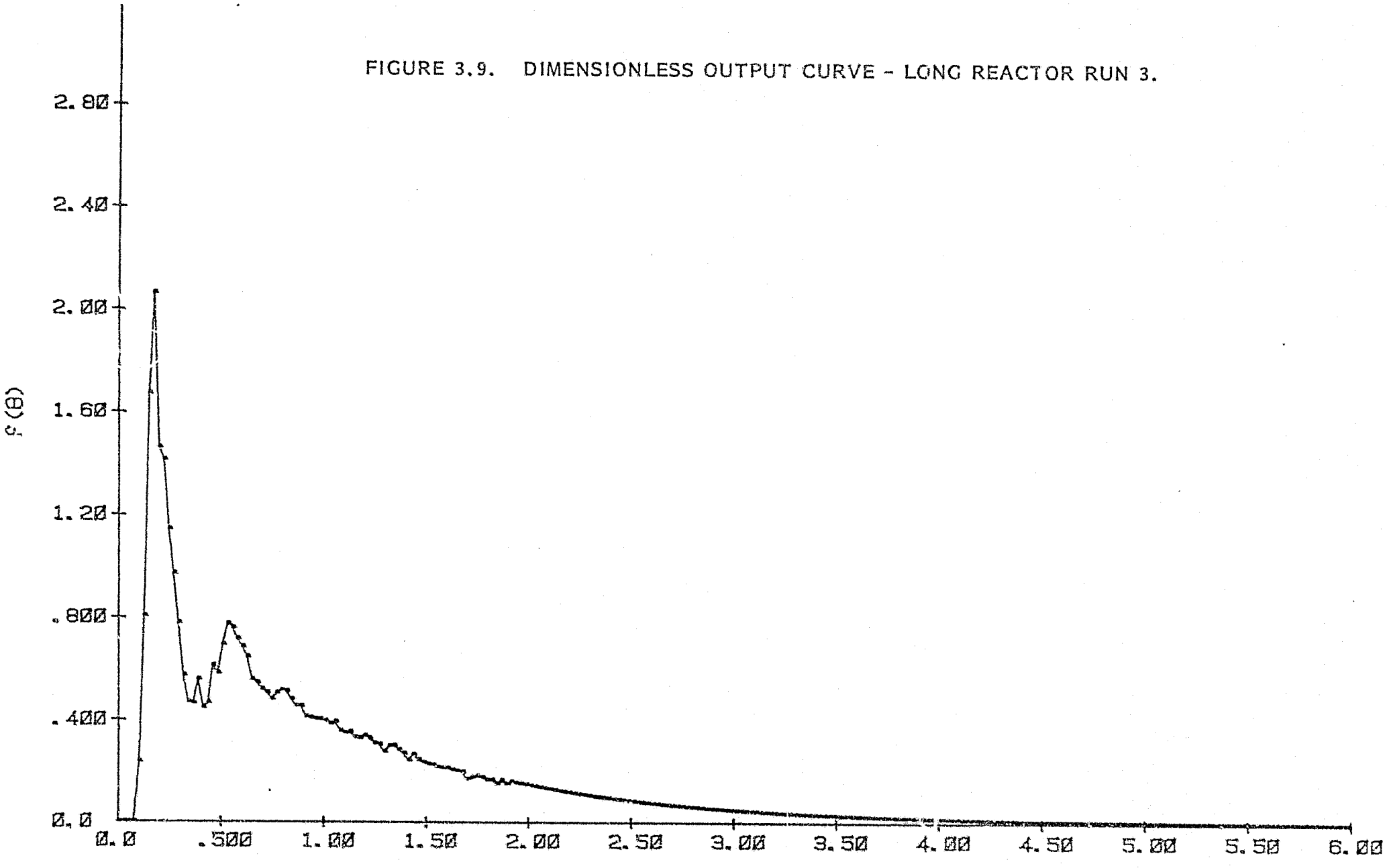


FIGURE 3.10. DIMENSIONLESS OUTPUT CURVE - LONG REACTOR RUN 4.

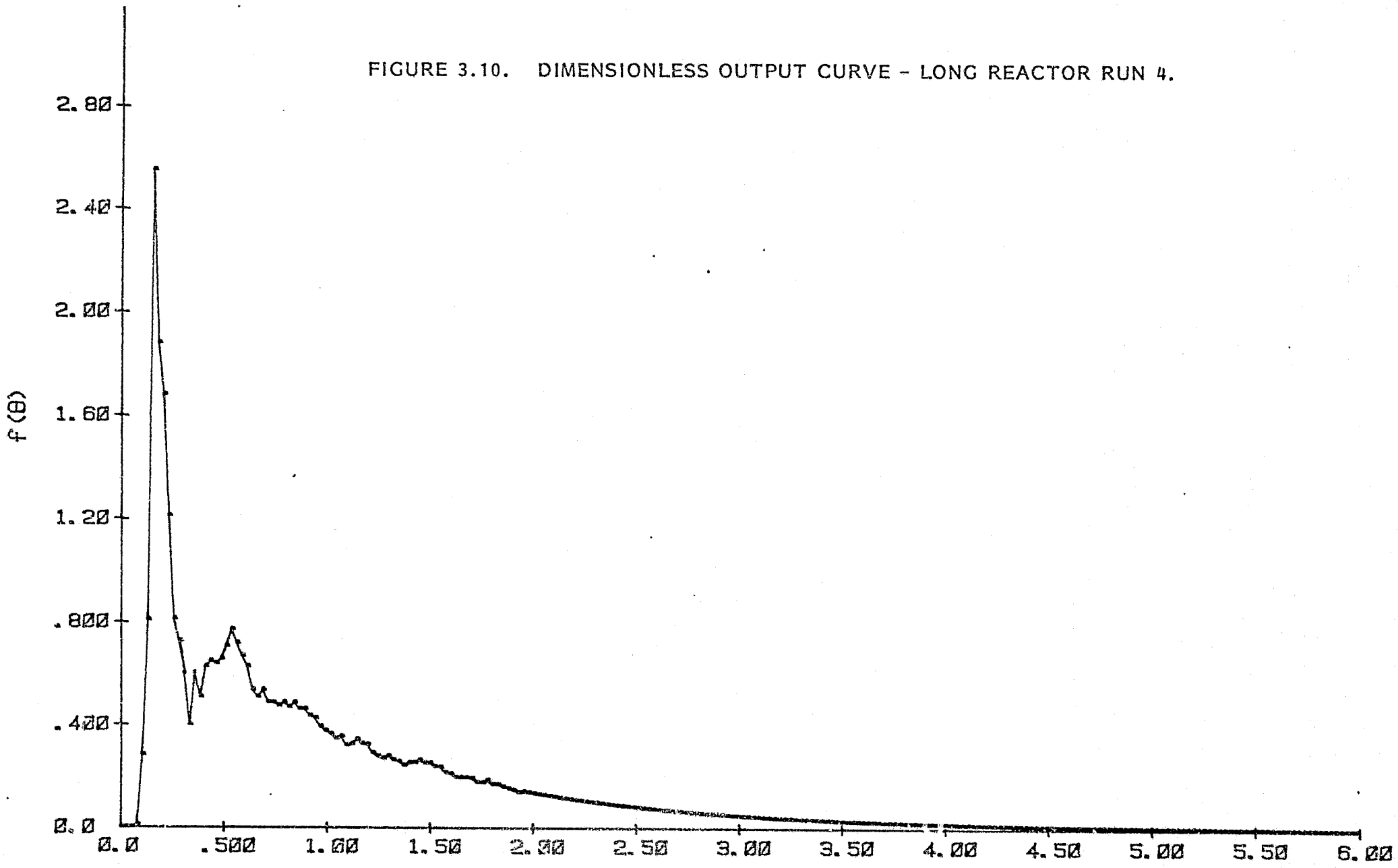


FIGURE 3.11. DIMENSIONLESS OUTPUT CURVE - LONG REACTOR RUN 5.

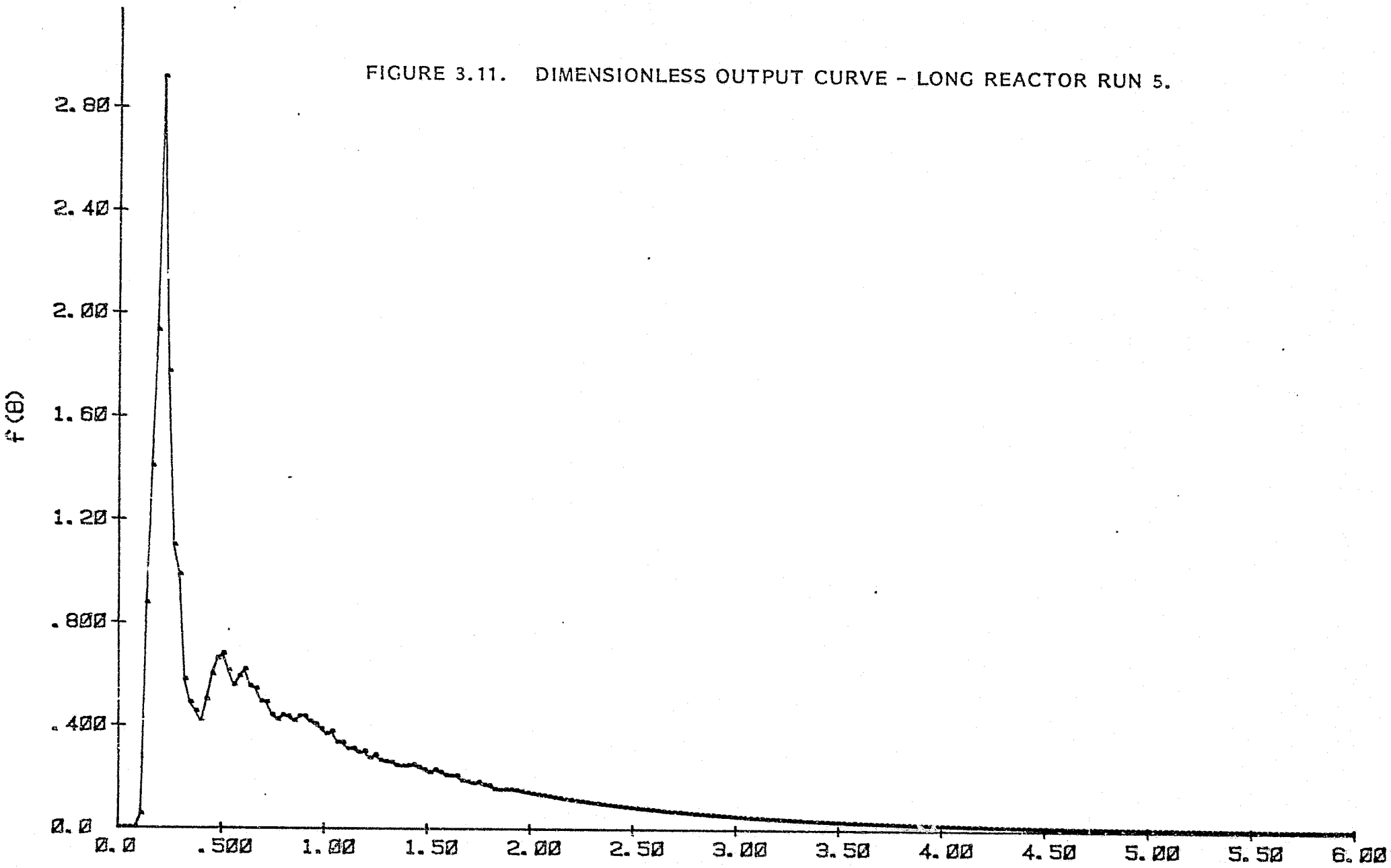


FIGURE 3.11. DIMENSIONLESS OUTPUT CURVE - LONG REACTOR RUN 5.

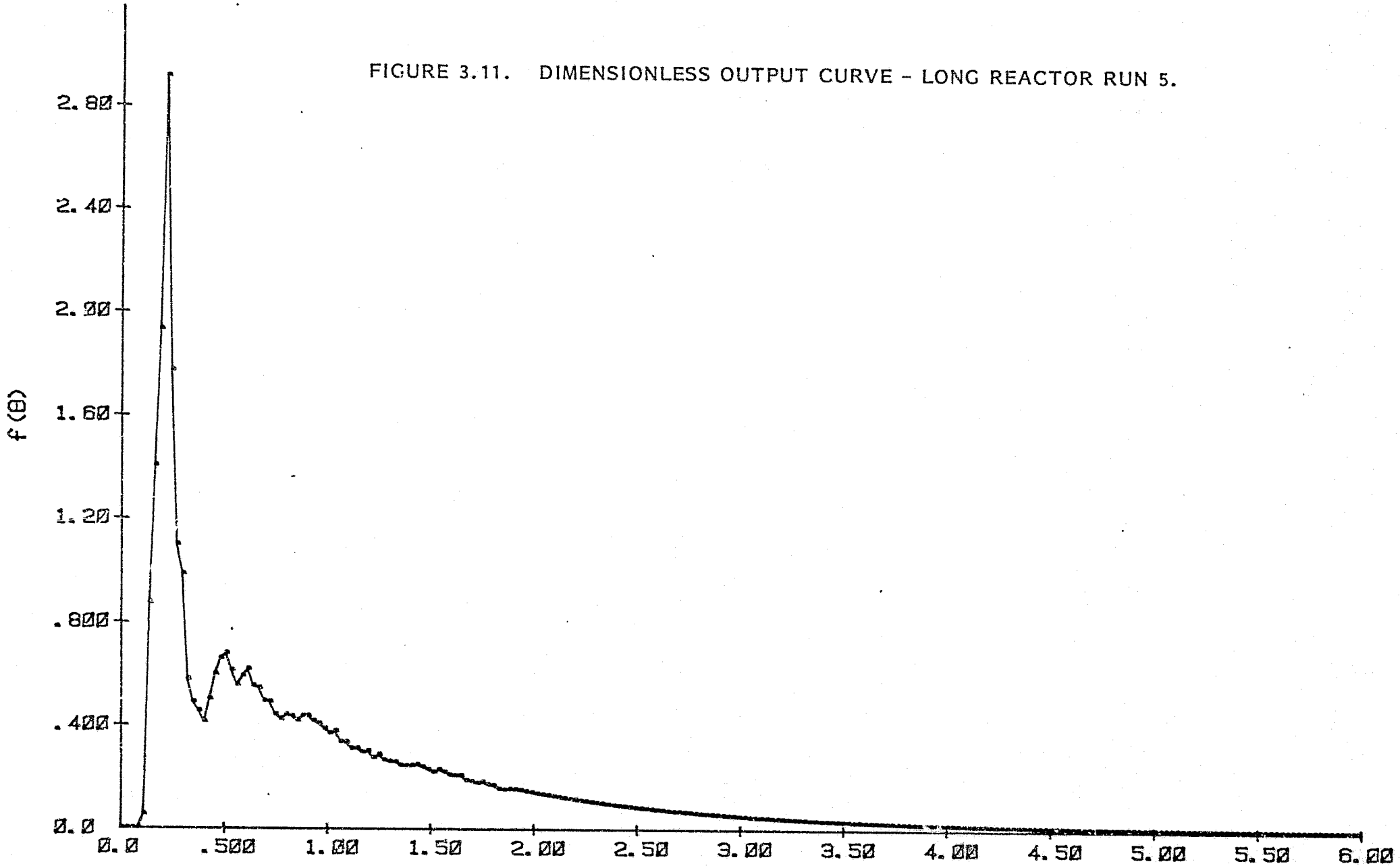


FIGURE 3.12. DIMENSIONLESS OUTPUT CURVE - SHORT REACTOR RUN 1.

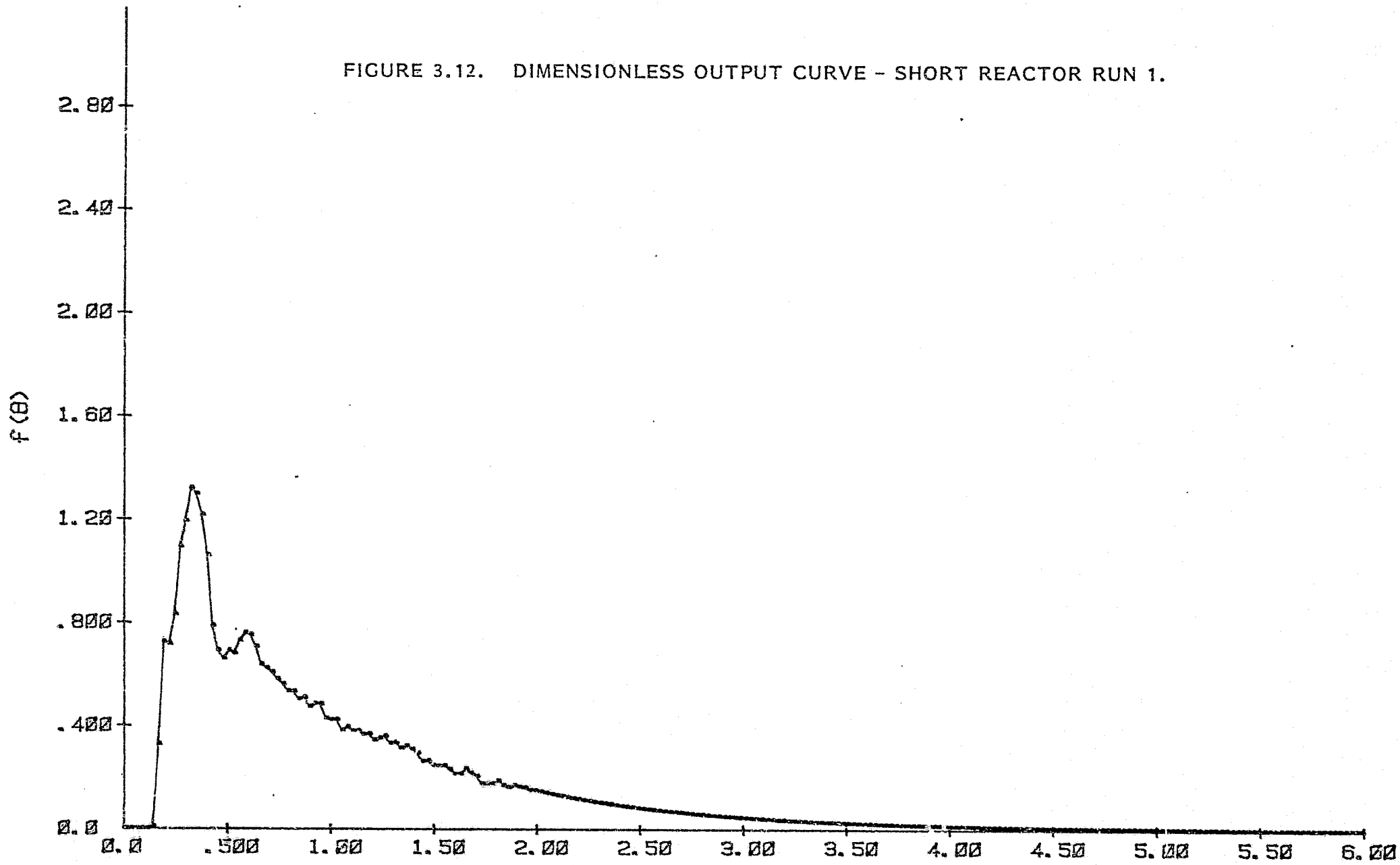


FIGURE 3.13. DIMENSIONLESS OUTPUT CURVE - SHORT REACTOR RUN 2.

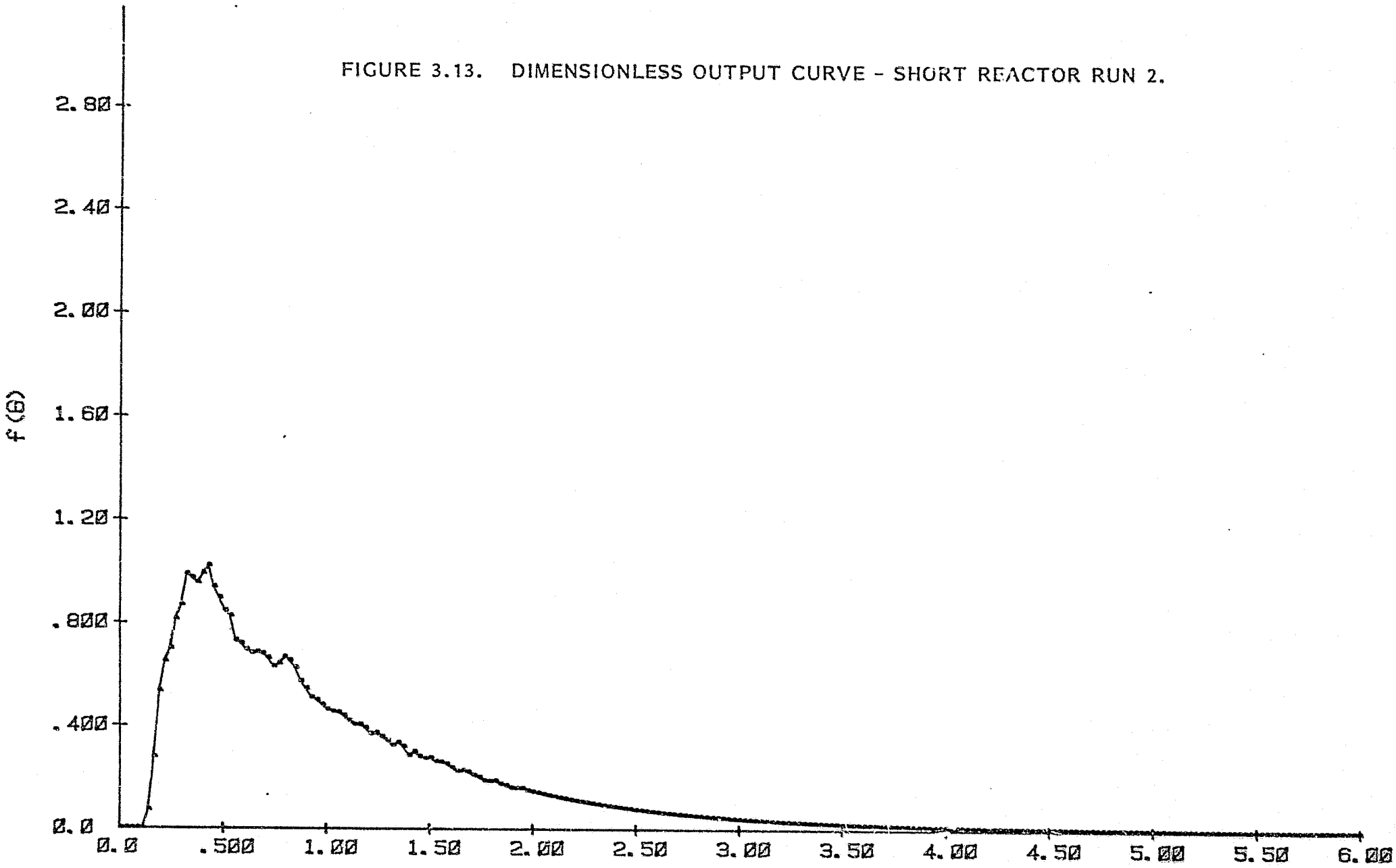


FIGURE 3.14. DIMENSIONLESS OUTPUT CURVE - SHORT REACTOR RUN 3.

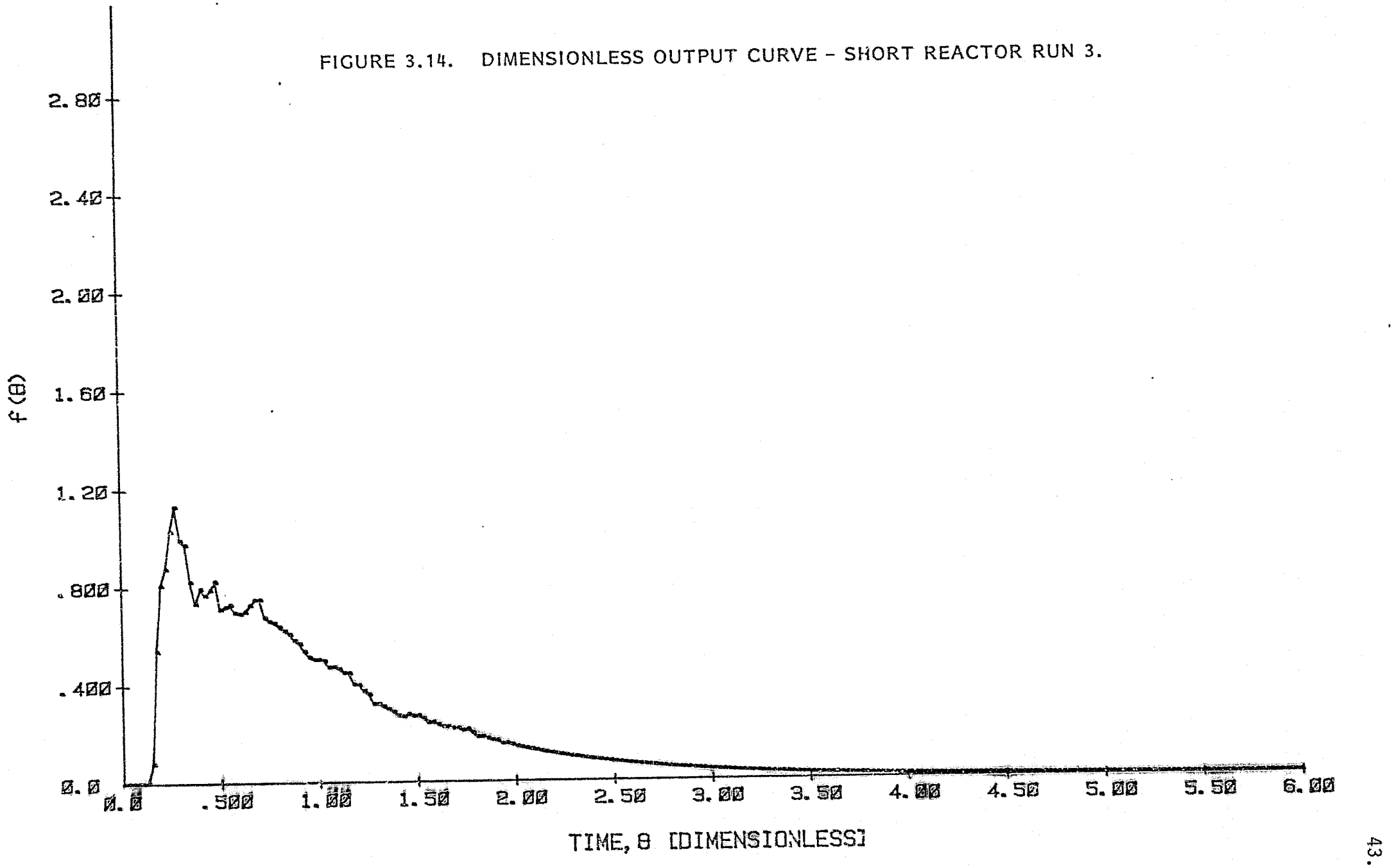


FIGURE 3.15. DIMENSIONLESS OUTPUT CURVE - SHORT REACTOR RUN 4.

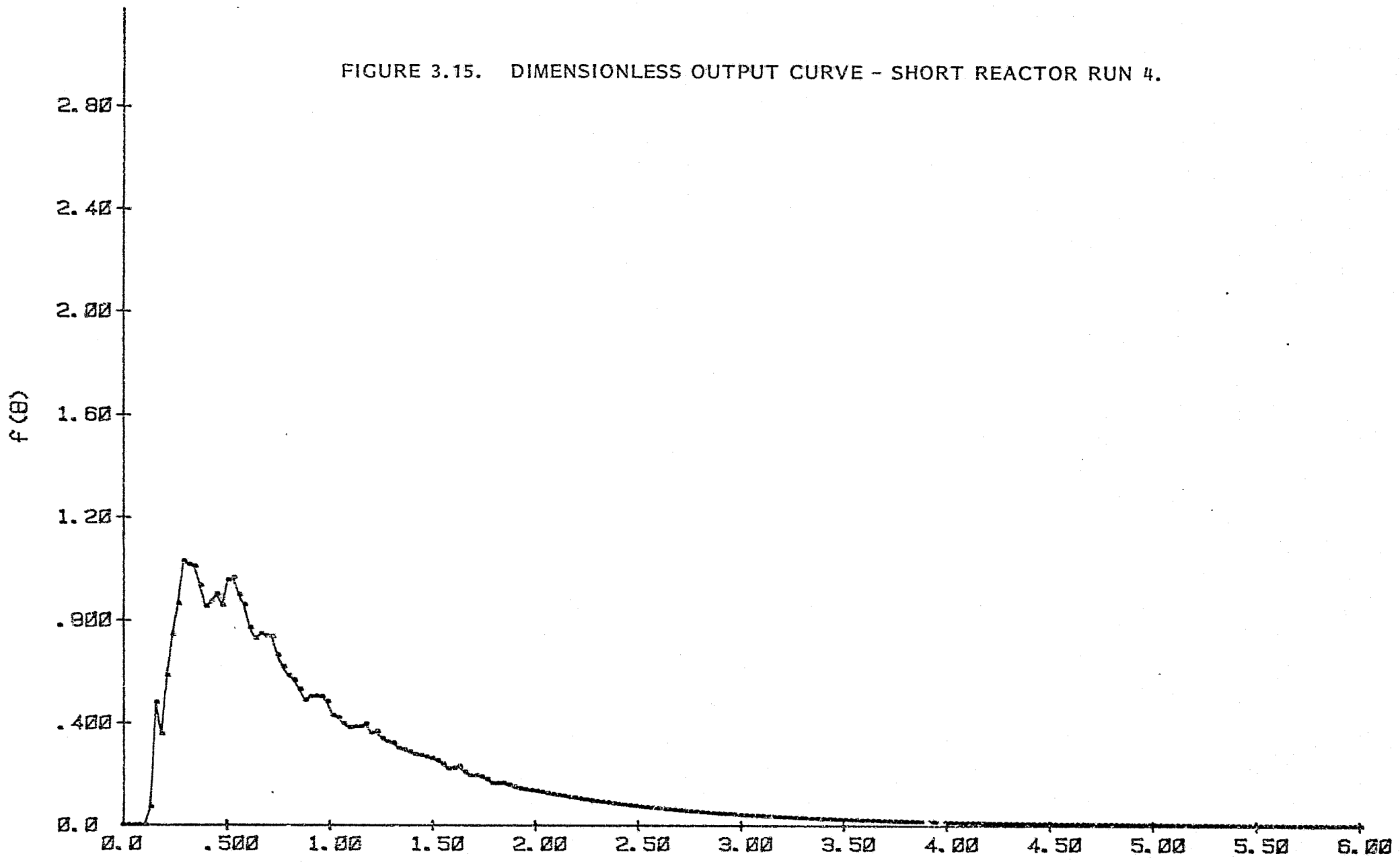


FIGURE 3.16. DIMENSIONLESS OUTPUT CURVE - SHORT REACTOR RUN 5.

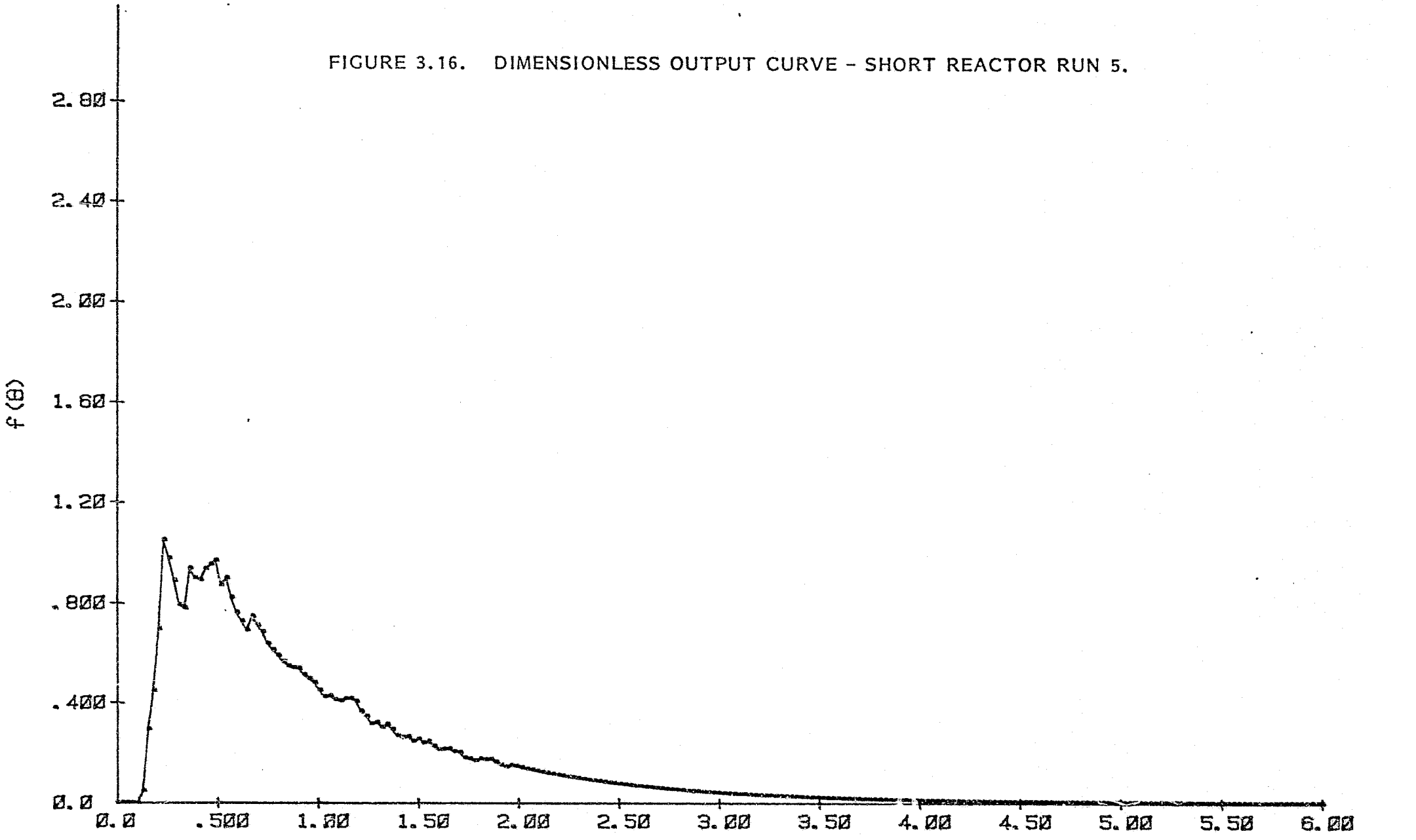


FIGURE 3.17. DIMENSIONLESS OUTPUT CURVES - LONG REACTOR

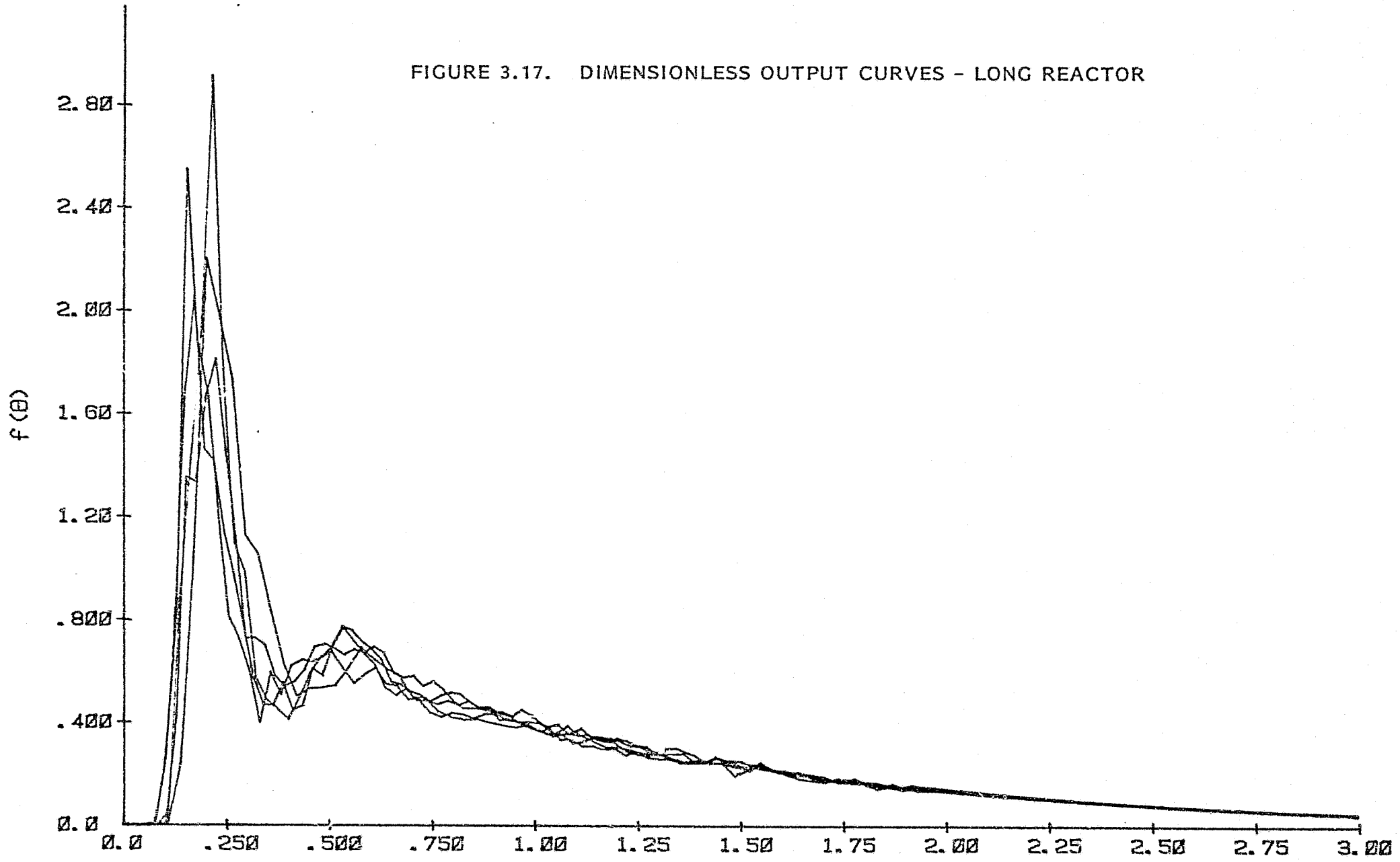
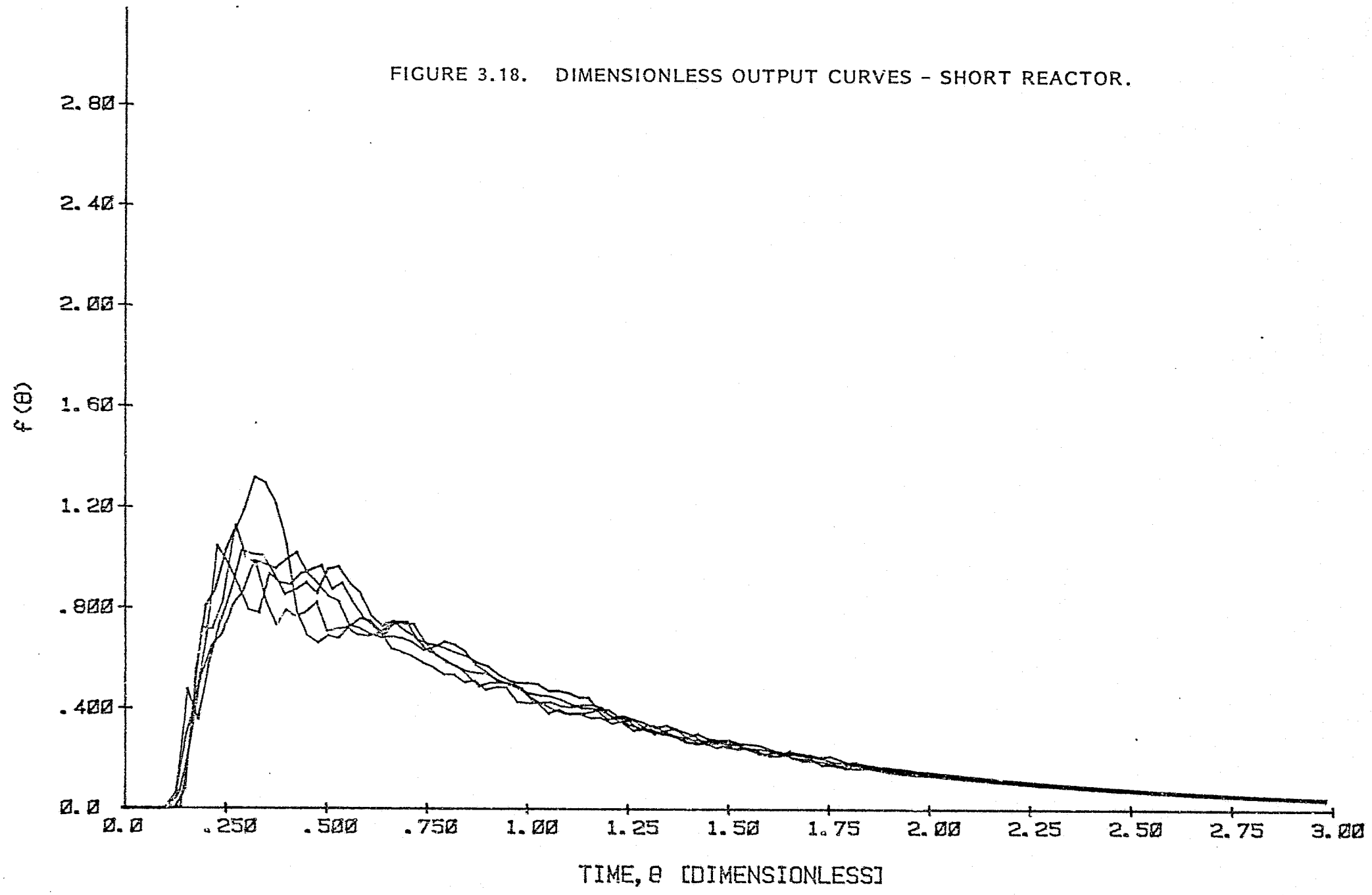


FIGURE 3.18. DIMENSIONLESS OUTPUT CURVES - SHORT REACTOR.



3.4 FLOW VISUALIZATION

Various types of powders and beads were introduced into the feed to the vessel, and the interior of the vessel was lit by stroboscope lighting in a dark room. The effect is that each particle shows up as a line of dots, thus indicating the direction and velocity of the particle.

A suitable particle for flow visualization tests should be small and light enough so as to follow the air flow patterns closely (19), but large enough to be seen by the eye or camera. Lycopodium powder (30 micron) is recommended by Merzkirch (19) and is light and free-flowing, but the particles were found to be too small to be seen individually in the vessel by either eye or camera. Using polystyrene spheres (0,5 to 1 mm) with a stroboscope speed of 25 000 rpm and a total flowrate of 970 m^3/h, the flow patterns could clearly be seen with the naked eye. With particles of this size, however, it must be remembered that the particle trajectories do not conform closely with the gas flow path.

In the case of the long reactor, high velocity jets of air could be seen, extending from the inlets to the centre of the vessel. Surrounding these central regions was a reverse flow of air recycling back towards the entrances. This observation confirms the view that the series of peaks in the output curve of this reactor is due to recirculation in the vessel.

In the case of the short reactor only the central jets could be distinguished and the rest of the vessel volume was well mixed. In both cases it could be seen now the flow patterns continuously fluctuated, particularly in the region where the inlet jets impinged.

Photography of the flow patterns was attempted, and the best results were obtained with a shutter speed of 1/60 second and an aperture of f/2,8. However, difficulty was experienced in focus-

ing on a particular plane in the vessel, and the closer particles (particularly on the bottom) obscured the picture. A better three-dimensional effect was obtained with the naked eye.

4. FREQUENCY ANALYSIS

4.1 INTRODUCTION

The technique of frequency analysis (13) uses the coefficients of the Fourier Series to characterise and analyse the RTD curves. For this analysis, only a recording of an input perturbation and the resultant output signal are required. The same information as for a whole series of tests with a sinusoidally varying tracer input is obtained. The input and output signals are both expressed as Fourier Series over a selected finite time interval. The Fourier coefficients of the true RTD curve are found by correcting for the imperfect input signal.

Frequency analysis has many advantages over time-domain analyses. Complicated convolution procedures used to predict the system response to any input disturbance become simple algebraic manipulations in the frequency domain. Similarly, correction for a non-ideal input pulse is also an algebraic correction the Fourier coefficients. Another useful property of the Fourier series is that experimental "noise" can effectively be smoothed out by truncation of the series at a suitable frequency. Frequency analysis also has a particular advantage when applied to systems exhibiting recycle, as the natural frequency shows up on the amplitude ratio plot.

A technique which is commonly used to analyse residence time distributions is the method of moments (20). This method is not used here, as it suffers from two serious disadvantages. The first of these is an uneven weighting of the "tail" of the RTD curve compared to the initial response. Noisy data in the tail region (due to lower radiation count rates when using radioactive tracers) leads to large errors. The second disadvantage of the method of moments is that only the first two moments are generally sufficiently reproducible to be used, while more than two moments are needed to uniquely describe a vessel with complicated flow patterns.

The Fourier coefficients can also be used to fit simple block-diagram type mathematical flow models to the RTD curves (see section 6). The theoretical model Fourier coefficients are derived from the Laplace Transform of the Model RTD function, and are relatively simple expressions compared to the complicated real time solutions (see appendices VII, VIIIand IX). A least-squares model fitting procedure is therefore much simpler in the frequency domain than in the time domain.

4.2 THEORY

The RTD function f(t) may be represented by a Fourier Series :

$$f(t) = \sum_{n=1}^{\infty} a_n \sin \frac{n\pi t}{T} + \sum_{n=0}^{\infty} b_n \cos \frac{n\pi t}{T} \qquad (4.1)$$

where $$a_n = \frac{1}{T} \int_0^{2T} f(t) \sin \frac{n\pi t}{T} \, dt \qquad (4.2)$$

$$b_o = \frac{1}{2T} \int_0^{2T} f(t) \, dt \qquad (4.3)$$

$$b_n = \frac{1}{T} \int_0^{2T} f(t) \cos \frac{n\pi t}{T} \, dt \qquad (4.4)$$

The above series expansion is subject to the Dirichlet conditions (7), which however do not impose any serious limitation on the type of function f(t).

The Fourier coefficients (a_n, b_n) of the experimental input and output curves are evaluated from the above equations by numerical integration (computer program "F-ANAL", appendix XI.4). Although the Fourier series is a periodic function, we are interested only in the fundamental interval [0,2T] comprising one cycle. T is

chosen so that the input pulse has practically returned to zero at time 2T. A value for 2T of six times the mean residence time was found to be adequate, by which time f(t) has diminished to about 0,001 of its maximum value, and the area under the normalised curve up to this point equals approximately 0,999.

Writing the Laplace transform of f(t), we obtain the transfer function for the system:

$$F(s) = \mathcal{L}\{f(t)\} = \int_0^\infty \exp(-st)\ f(t)\ dt \qquad (4.5)$$

where the complex variable $s = \alpha + iw$.

Since $\int_0^\infty |f(t)|dt$ is bounded (equals unity), choosing $\alpha = 0$ ensures the convergence of the Laplace integral F(iw). Furthermore we may approximate this infinite integral over the range 0 to 2T, if f(t) is sufficiently small for $t > 2T$.

Then

$$F(iw) = \int_0^{2T} \exp(-iwt)\ f(t)\ dt$$
$$= \int_0^{2T} f(t)\ \cos(wt)\ dt - i \int_0^{2T} f(t)\ \sin(wt)\ dt$$

Now from equations (4.2) to (4.4) with frequency w given by

$$w = \frac{n\pi}{T}$$

we have

$$F(iw) = Tb_n - iTa_n \qquad (n \geq 1) \qquad (4.6)$$

$$F(0) = 2Tb_o \qquad (4.7)$$

The above two equations relate the Fourier coefficients to the Laplace transform of the RTD function. The frequency response of

the system can also be expressed in terms of the amplitude ratio (AR) and phase lag (Ø), by writing F(iw) in polar form :

$$F(iw) = AR \exp(i\emptyset) \tag{4.8}$$

From equation (4.6),

$$AR = T\sqrt{a_n^2 + b_n^2} \tag{4.9}$$

$$\emptyset = -\tan^{-1}(a_n/b_n) \tag{4.10}$$

The number of pairs of Fourier coeffients (N) which can be used, is limited by the number of experimental readings taken. If the number of readings is M, then a series with N = M/2 pairs of coefficients will fit the set of data points exactly. If more than M/2 pairs of coefficients are used then a cyclical repetition of previous coefficients will occur - a phenomenon called aliasing. The corresponding hignest possible frequency, called the folding frequency is given by $w = M\pi/2T$.

By choosing N<M/2, some high frequency content of the signal will be lost. As the high frequency content is mainly noise, this truncation of the Fourier Series results in a smoothing of the curve. The amplitude ratio plot (AR vs w) is used to determine the truncation frequency, i.e. the frequency above which the amplitude of the signal drops below that of the noise (see e.g. figure IV.5).

If the input pulse is recorded at the vessel inlet, then the Fourier coefficients of this curve can be used to correct those of the output curve, so as to obtain the coefficents of the true RTD curve. For a linear system,

$$F_{out}(s) = F(s).F_{in}(s)$$

where subscripts "in" and "out" refer to the input and output, and F(s) is the transfer function. Writing equation (4.6) for each of

the three F(s) functions, we obtain

$$(Tb_{n_{out}} - iTa_{n_{in}}) = (Tb_n - iTa_n).(Tb_{n_{in}} - iTa_{n_{in}})$$

Equating real and imaginary parts,

$$b_{n_{out}} = T(b_{n_{in}} b_n - a_{n_{in}} a_n)$$

$$a_{n_{out}} = T(a_{n_{in}} b_n - a_n b_{n_{in}})$$

The Fourier coefficients of the true RTD function are given by

$$a_n = \frac{b_{n_{in}} a_{n_{out}} - a_{n_{in}} b_{n_{out}}}{T\,(b^2_{n_{in}} + a^2_{n_{in}})} \qquad (4.11)$$

$$b_n = \frac{b_{n_{in}} b_{n_{out}} + a_{n_{in}} a_{n_{out}}}{T\,(b^2_{n_{in}} + a^2_{n_{in}})} \qquad (4.12)$$

4.3 RESULTS OF FREQUENCY ANALYSIS

The Fourier coefficients and the corresponding amplitude ratios and phase lags are computed for each dimensionless output curve (using program F-ANAL, appendix XI.4). A total of M/2 pairs of coefficients are computed for each output curve, where M is the number of experimental points up to $\theta = 6$. Plots of the Fourier coefficients, amplitude ratio and phase lag for each run are given in appendices IV and V.

The Fourier coefficients are seen to follow a characteristic pattern for each reactor up to a certain frequency, above which noise predominates and the coefficients oscillate randomly about zero. As discussed in section 4.2, the Fourier Series is truncated where the noise becomes predominant. The truncation frequency is determined from the amplitude ratio plot, where log AR is seen to take a sharp dip and thereafter oscillate randomly.

The suitable truncation point shows up more clearly in some AR plots (e.g. figure IV.5) than others. Truncation and folding frequencies are listed in table 4.1. Frequencies are given in terms of n (the Fourier coeffient pair number); the frequency in rad/sec is given by $w = n\pi/T$, where a value for T of 3 is used for all curves.

TABLE 4.1. TRUNCATION AND FOLDING FREQUENCIES

	LONG REACTOR		SHORT REACTOR	
RUN	TRUNCATION FREQ (n=N)	FOLDING FREQ (n=M/2)	TRUNCATION FREQ (n=N)	FOLDING FREQ (n=M/2)
1	57	96	26	115
2	48	125	34	114
3	70	125	35	120
4	61	118	40	112
5	55	113	35	116

The amplitude ratio plots of the long reactor show a characteristic hump at about n = 15, called the natural frequency. This phenomenon is due to the series of peaks in the output curve and is characteristic of systems with recycle. The significance thereof is discussed further in appendix X.

Truncated Fourier series curves generated from the coefficients are seen to approximate the experimental points well, with effective smoothing out of some noise. Two examples of the fits are shown in figures 4.1 and 4.2. These curves (as well as all subsequent ones) are only plotted up to $\theta = 3$, as there is no important detail beyond this point. The oscillations of the Fourier

curves over the first few and last few (near $\theta = 6$) points is due to the Gibbs phenomenon in the vicinity of sharp changes, and is of no importance here.

Fourier coefficients of the input curves are also computed, after conversion of these curves to the same time units as the corresponding output curves. The Fourier coefficients of the RTD function are then computed using equations (4.11) and (4.12). Fourier curves generated from these corrected coeffients are compared to the uncorrected curves in figures 4.3 and 4.4. The runs with highest flowrate are illustrated, i.e. where the spread of the input curve was greatest (in θ units) and the correction most significant.

The corrected Fourier series curves representing the RTD functions are all plotted in figures 4.5 and 4.6 for the two vessel lengths respectively. The curves for different flowrates are now seen to correspond even more closely than in figures 3.15 and 3.16.

Typical dimensionless RTD curves of the two reactors are shown on the same axes in figure 4.7. The high first peak of the long reactor RTD is a weakness of this reactor, allowing about 30% of the feed to leave within one third of the mean residence time (see section 6.1). The more well-mixed RTD of the short model would result in higher conversions per unit reactor volume for simple reaction schemes.

FIGURE 4.1. FOURIER SERIES REPRESENTATION OF OUTPUT CURVE - LONG REACTOR RUN 3.

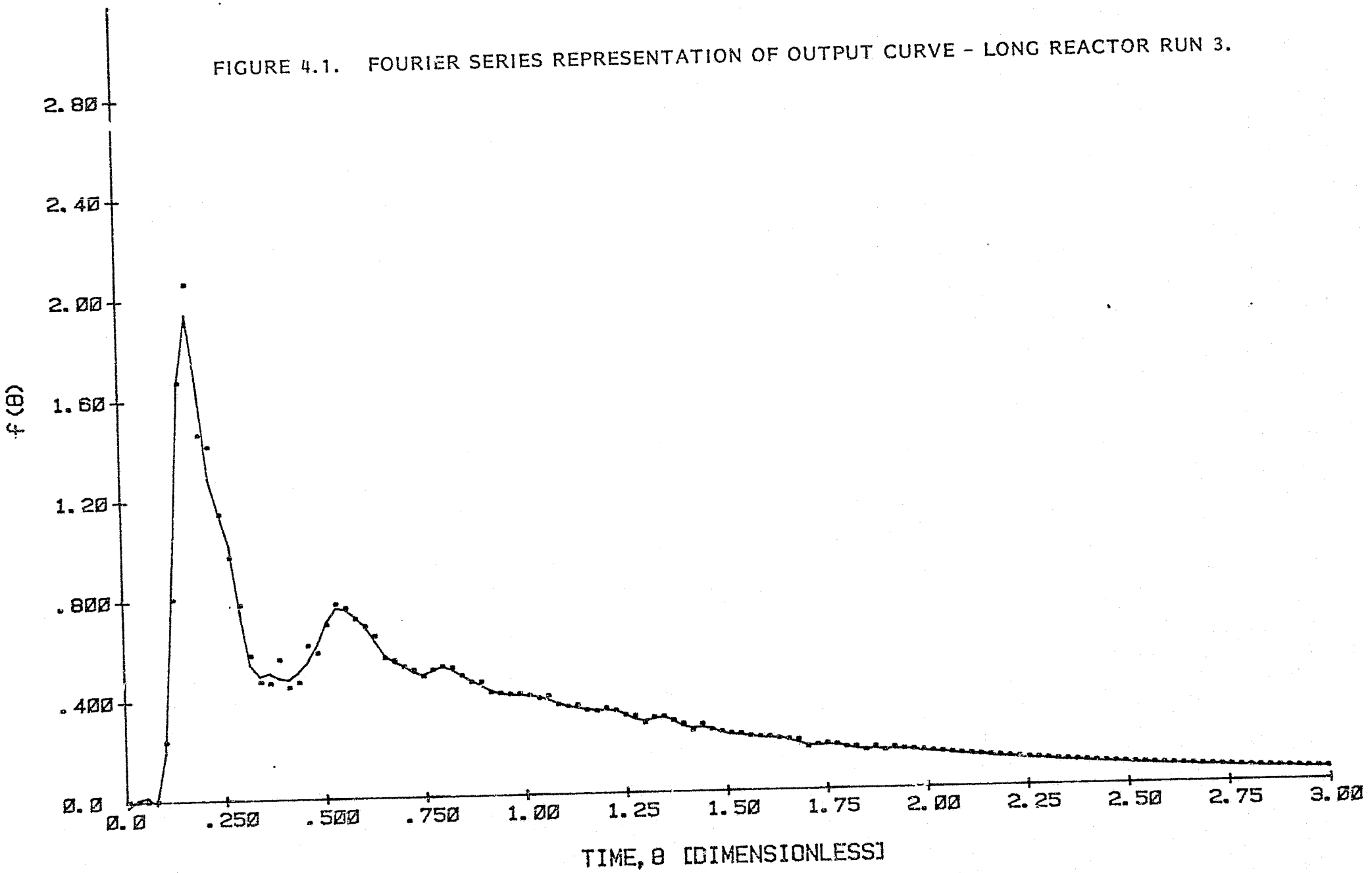


FIGURE 4.2. FOURIER SERIES REPRESENTATION OF OUTPUT CURVE - SHORT REACTOR RUN 5

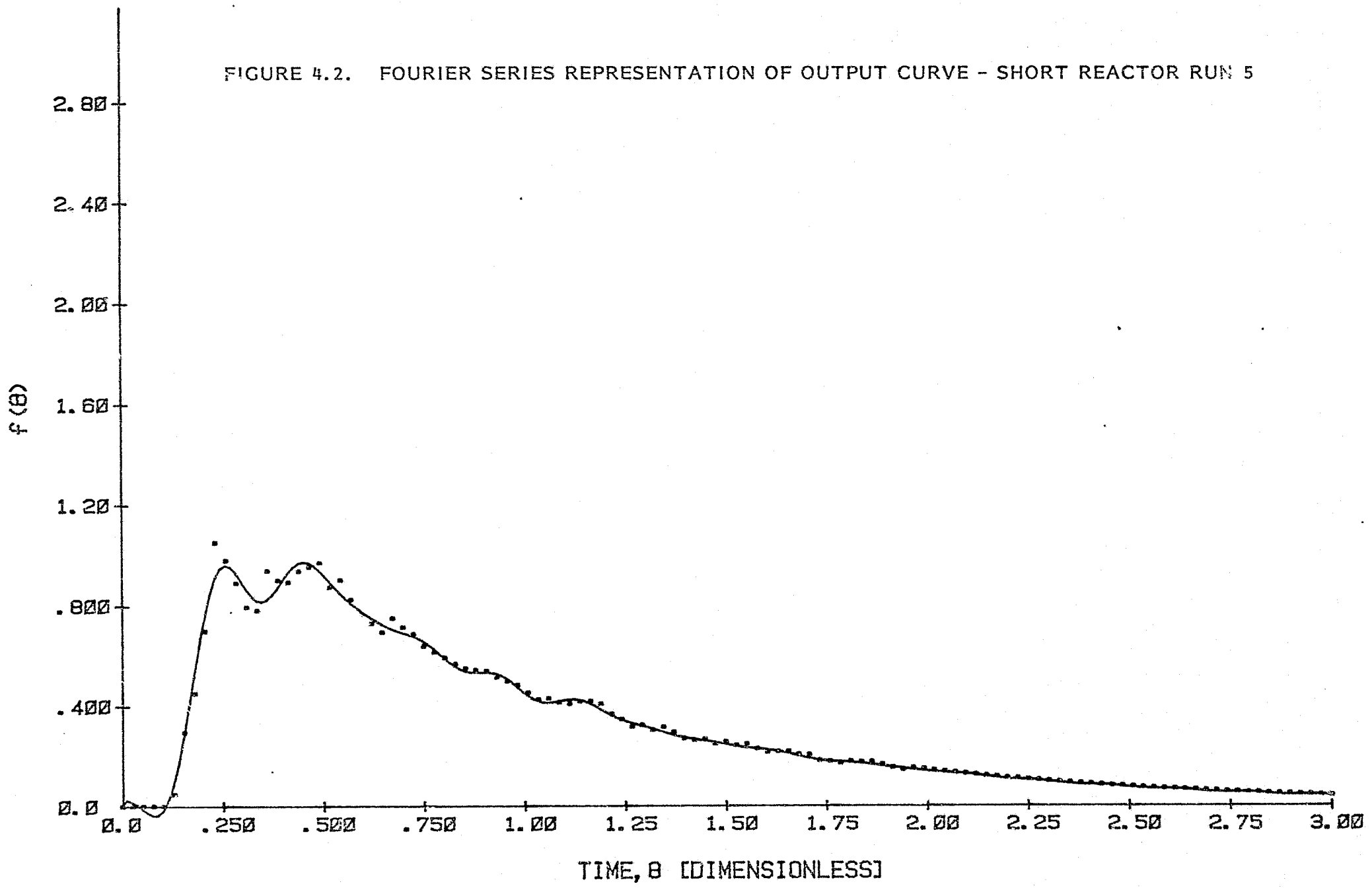


FIGURE 4.3. CORRECTION FOR NON-IDEAL INPUT - LONG REACTOR RUN 1.

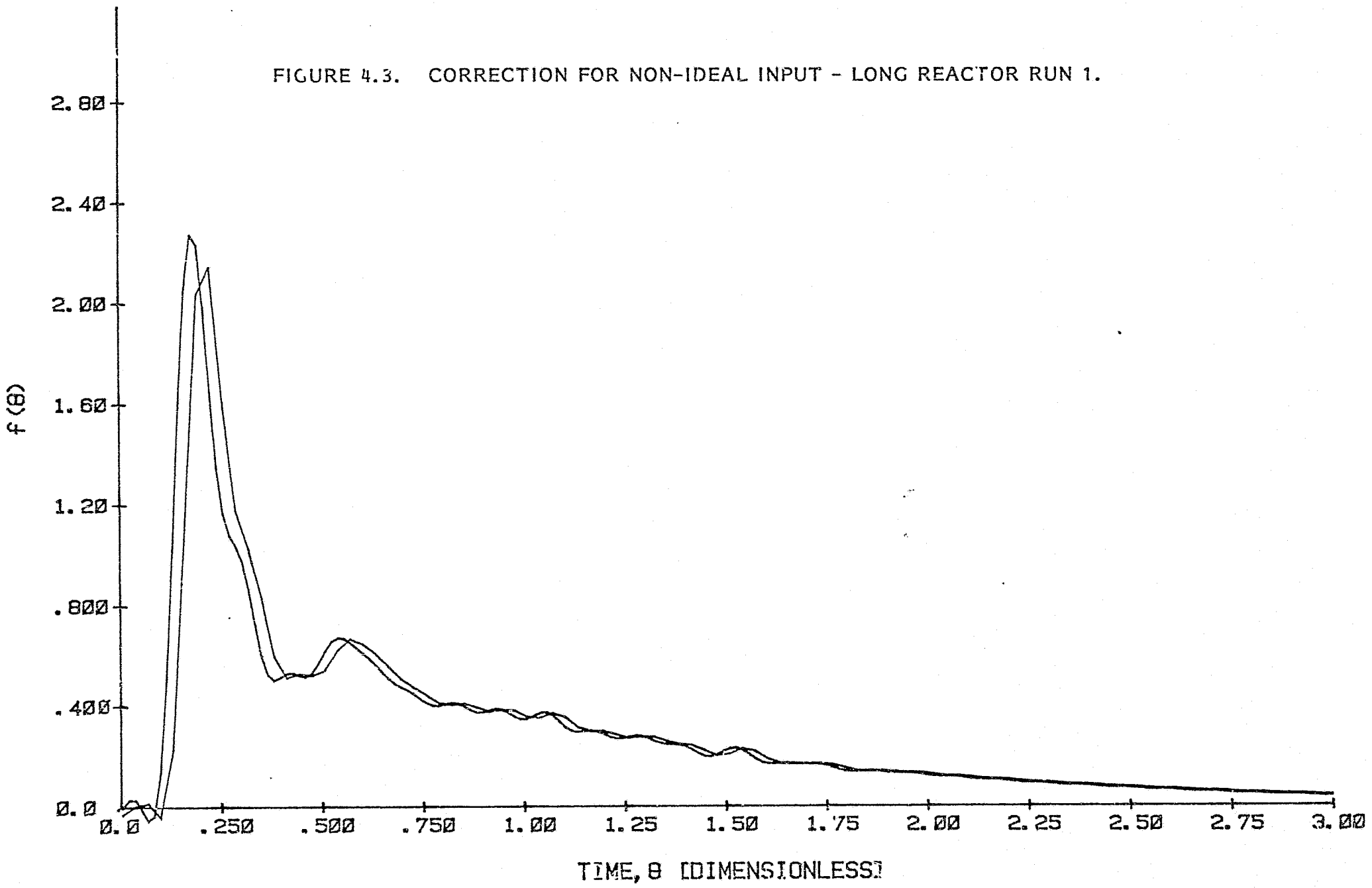


FIGURE 4.4 CORRECTION FOR NON-IDEAL INPUT - SHORT REACTOR RUN 1.

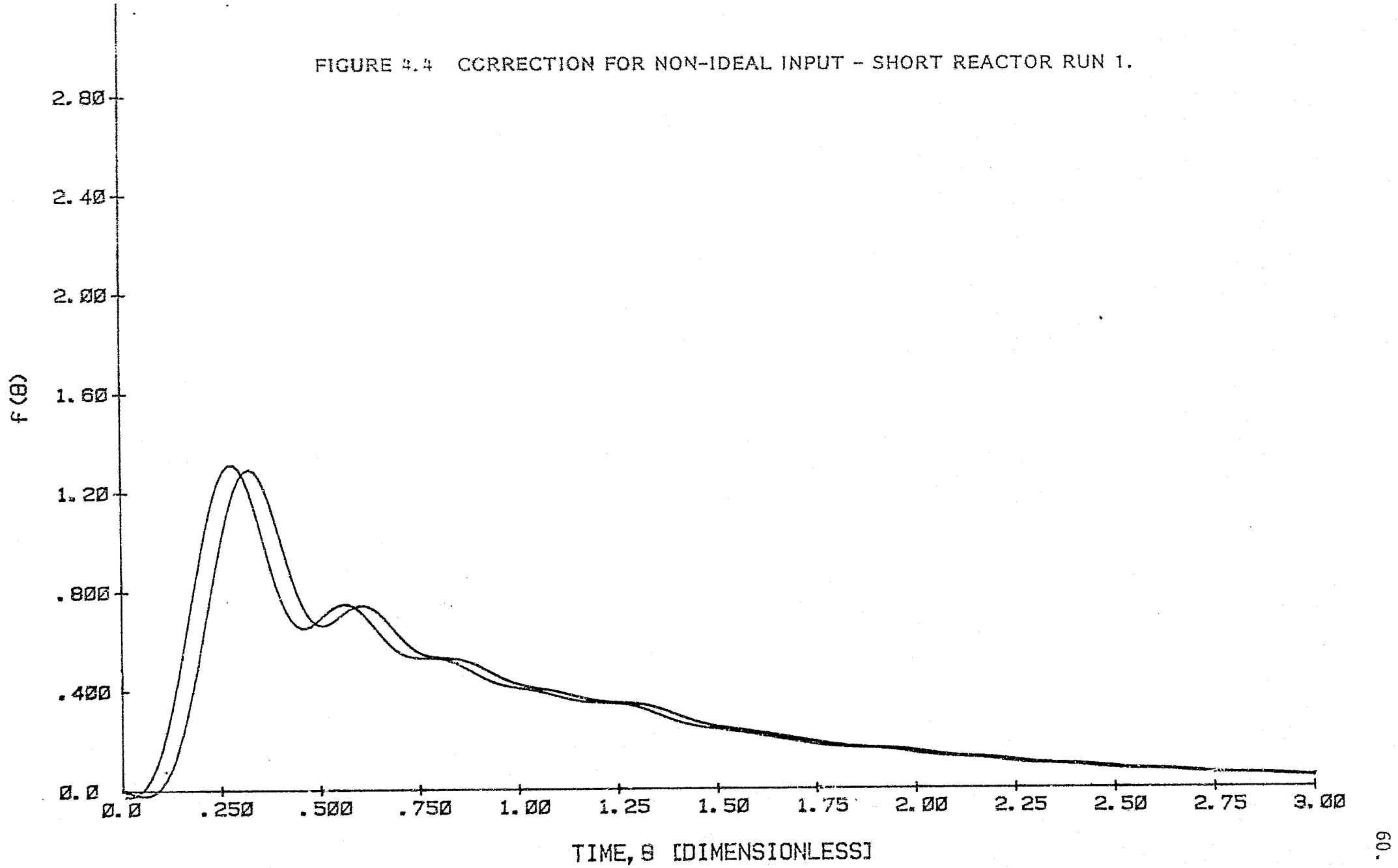


FIGURE 4.5. CORRECTED RTD CURVES - LONG REACTOR.

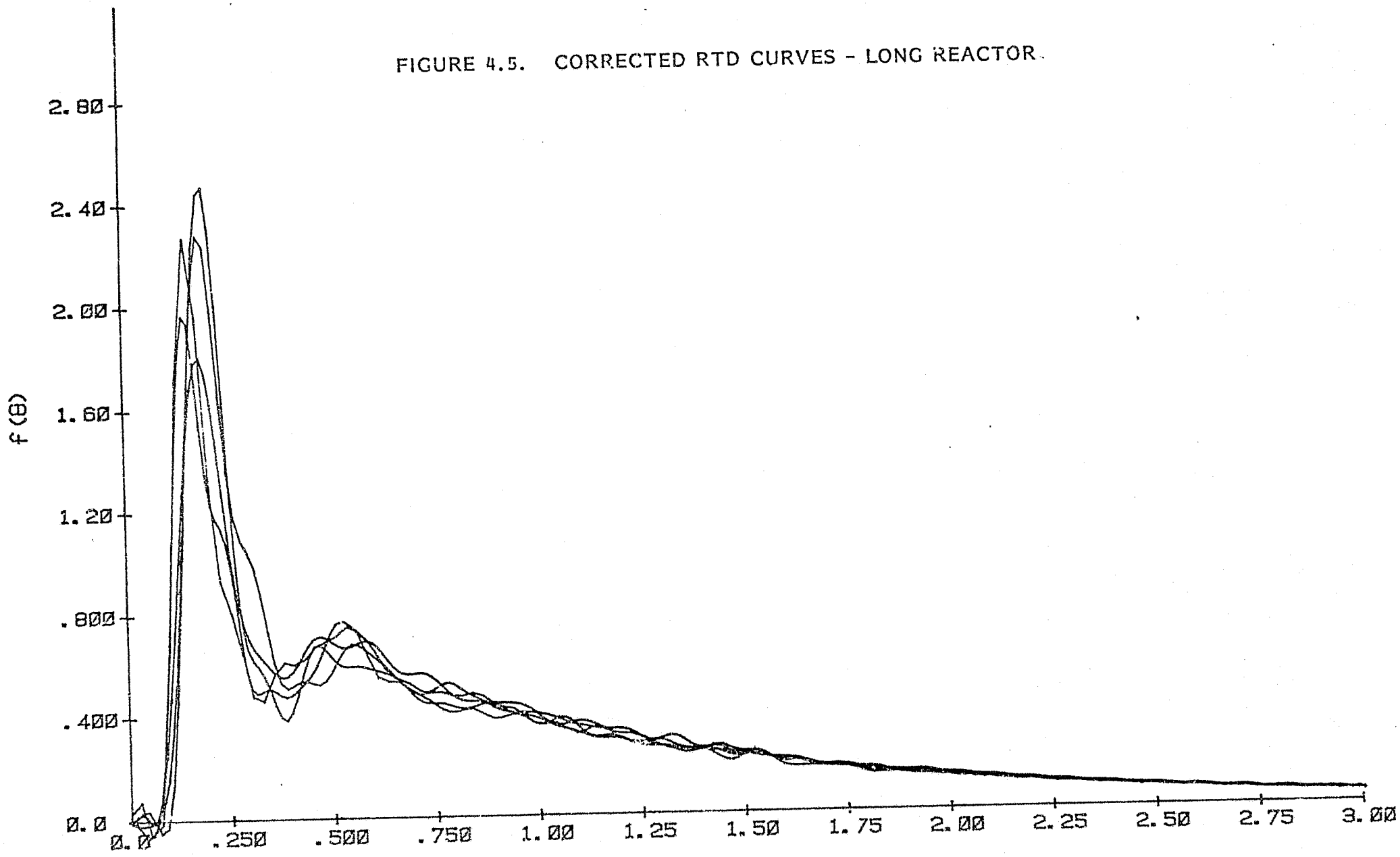


FIGURE 4.6. CORRECTED RTD CURVES - SHORT REACTOR.

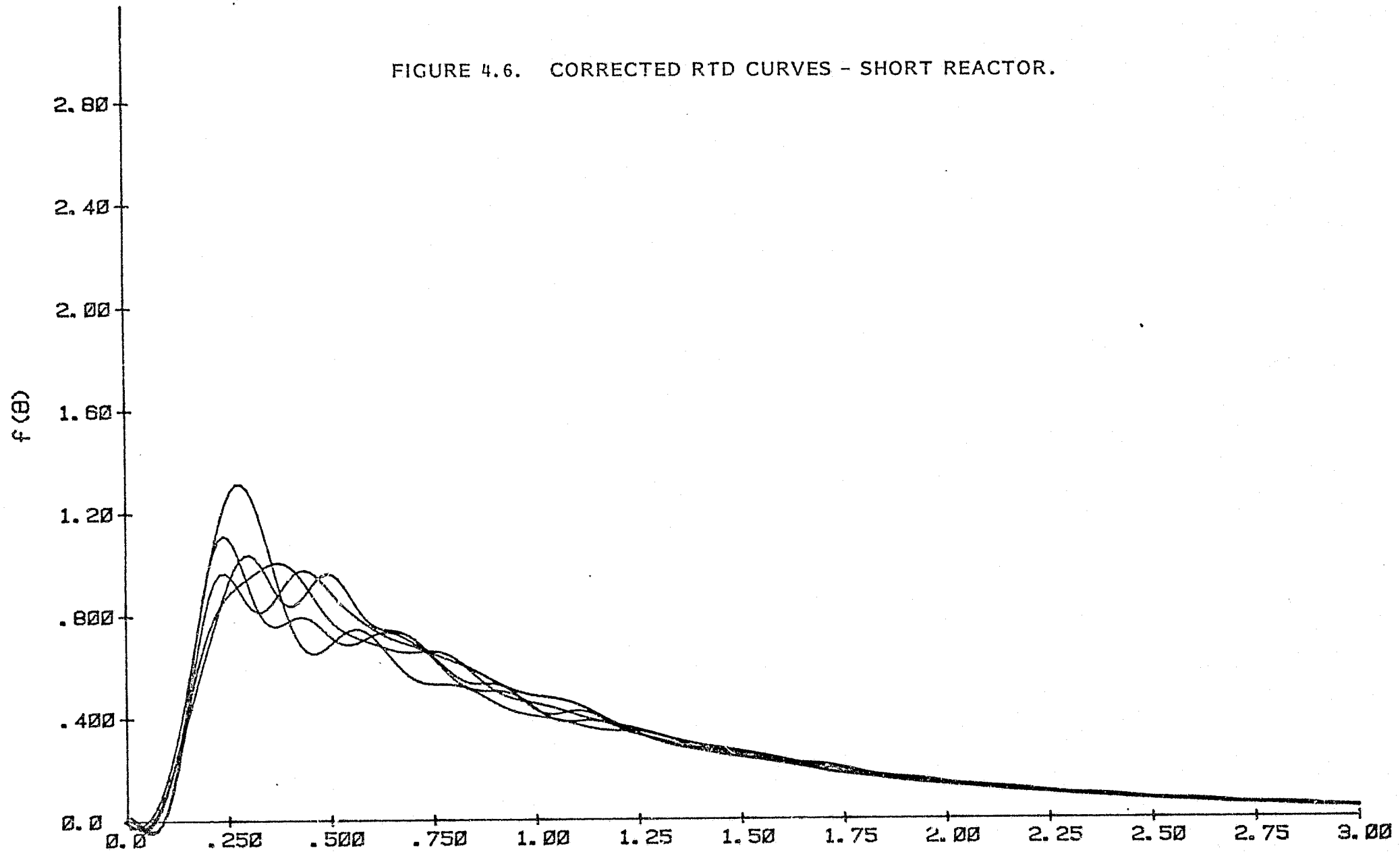
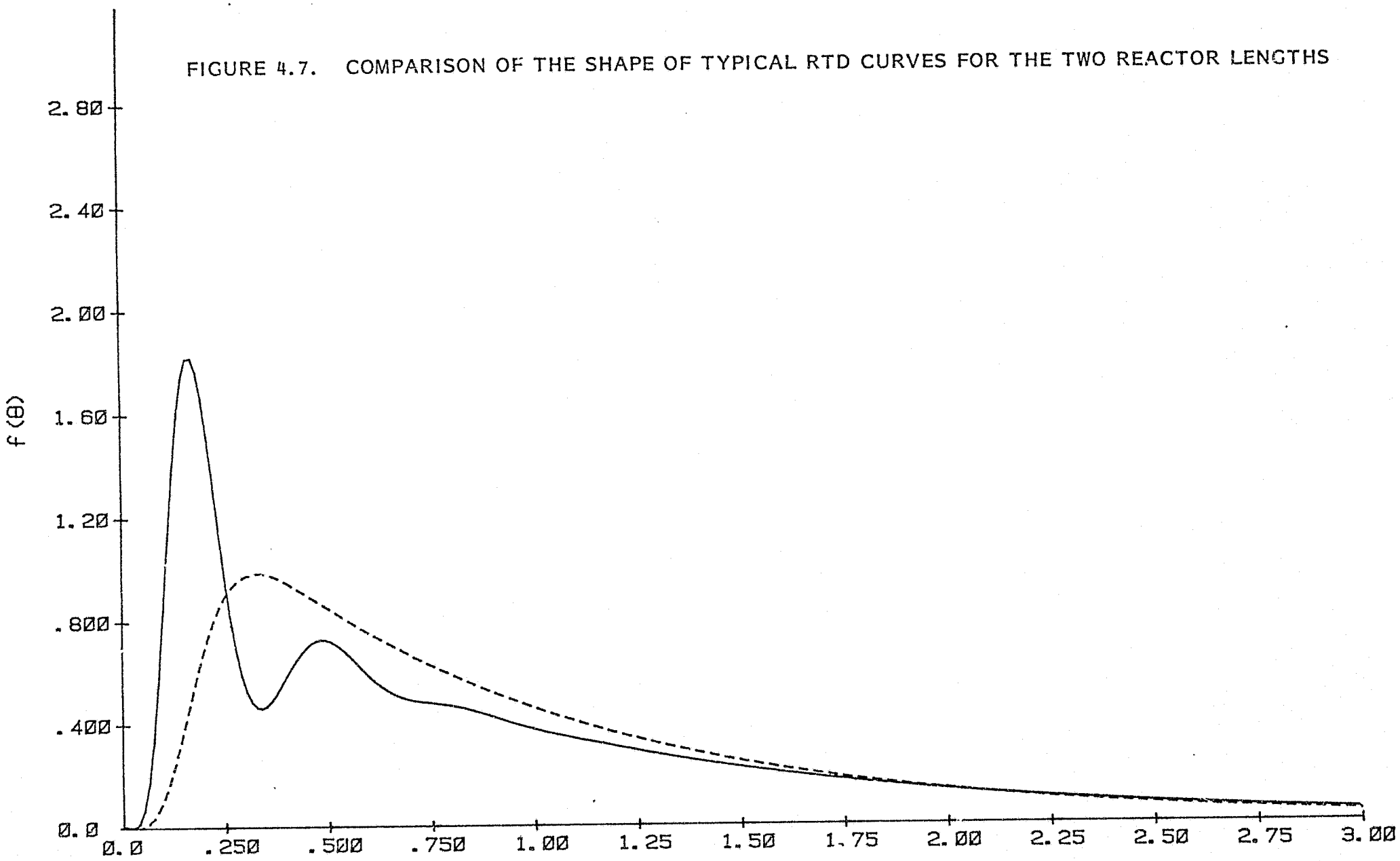


FIGURE 4.7. COMPARISON OF THE SHAPE OF TYPICAL RTD CURVES FOR THE TWO REACTOR LENGTHS



5. MATHEMATICAL MODELS

5.1 PROPOSED FLOW MODELS

In order to use the residence time distribution curve for prediction of conversion within the reactor, it is necessary to have further information regarding the flow patterns. This information is obtained from flow visualisation experiments (section 3.4) and the shape of the RTD curve. Based on this knowledge, and taking into account the physical configuration of the vessel, various flow models are proposed and tested. In the following discussion and in section 6 an attempt is made to arrive at the most realistic flow model, acknowledging however that the RTD curve may be represented by more than one flow scheme.

Due to the symmetrical shape of the reactor, it is assumed that the flow patterns in the two sides are the same. (This is why tracer is injected on one side only). We therefore need only look at one side of the reactor.

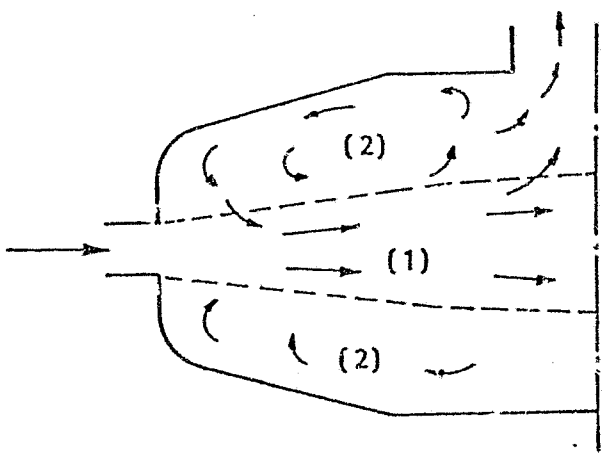


FIGURE 5.1 VISUALISATION OF FLOW PATTERNS

From the geometry of the reactor and from the flow visualisation tests, it is clear that two broadly differing flow regions can be distinguished. Region 1 is the high velocity turbulent diverging inlet jet, extending to under the outlet, where it impinges on the opposing jet. At impingement the jet is deflected laterally in all directions. Part of the air flows straight out the exit and part enters flow region 2 which surrounds the inlet jet. In region 2 the flow is more "mixed" than in region 1. Region 2 can be viewed as a zone of recirculation, the air being re-entrained by the inlet jet ("Recycle model"). Alternatively, region 2 can be seen as a well-mixed region (CSTR) exchanging fluid at the outlet of region 1 ("Bypass model"). It would be expected that recirculation would be more established in a reactor with large length/diameter ratio, as was seen in the flow visualization experiments for the two vessel lengths.

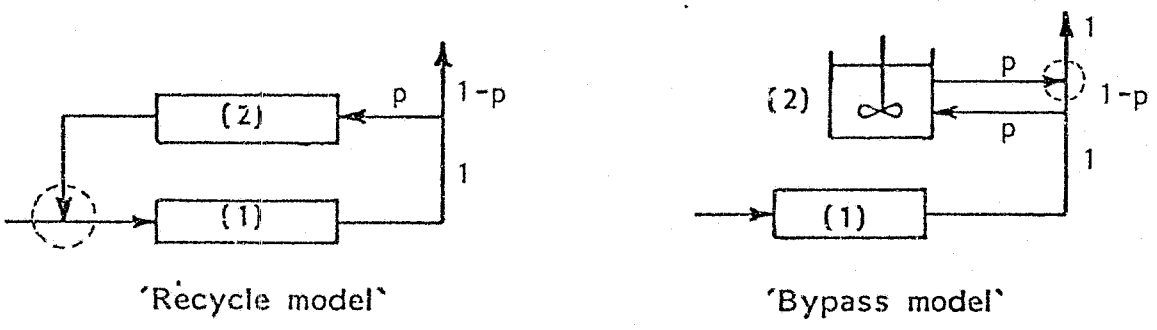


FIGURE 5.2 PROPOSED FLOW MODELS

Obviously these two models are gross approximations; a more realistic model would include several paths for exchange of fluid between the two regions. However, it is important not to introduce too many parameters into the model, as the model may become too flexible. An unrealistic multiparameter model could be forced to fit the response curve in this way. One should therefore aim for the simplest model which fits the data (4). This is illustrated and discussed further in section 6.

5.2 LAPLACE TRANSFORMS

The transfer function for a linear system is defined as:

$$F(s) = \frac{c_o(s)}{c_i(s)} = \mathcal{L}\{f(t)\} = \int_o^\infty f(t)\, \exp(-st)\, dt \qquad (5.1)$$

where $f(t)$ is the RTD function and $c_o(t)$ and $c_i(t)$ are the output and input concentration functions. $F(s)$ may be written in terms of $F_1(s)$ and $F_2(s)$ by mass balance, where

$F_1(s) = \mathcal{L}\{f_1(t)\}$ = transfer function of region 1

$F_2(s) = \mathcal{L}\{f_2(t)\}$ = transfer function of region 2

For the recycle model, a tracer mass balance over the point indicated by the dotted line in figure 5.2 yields:

$$(1-p)c_i(s) + pF_2(s)c_o(s) = c'(s)$$

where $c_o(s) = F_1(s)c'(s)$

Substituting $c'(s)$,

$$(1-p)c_i(s) + pF_2(s)c_o(s) = \frac{c_o(s)}{F_1(s)}$$

$$(1-p)F_1(s)c_i(s) + [pF_1(s)F_2(s) - 1]\, c_o(s) = 0$$

$$F(s) = \frac{c_o(s)}{c_i(s)} = \frac{(1-p)\ F_1(s)}{1 - pF_1(s)F_2(s)} \qquad (5.2)$$

where p = recycle fraction

The recycle ratio R is also sometimes used :

$$R = \frac{p}{1 - p}$$

For the bypass model, a balance over the point indicated in figure 5.2 yields:

$$(1-p)F_1(s)c_i(s) + pF_1(s)F_2(s)c_i(s) = c_o(s)$$

$$F(s) = \frac{c_o(s)}{c_i(s)} = (1-p)F_1(s) + pF_1(s)F_2(s)$$

$$F(s) = F_1(s)\ (1 - p + pF_2(s)) \qquad (5.3)$$

The following transfer functions are used for $F_1(s)$ and $F_2(s)$:

Ideal mixing (CSTR):

$$F_1\ (s) = \frac{1}{\tau_1 s + 1} \qquad (5.4)$$

where τ_1 = mean of $f_1(t)$

Mixed tanks in series (gamma distribution):

$$F_1(s) = \frac{1}{(\tau_1 s/n_1 + 1)^{n_1}} \qquad (5.5)$$

where τ_1 = mean of $f_1(t)$

n_1 = number of stirred tanks

σ_1^2 ≙ variance of $f_1(t) = \tau_1^2/n_1$

Taylor's axial dispersion model : (see appendix VIII.3)

$$F_1(s) = \exp\left[\frac{\tau_1^2}{\sigma_1{}^2} - \sqrt{\frac{\tau_1{}^4}{\sigma_1{}^4} + \frac{2\tau_1{}^3 s}{\sigma_1{}^2}}\right] \qquad (5.6)$$

5.3 MODEL FOURIER COEFFICIENTS

The Fourier coefficients of the mathematical model can be calculated from the Laplace Transform by rewriting equations (4.6) and (4.7) as

$$b_0 = 1/2T \qquad (5.7)$$

$$a_n = -(1/T)\ \mathrm{Im}\,[F(iw)] \qquad (5.8)$$

$$b_n = (1/T)\ \mathrm{Re}\,[F(iw)] \qquad (5.9)$$

where Re [ ] and Im [ ] are the real and imaginary parts of the complex number F(iw) at any frequency w.

Equations for the model Fourier coeffcients are derived in Appendices VII and IX, and the results are summarised here.

Recycle model with a Gamma distribution in each loop :

Independent variables : $p, \tau_1, \sigma_1^2, \sigma_2^2$

Other variables : $\tau_2 = \dfrac{(1-p)\,\tau - \tau_1}{p}$ (see appendix VII)

$$\frac{V_1}{V} = \frac{\tau_1}{\tau_1 + p\,\tau_2}$$

$$F(iw) = \frac{(1-p)r_2^{n_2}[r_1^{n_1} r_2^{n_2}\cos(n_1\theta_1) - p\cos(n_2\theta_2)] + i(1-p)r_2^{n_2}[-r_1^{n_1} r_2^{n_2}\sin(n_1\theta_1) - p\sin(n_2\theta_2)]}{r_1^{2n_1} r_2^{2n_2} - 2pr_1^{n_1} r_2^{n_2}\cos(n_1\theta_1 + n_2\theta_2) + p^2} \qquad (5.10)$$

$$a_n = \frac{1}{T}\,\frac{(1-p)r_2^{n_2}[r_1^{n_1} r_2^{n_2}\sin(n_1\theta_1 + p\sin(n_2\theta_2)}{r_1^{2n_1} r_2^{2n_2} - 2pr_1^{n_1} r_2^{n_2}\cos(n_1\theta_1 + n_2\theta_2) + p^2} \qquad (5.11)$$

$$b_n = \frac{1}{T}\,\frac{(1-p)r_2^{n_2}[r_1^{n_1} r_2^{n_2}\cos(n_1\theta_1 - p\cos(n_2\theta_2)}{r_1^{2n_1} r_2^{2n_2} - 2pr_1^{n_1} r_2^{n_2}\cos(n_1\theta_1 + n_2\theta_2) + p^2} \qquad (5.12)$$

$$\text{where} \quad r_1 = \sqrt{\frac{\tau_1^2 w^2}{n_1^2} + 1} \qquad \theta_1 = \tan^{-1}\left(\frac{\tau_1 w}{n_1}\right)$$
$$r_2 = \sqrt{\frac{\tau_2^2 w^2}{n_2^2} + 1} \qquad \theta_2 = \tan^{-1}\left(\frac{\tau_2 w}{n_2}\right) \qquad (5.13)$$

$n_1 = \dfrac{\tau_1^2}{\sigma_1^2}$ = equivalent number of mixed tanks in region 1

$n_2 = \dfrac{\tau_2^2}{\sigma_2^2}$ = equivalent number of mixed tanks in region 2

n_1 and n_2 need not be whole numbers

The above model equations can be used for the following less general models :

- Plug flow in region 1 and/or 2 : n_1 and/or $n_2 \rightarrow \infty$
  ($r_1 = r_2 = 1$, $\theta_1 = \theta_2 = 0$, $n_1\theta_1 = w\tau_1$, $n_2\theta_2 = w\tau_2$)

- Instantaneous recycle : $\tau_2 = 0$
  ($r_2 = 1$, $\theta_2 = 0$)

- Gamma distribution only : $p = 0$, $\tau_2 = 0$

Recycle model with axial dispersion in both loops :

Independent variables : p, τ_1, σ_1^2, σ_2^2

$$F(iw) = \frac{(1-p)\exp a_1 \left[\cos\beta_1 - p\exp(a_1+a_2)\cos\beta_2 - i\sin\beta_1 - ip\exp(a_1+a_2)\sin\beta_2\right]}{1 - 2p\exp(a_1+a_2)\cos(\beta_1+\beta_2) + p^2\exp(2a_1+2a_2)} \qquad (5.14)$$

$$a_n = \frac{1}{T}\,\frac{(1-p)\exp a_1 \left[\sin\beta_1 + p\exp(a_1+a_2)\sin\beta_2\right]}{1 - 2p\exp(a_1+a_2)\cos(\beta_1+\beta_2) + p^2\exp(2a_1+2a_2)} \qquad (5.15)$$

$$b_n = \frac{1}{T}\,\frac{(1-p)\exp a_1 \left[\cos\beta_1 - p\exp(a_1+a_2)\cos\beta_2\right]}{1 - 2p\exp(a_1+a_2)\cos(\beta_1+\beta_2) + p^2\exp(2a_1+2a_2)} \qquad (5.16)$$

where
$$a_1 = A_1 - \alpha_1$$
$$a_2 = A_2 - \alpha_2$$

$$\alpha_1 = r_1\cos\theta_1 \qquad \beta_1 = r_1\sin\theta_1$$
$$\alpha_2 = r_2\cos\theta_2 \qquad \beta_2 = r_2\sin\theta_2$$

$$r_1 = (A_1^4 + B_1^2)^{\frac{1}{4}} \qquad \theta_1 = 0{,}5\tan^{-1}(B_1/A_1^2)$$
$$r_2 = (A_2^4 + B_2^2)^{\frac{1}{4}} \qquad \theta_2 = 0{,}5\tan^{-1}(B_2/A_2^2)$$

$$A_1 = \tau_1^2/\sigma_1^2 \qquad B_1 = 2\tau_1^3 w/\sigma_1^2$$
$$A_2 = \tau_2^2/\sigma_2^2 \qquad B_2 = 2\tau_2^3 w/\sigma_2^2 \qquad (5.17)$$

Bypass model with region 1 a gamma distribution and region 2 a CSTR :

Independent variables : p, τ_1, σ_1^2

Other variables : $\tau_2 = (\tau - \tau_1)/p$

$$V_1/V = \tau_1/\tau$$

$$F(iw) = \frac{(1 + \tau_2^2 w^2 - p\tau_2^2 w^2)\cos n_1\theta_1 - p\tau_2 w \sin n_1\theta_1 - i\,[(1 + \tau_2^2 w^2 - p\tau_2^2 w^2)\sin n_1\theta_1 + p\tau_2 w \cos n_1\theta_1]}{r_1^{n_1/2}(1 + \tau_2^2 w^2)} \quad (5.18)$$

$$a_n = \frac{1}{T} \frac{[1 + (1-p)\tau_2^2 w^2]\sin n_1\theta_1 + p\tau_2 w \cos n_1\theta_1}{r_1^{n_1/2}(1 + \tau_2^2 w^2)} \quad (5.19)$$

$$b_n = \frac{1}{T} \frac{[1 + (1-p)\tau_2^2 w^2]\cos n_1\theta_1 - p\tau_2 w \sin n_1\theta_1}{r_1^{n_1/2}(1 + \tau_2^2 w^2)} \quad (5.20)$$

where $$r_1 = \frac{\tau_1^2 w^2}{n_1^2} + 1$$

$$\theta_1 = \tan^{-1}\left(\frac{\tau_1 w}{n_1}\right) \quad (5.21)$$

5.4 FITTING OF MATHEMATICAL MODELS

5.4.1 Least Squares Fit of Fourier Coefficients

The experimental Fourier coefficients have been determined in section 4.3, and we have seen how the theoretical coefficients of the model are derived, the latter set of coefficients being functions of the model parameters. The model parameters may now be varied, to give the best fit between the experimental and theoretical coefficients.

$$\text{Let} \quad f(t) = \sum_{n=1}^{\infty} a_n \sin(n\pi t/T) + \sum_{n=0}^{\infty} b_n \cos(n\pi t/T)$$

$$\text{and} \quad g(t) = \sum_{n=1}^{\infty} a_n' \sin(n\pi t/T) + \sum_{n=0}^{\infty} b_n' \cos(n\pi t/T)$$

where f(t) is the experimental RTD curve
and g(t) is the theoretical model RTD.

In order to obtain the closest fit between f(t) and g(t) in the time domain, we minimise S^2, where

$$S^2 = (1/2T) \int_0^{2T} [f(t) - g(t)]^2 \, dt$$

$$= (1/2T) \int_0^{2T} \left[\sum_{n=1}^{\infty} (a_n - a_n') \sin(n\pi t/T) + \sum_{n=0}^{\infty} (b_n - b_n') \cos(n\pi t/T) \right]^2 dt$$

$$= 0{,}5 \left[\sum_{n=1}^{\infty} (a_n - a_n')^2 + \sum_{n=1}^{\infty} (b_n - b_n')^2 \right] \qquad (5.22)$$

Doing a least-squares fit of the Fourier coefficients (equation 5.22) is thus equivalent to a least-squares fit in the time domain. The IMSL program "ZXMIN" which uses a quasi-Newton minimisation routine (21,22) is used to minimise S^2 and produce the corresponding model parameters. (See appendices XI.5, XI.6 and XI.7 for the various computer programs).

A measure of how well the model fits the experimental RTD curve is given by the average difference between the experimental and theoretical Fourier coefficients, i.e. $\sqrt{S^2/N}$, where the summations in equation (5.22) are summed to n = N (the truncation frequency).

5.4.2 Regeneration of the RTD Curve

The Fourier coefficients of the model evaluated in section 5.4.1 can be used to regenerate a Fourier series. This is then the RTD curve predicted by the model, obtained by numerical inversion the transfer function. This model RTD curve can now be compared with the experimental curve, and the degree of fit further examined. Fourier curves are generated in program F-ANAL (appendix XI.4).

5.4.3 Variation of Model Parameters with Frequency

If the mathematical model were to contain two parameters, these could be evaluated at different frequencies by solving the two Fourier coefficient equations using the experimental values for a_n and b_n. However, the models used in this work contain three to four parameters, which can therefore not be evaluated at a single frequency. Instead, a least-squares fit is done over a few Fourier coefficients at a time (five are used here) at increasing frequency, using the same technique as in section 5.4.1. Thus the model parameters are evaluated over consecutive frequency bands. For a model which fits the data well, the parameters would be expected to remain approximately constant, i.e. independent of frequency. This method can therefore be used as a criterion for choosing between competing models.

Doing a least-squares fit of the Fourier coefficients (equation 5.22) is thus equivalent to a least-squares fit in the time domain. The IMSL program "ZXMIN" which uses a quasi-Newton minimisation routine (21,22) is used to minimise S^2 and produce the corresponding model parameters. (See appendices XI.5, XI.6 and XI.7 for the various computer programs).

A measure of how well the model fits the ex, ntal RTD curve is given by the average difference between the experimental and theoretical Fourier coefficients, i.e. $\sqrt{S^2/N}$, where the summations in equation (5.22) are summed to n = N (the truncation frequency).

5.4.2 Regeneration of the RTD Curve

The Fourier coefficients of the model evaluated in section 5.4.1 can be used to regenerate a Fourier series. This is then the RTD curve predicted by the model, obtained by numerical inversion the transfer function. This model RTD curve can now be compared with the experimental curve, and the degree of fit further examined. Fourier curves are generated in program F-ANAL (appendix XI.4).

5.4.3 Variation of Model Parameters with Frequency

If the mathematical model were to contain two parameters, these could be evaluated at different frequencies by solving the two Fourier coefficient equations using the experimental values for a_n and b_n. However, the models used in this work contain three to four parameters, which can therefore not be evaluated at a single frequency. Instead, a least-squares fit is done over a few Fourier coefficients at a time (five are used here) at increasing frequency, using the same technique as in section 5.4.1. Thus the model parameters are evaluated over consecutive frequency bands. For a model which fits the data well, the parameters would be expected to remain approximately constant, i.e. independent of frequency. This method can therefore be used as a criterion for choosing between competing models.

6. RESULTS OF MATHEMATICAL MODEL FITTING

6.1 Long Reactor

The flow visualization experiments and the shape of the experimental RTD curve suggest that the recycle model be tested first in this case. Least squares fits of the Fourier coefficients are done, as described in section 5.4.1. Methods described in appendices VII and X are used to obtain first estimates of the model parameters. By using careful estimates, the minimisation procedure converged in each case.

Values of the model parameters giving closest fit of the recycle model with a gamma distribution (tanks-in-series) in each loop are given in table 6.1.

The value of $\sqrt{S^2/N}$ gives the average difference between the experimental and theoretical Fourier coefficients and is in all cases very small compared to the values of the coefficients. Figure 6.1 shows an example (run 5) of how closely the theoretical coefficients (dotted lines) fit the experimental values. It can clearly be seen how the experimental curve is affected by noise at high frequency.

The first two independent variables in table 6.1 are seen to remain constant, the differences between runs being arbitrary. The other two independent variables, namely the two variances, differ considerably (especially σ_2^2/τ_2^2). This is because the variances are of secondary importance, small changes in their values not affecting the shape of the RTD curve significantly.

FIGURE 6.1. TYPICAL LEAST SQUARES FIT OF FOURIER COEFFICIENTS.

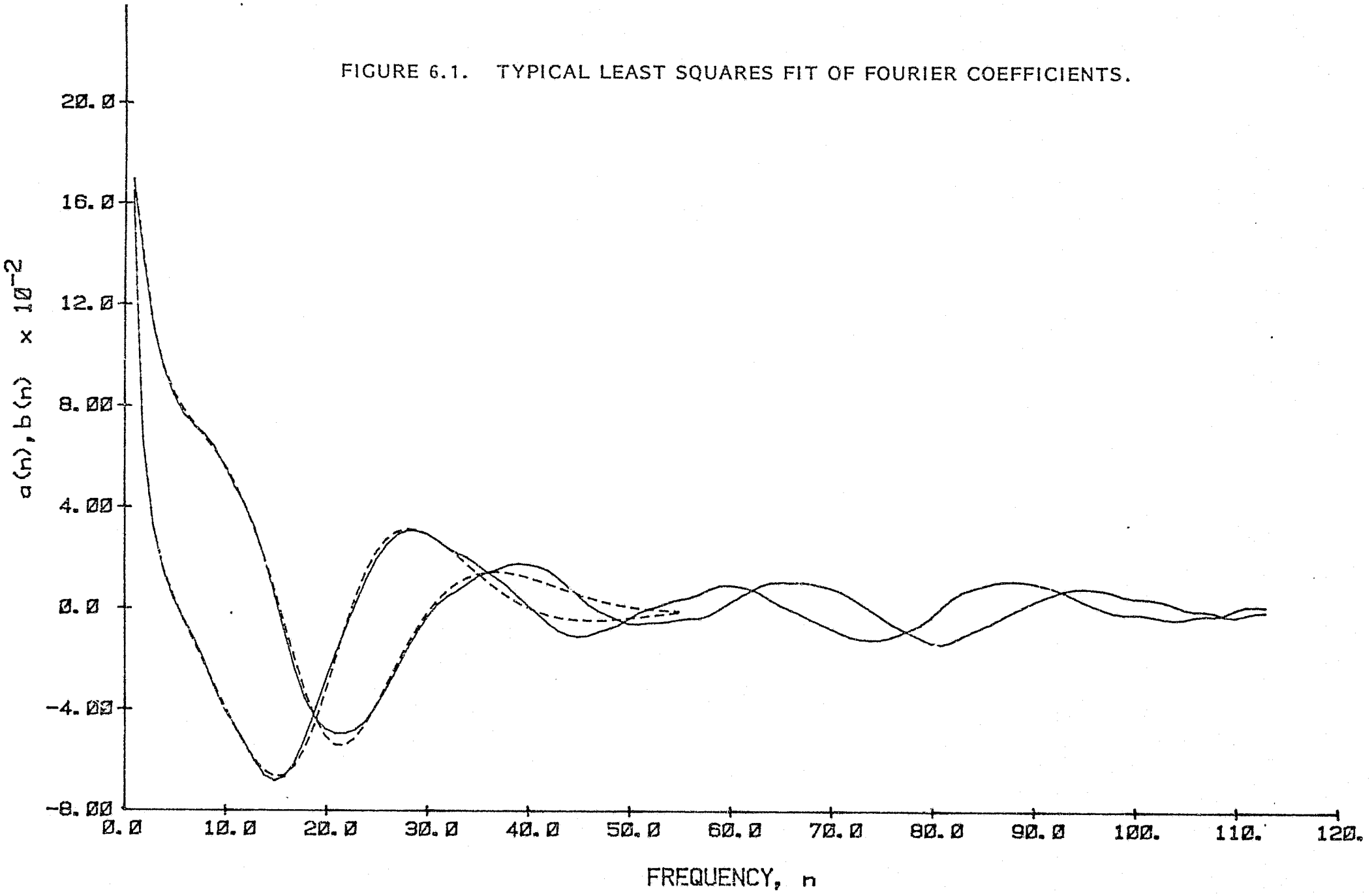


TABLE 6.1. MODEL PARAMETERS FOR LEAST-SQUARES FIT OF THE RECYCLE MODEL WITH A GAMMA DISTRIBUTION IN EACH LOOP

RUN	INDEPENDENT VARIABLES				$\sqrt{S^2/N}$
	p	τ_1	σ_1^2/τ_1^2	σ_2^2/τ_2^2	
1	0,675	0,217	0,085	1,63	0,0057
2	0,726	0,204	0,100	0,90	0,0026
3	0,711	0,189	0,125	0,34	0,0049
4	0,738	0,174	0,083	0,99	0,0051
5	0,685	0,207	0,067	1,16	0,0030

RUN	OTHER VARIABLES (DEPENDENT)				
	τ_2	n_1	n_2	R	V_1/V
1	0,142	11,7	0,61	2,06	0,694
2	0.087	10,0	1,11	2,65	0,764
3	0,131	8,0	2,98	2,46	0,670
4	0,109	12,1	1,01	2,82	0,684
5	0,149	14,9	0,86	2,17	0,670

Using different half loop distributions ($F_1(s)$ and $F_2(s)$) should therefore not affect the values of the primary variables (τ_1 and p) significantly. This is shown by fitting a recycle model with axial dispersion in each loop, resulting in the parameters in table 6.2. Dimensionless variances are used as parameters instead of dispersion coefficients or number of stirred tanks in series, so that easy comparison may be made. The degree of fit ($\sqrt{S^2/N}$) is approximately equal for the above two recycle models.

TABLE 6.2. MODEL PARAMETERS FOR LEAST-SQUARES FIT OF THE RECYCLE MODEL WITH AXIAL DISPERSION IN EACH LOOP

RUN	INDEPENDENT VARIABLES				$\sqrt{S^2/N}$	DEPENDENT VARIABLES		
	p	τ_1	$\frac{\sigma_1^2}{\tau_1^2}$	$\frac{\sigma_2^2}{\tau_2^2}$		τ_2	R	V_1/V
1	0,654	0,228	0,103	1,30	0,0048	0,160	1,89	0,685
2	0,707	0,216	0,123	0,55	0,0022	0,098	2,41	0,758
3	0,692	0,203	0,155	0,18	0,0039	0,141	2,25	0,674
4	0,721	0,183	0,102	0,67	0,0045	0,122	2,58	0,675
5	0,675	0,213	0,076	1,28	0,0034	0,156	2,08	0,670

The Fourier coefficients from the least-squares fits are used to generate the theoretical model RTD curves. These curves are now compared with the experimental curves. Examples are shown for runs 2 and 5 in figures 6.2 to 6.8. The theoretical curves are shown with dotted lines. Equally good fits are obtained for the gamma distribution and axial dispersion versions of the recycle model.

As the variance in region 2 (σ_2^2/τ_2^2) is of lesser importance and is equal to one on average, a simpler 3-parameter recycle model is proposed with region 2 represented by one CSTR (for a CSTR, $\sigma^2/\tau^2=1/n=1$). The resulting parameters of a least-squares fit of this model are shown in table 6.3. The results are very similar to table 6.1 and the RTD curve fits are practically as good. Note that the area under the first peak of the RTD curve given in table 3.5 very nearly equals 1-p (see appendix VII).

The theoretical model RTD curve fits for all the runs are drawn on one set of axes for each of the 3 recycle model variations in figures 6.9 to 6.11.

TABLE 6.2. MODEL PARAMETERS FOR LEAST-SQUARES FIT OF THE RECYCLE MODEL WITH AXIAL DISPERSION IN EACH LOOP

RUN	INDEPENDENT VARIABLES				$\sqrt{S^2/N}$	DEPENDENT VARIABLES		
	p	τ_1	$\frac{\sigma_1^2}{\tau_1^2}$	$\frac{\sigma_2^2}{\tau_2^2}$		τ_2	R	V_1/V
1	0,654	0,228	0,103	1,30	0,0048	0,160	1,89	0,685
2	0,707	0,216	0,123	0,55	0,0022	0,098	2,41	0,758
3	0,692	0,203	0,155	0,18	0,0039	0,141	2,25	0,674
4	0,721	0,183	0,102	0,67	0,0045	0,122	2,58	0,675
5	0,675	0,213	0,076	1,28	0,0034	0,156	2,08	0,670

The Fourier coefficients from the least-squares fits are used to generate the theoretical model RTD curves. These curves are now compared with the experimental curves. Examples are shown for runs 2 and 5 in figures 6.2 to 6.8. The theoretical curves are shown with dotted lines. Equally good fits are obtained for the gamma distribution and axial dispersion versions of the recycle model.

As the variance in region 2 (σ_2^2/τ_2^2) is of lesser importance and is equal to one on average, a simpler 3-parameter recycle model is proposed with region 2 represented by one CSTR (for a CSTR, $\sigma^2/\tau^2=1/n=1$). The resulting parameters of a least-squares fit of this model are shown in table 6.3. The results are very similar to table 6.1 and the RTD curve fits are practically as good. Note that the area under the first peak of the RTD curve given in table 3.5 very nearly equals 1-p (see appendix VII).

The theoretical model RTD curve fits for all the runs are drawn on one set of axes for each of the 3 recycle model variations in figures 6.9 to 6.11.

TABLE 6.3. MODEL PARAMETERS FOR LEAST-SQUARES FIT OF THE RECYCLE MODEL WITH A GAMMA DISTRIBUTION IN THE FORWARD LOOP AND A CSTR IN THE RECYCLE

	INDEPENDENT VARIABLES				DEPENDENT VARIABLES			
RUN	p	τ_1	σ_1^2/τ_1^2	$\sqrt{S^2/N}$	τ_2	n_1	R	V_1/V
1	0,671	0,218	0,088	0,0059	0,147	11,3	2,04	0,689
2	0,727	0,204	0,099	0,0026	0,086	10,1	2,66	0,766
3	0,729	0,184	0,111	0,0053	0,111	9,0	2,69	0,696
4	0,738	0,174	0,083	0,0051	0,109	12,1	2,82	0,684
5	0,685	0,207	0,068	0,0031	0,149	14,7	2,17	0,670

The "bypass model" with region 1 a gamma distribution and region 2 a CSTR was also fitted to the data, and the results are given in table 6.4

TABLE 6.4. MODEL PARAMETERS FOR LEAST-SQUARES FIT OF THE BYPASS MODEL

	INDEPENDENT VARIABLES					
RUN	p	τ_1	σ_1^2/τ_1^2	$\sqrt{S^2/N}$	τ_2	V_1/V
1	0,798	0,192	0,051	0,0038	0,964	0,200
2	0,847	0,176	0,063	0,0043	0,943	0,181
3	0,854	0,154	0,063	0,0052	0,963	0,158
4	0,844	0,154	0,045	0,0044	0,969	0,158
5	0,779	0,192	0,047	0,0049	1,013	0,196

Although the values of $\sqrt{S^2/N}$ are about the same as for the recycle models, examination of the RTD curve fit (figure 6.5) shows that the bypass model is a poorer model, as the second peak in the RTD is not modelled at all. The smaller values of $\tau_1, \sigma_1^2/\tau_1^2$ and V_1/V and larger p are as expected, as region 1 comprises only incoming fluid, all recycling being contained in region 2, for the bypass model.

FIGURE 6.2. RECYCLE MODEL WITH GAMMA DISTRIBUTIONS IN BOTH LOOPS - LONG REACTOR RUN 2.

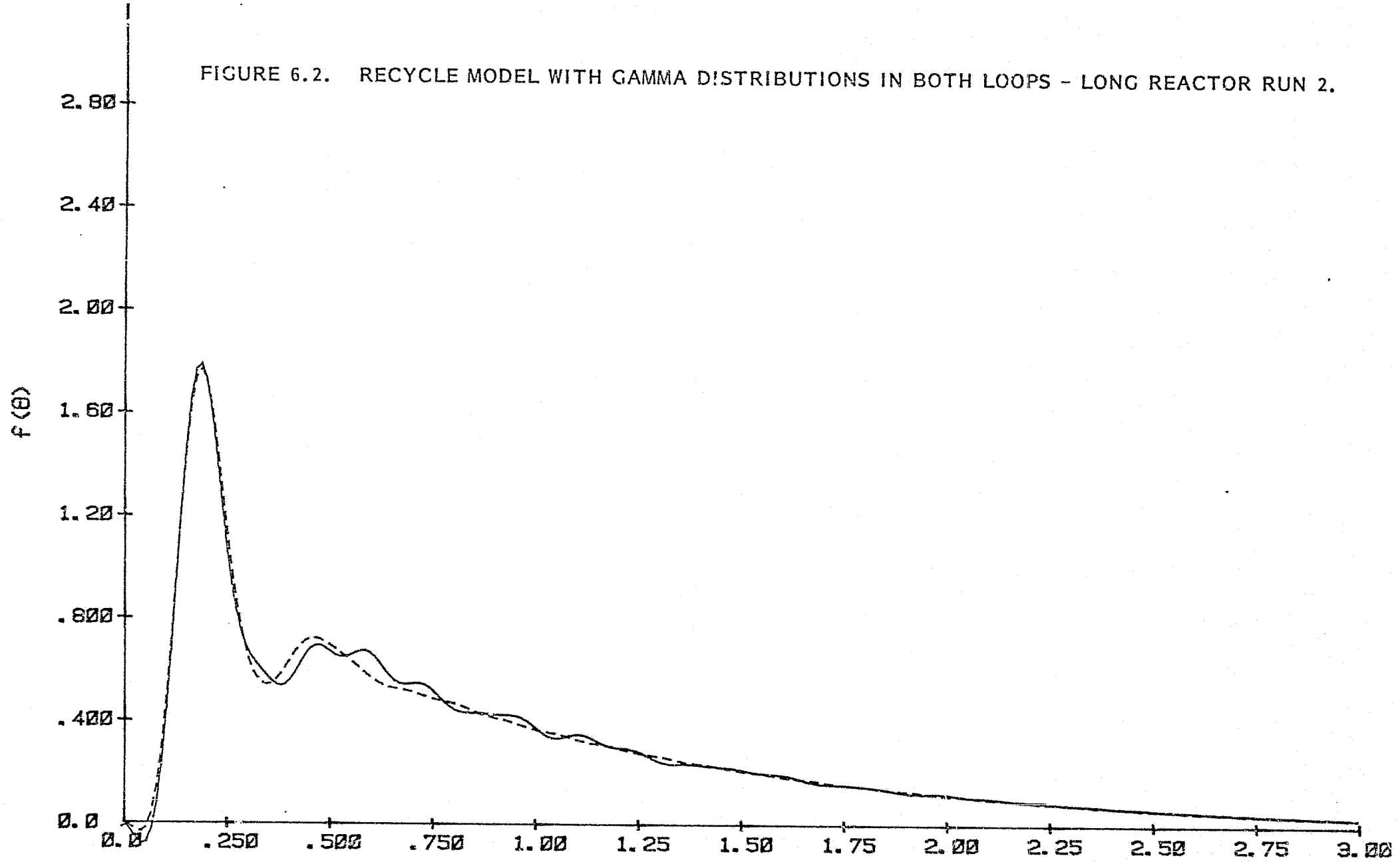


FIGURE 6.3. RECYCLE MODEL WITH AXIAL DISPERSION IN BOTH LOOPS - LONG REACTOR RUN 2.

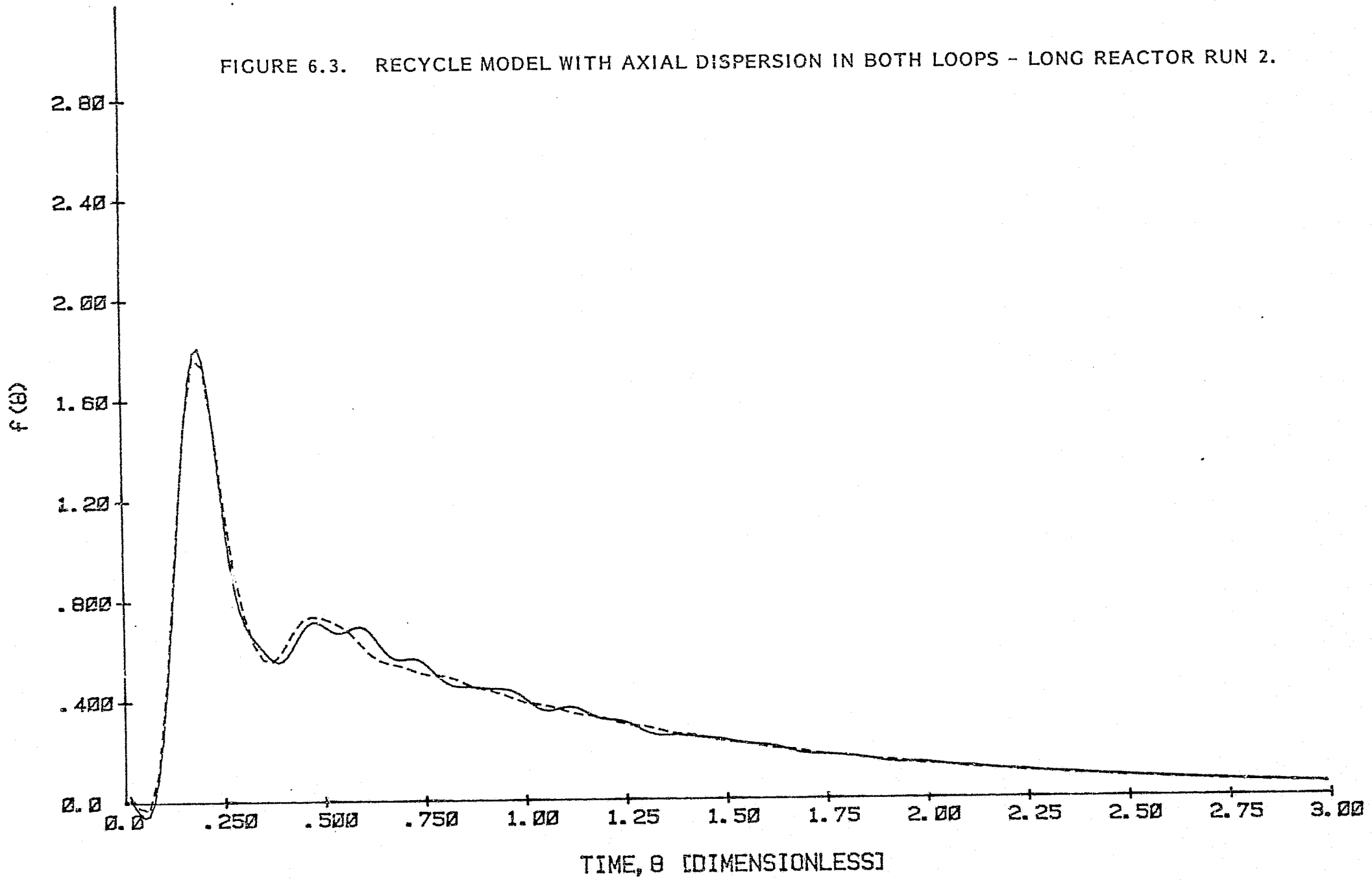


FIGURE 6.4. RECYCLE MODEL WITH A GAMMA DISTRIBUTION IN THE FORWARD LOOP AND A CSTR IN THE RECYCLE - LONG REACTOR RUN 2.

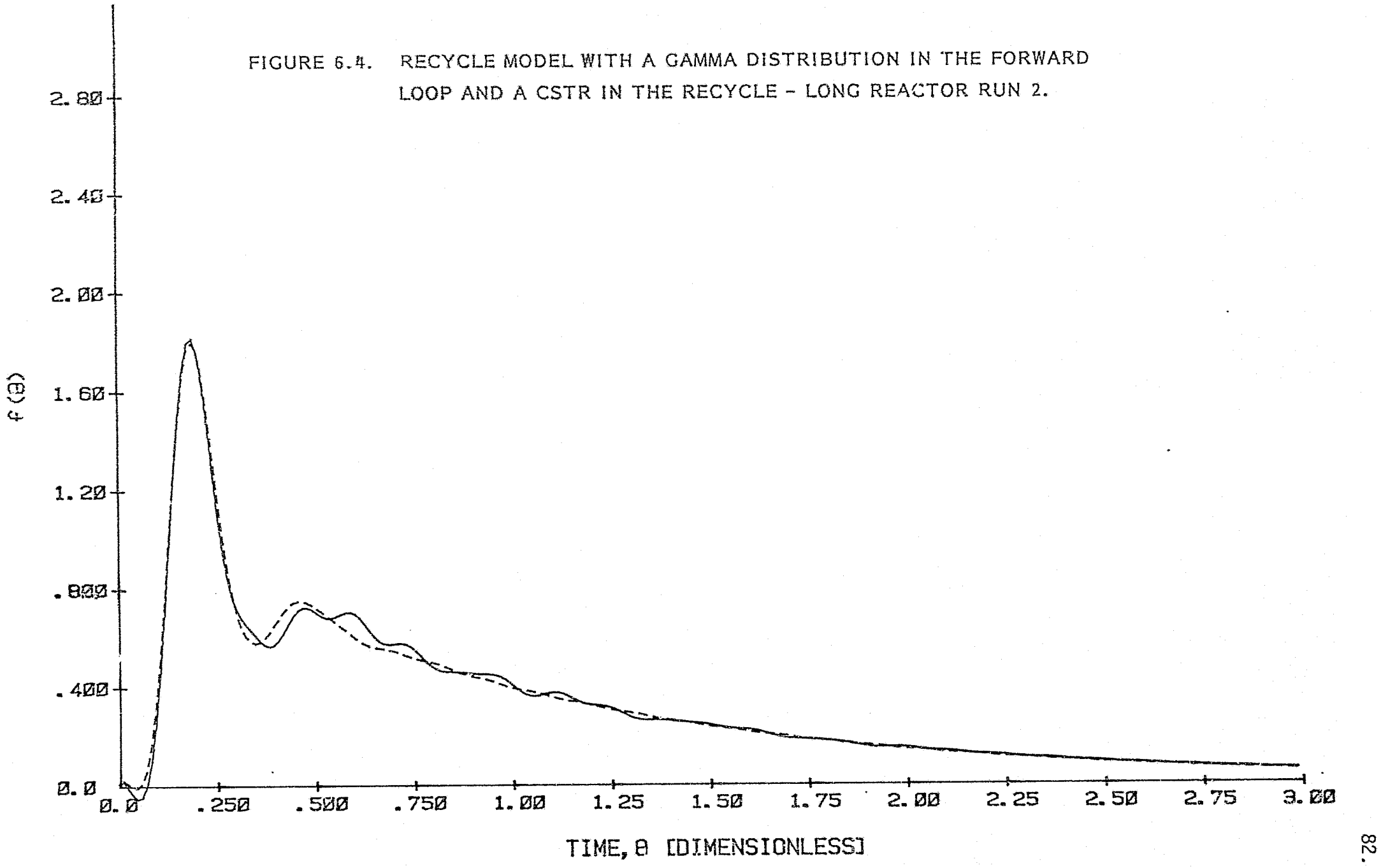


FIGURE 6.5. BYPASS MODEL - LONG REACTOR RUN 2.

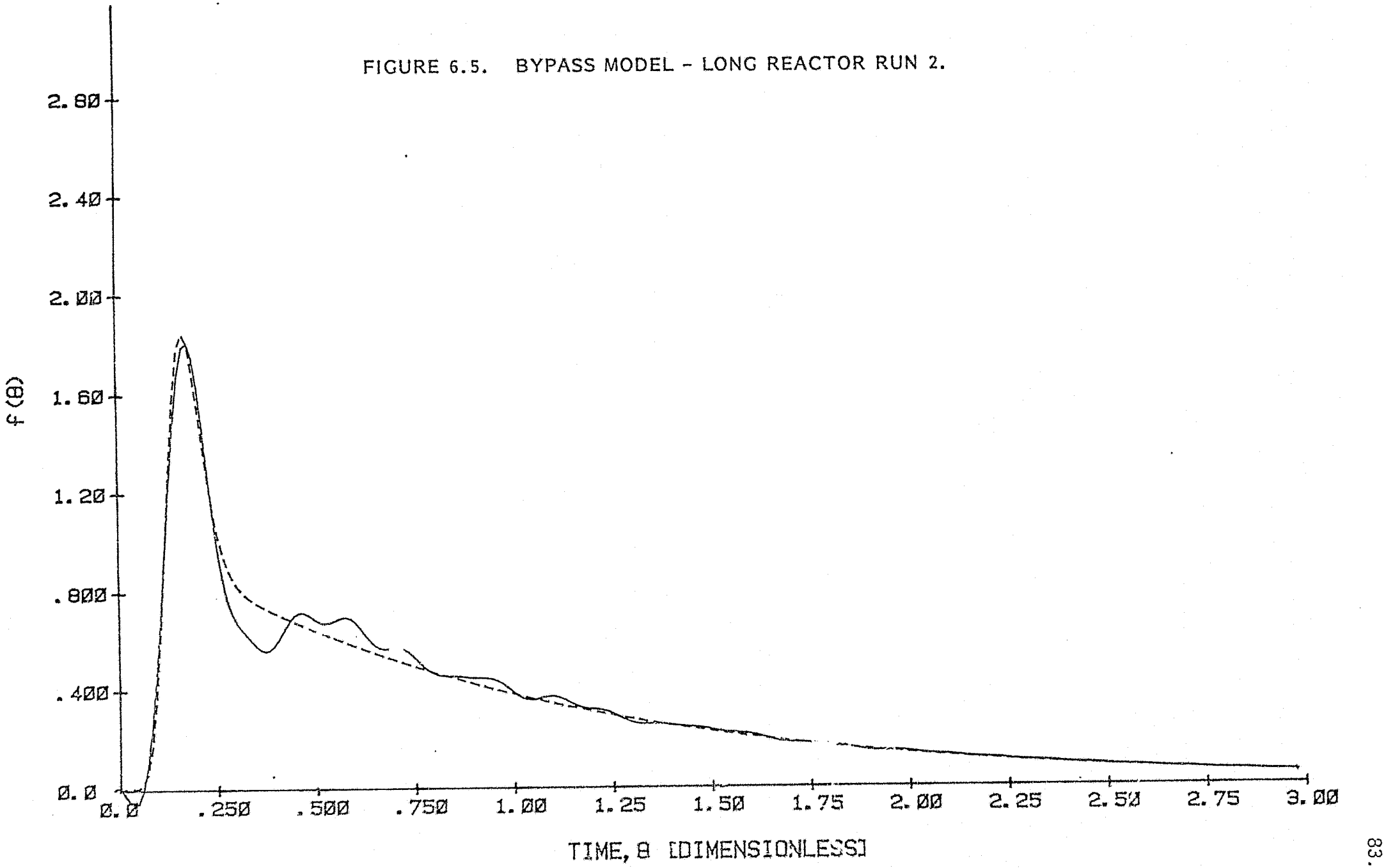


FIGURE 6.6. RECYCLE MODEL WITH GAMMA DISTRIBUTIONS IN BOTH LOOPS - LONG REACTOR RUN 5.

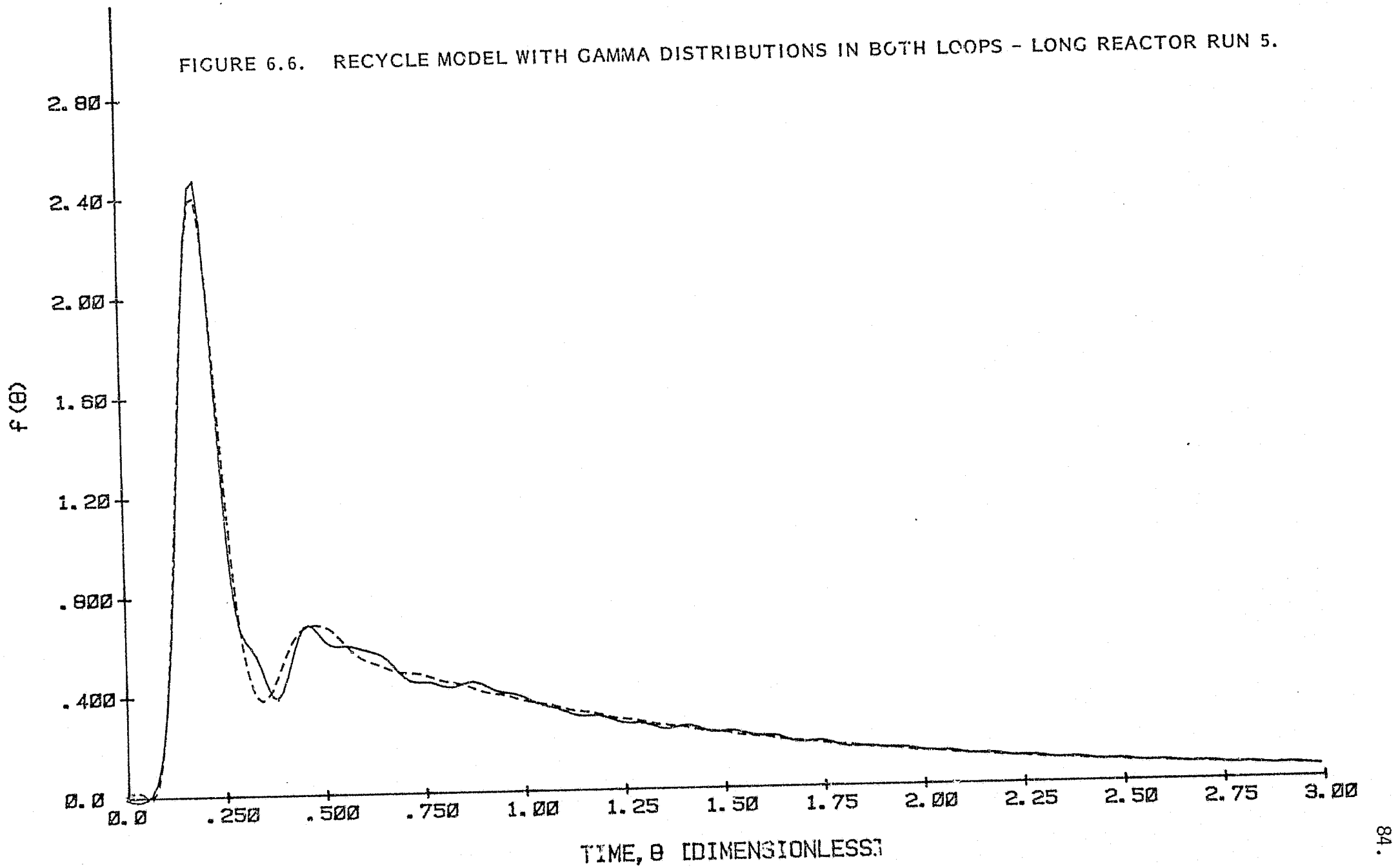


FIGURE 6.7. RECYCLE MODEL WITH AXIAL DISPERSION IN BOTH LOOPS - LONG REACTOR RUN 5.

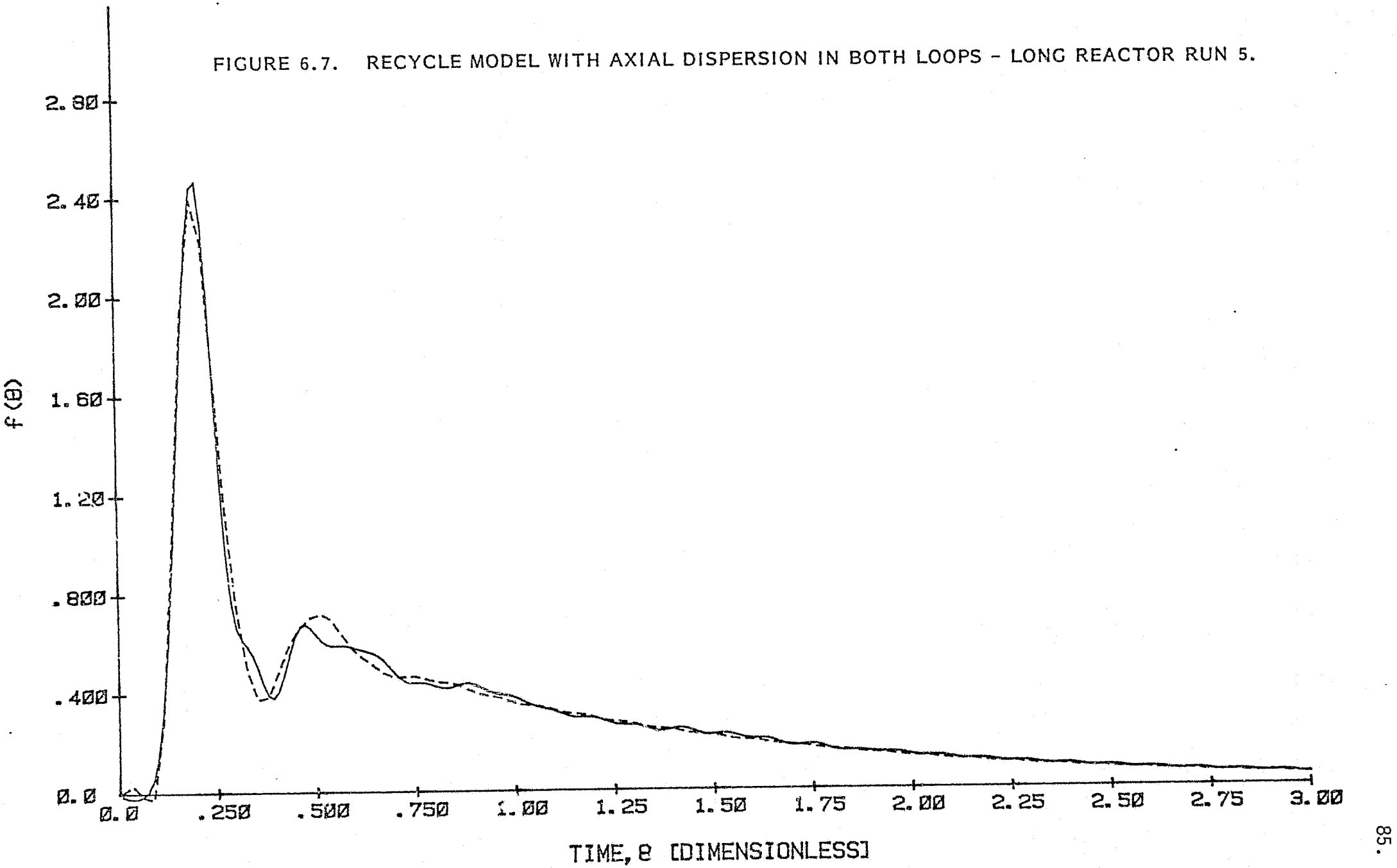


FIGURE 6.8. RECYCLE MODEL WITH A GAMMA DISTRIBUTION IN THE FORWARD LOOP AND A CSTR IN THE RECYCLE - LONG REACTOR RUN 5.

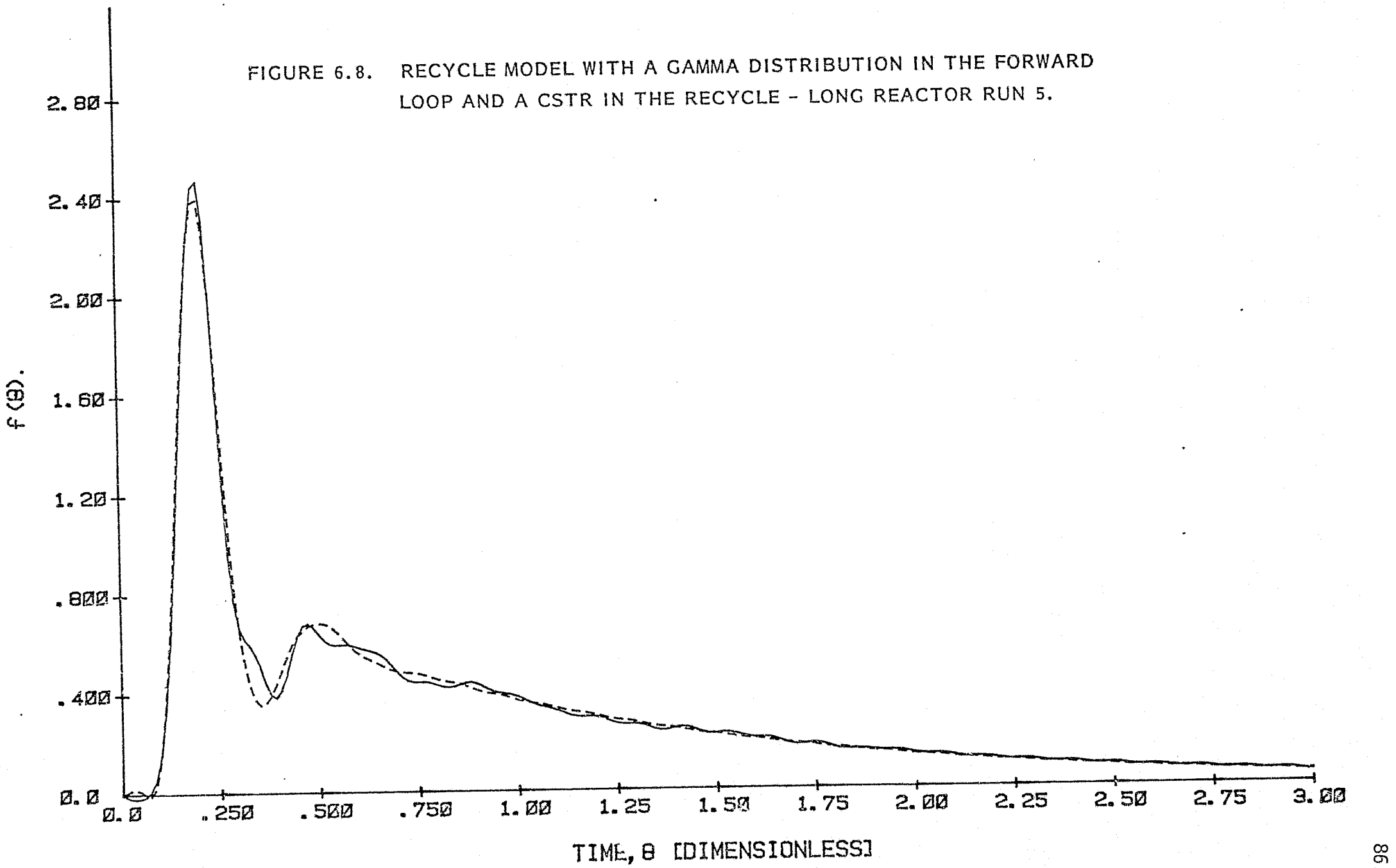


FIGURE 6.9. RECYCLE MODEL WITH GAMMA DISTRIBUTIONS IN BOTH LOOPS - LONG REACTOR.

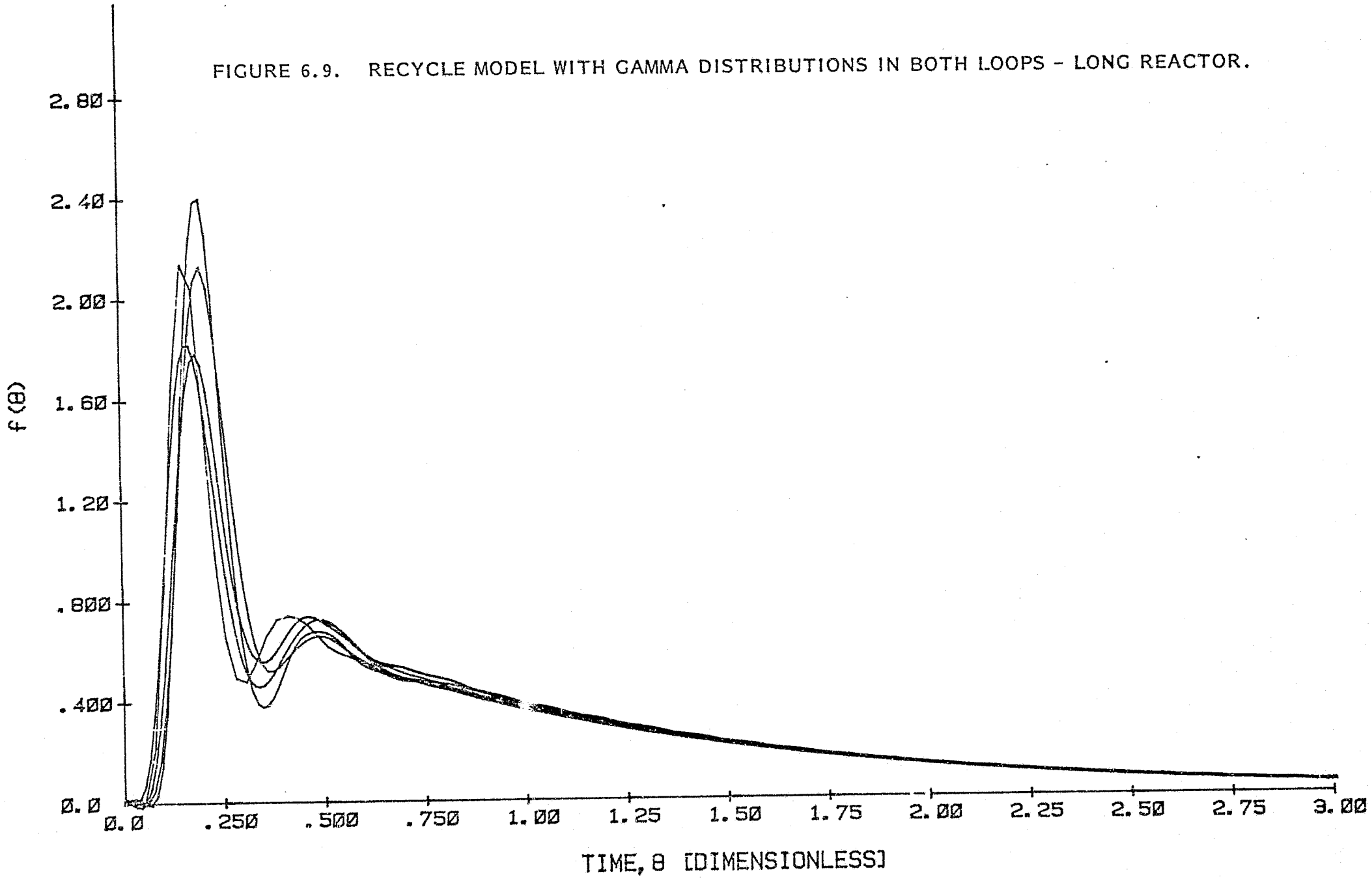


FIGURE 6.10. RECYCLE MODEL WITH AXIAL DISPERSION IN BOTH LOOPS – LONG REACTOR.

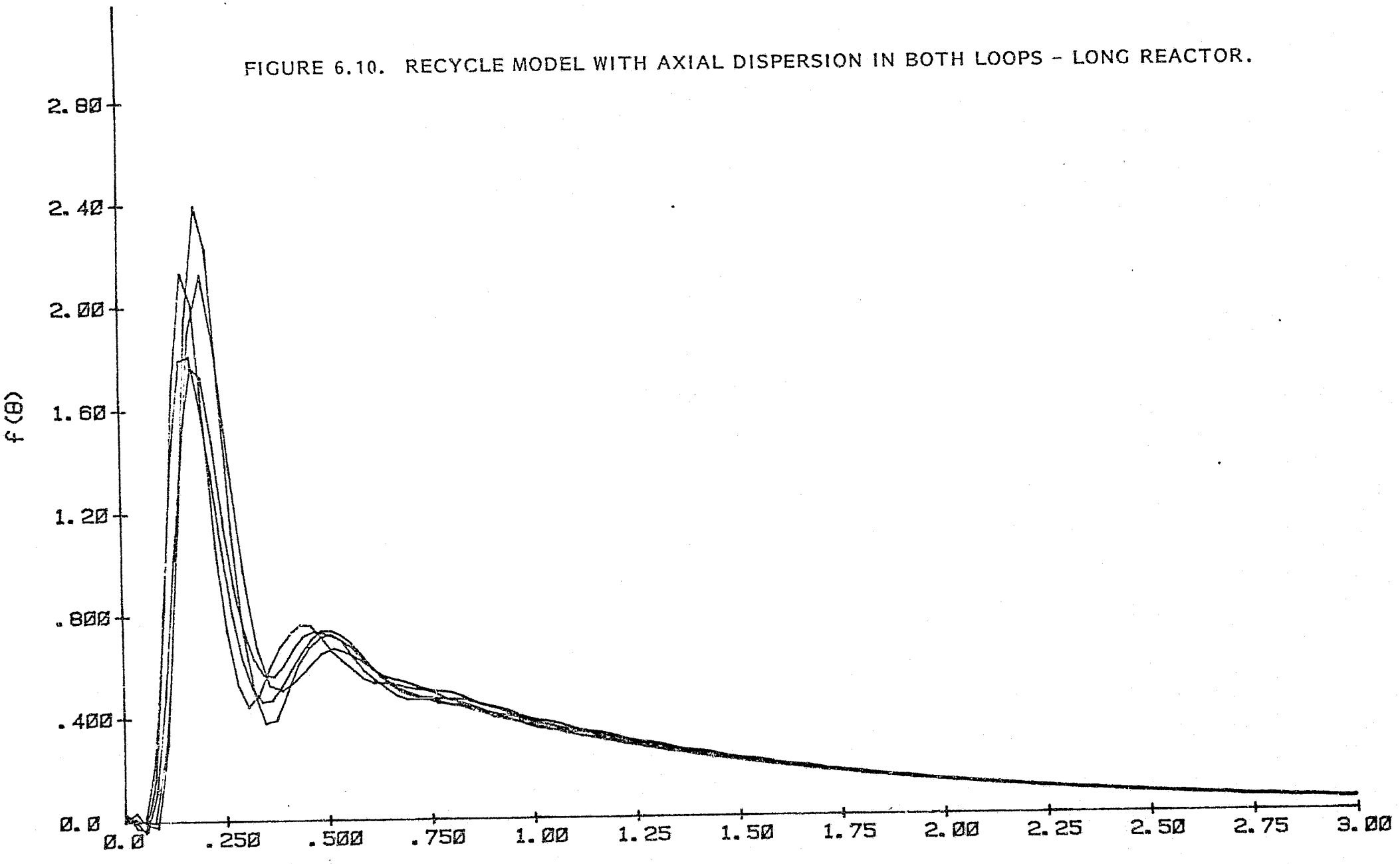
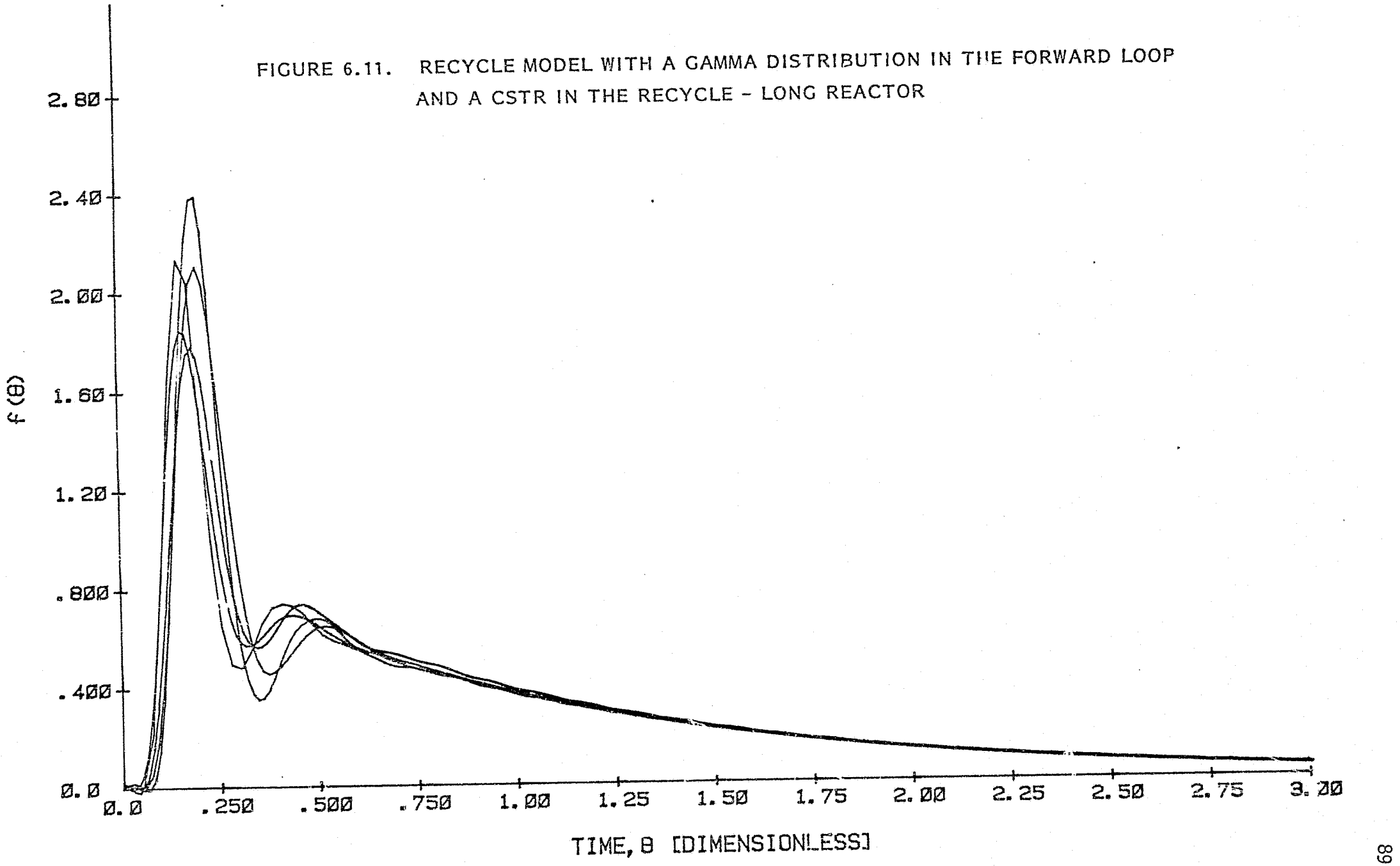


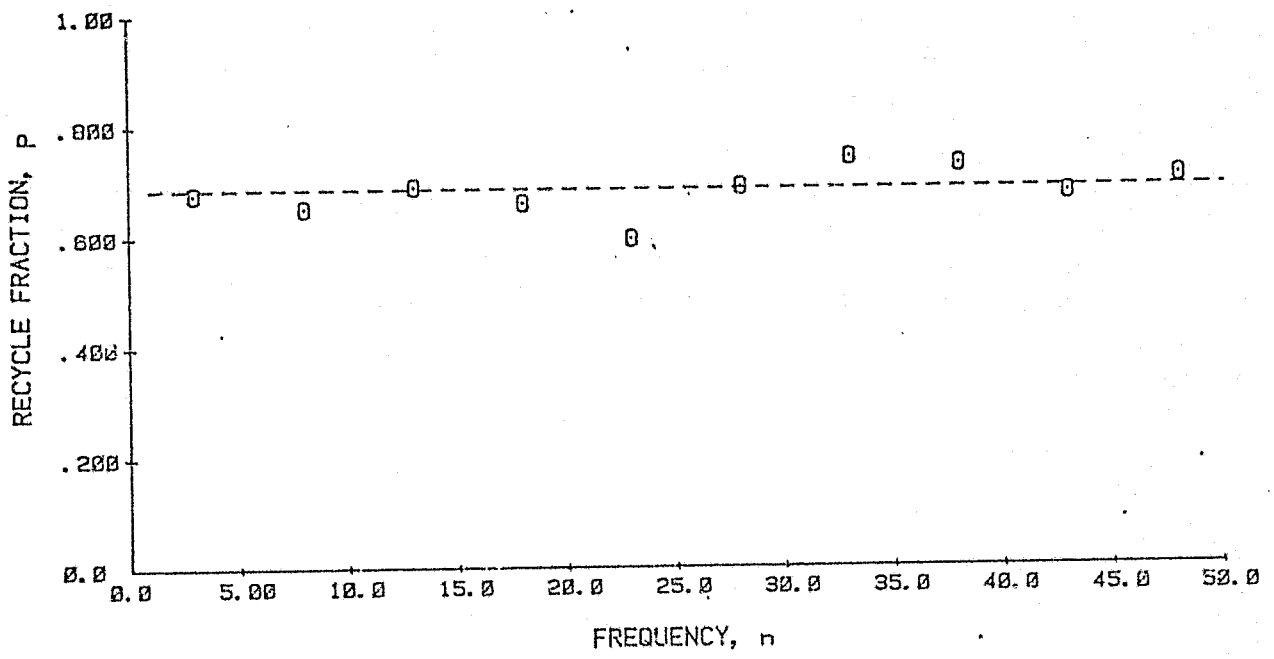
FIGURE 6.11. RECYCLE MODEL WITH A GAMMA DISTRIBUTION IN THE FORWARD LOOP AND A CSTR IN THE RECYCLE - LONG REACTOR



The different models can also be compared by looking at the parameter vs w plots, as discussed in section 5.4.3. Plots of the two primary variables, p and τ_1, are given in figures 6.12 to 6.15 for the various recycle models and the bypass model, using run 5 as an example. The other two variables (σ_1^2/τ_1^2 and σ_2^2/τ_2^2) are not plotted as the noise level is too high. The dotted lines shows the values of the parameters obtained from the least-squares fit.

It can be seen that the plots for the recycle model with either axial dispersion or a gamma distribution in each loop produce similar plots and therefore have equal merit. If the recycle model with one CSTR in the recycle (figure 6.14) is compared to the bypass model (figure 6.15), it can be seen that the parameters vary far less with frequency in the former case. The recycle model is therefore a much better representation of reality than the bypass model, in accordance with previous deduction. (Note that only models with an equal number of parameters can be compared by this method).

FIGURE 6.12. PARAMETERS OF THE RECYCLE MODEL WITH GAMMA DISTRIBUTIONS IN BOTH LOOPS - LONG REACTOR RUN 5.



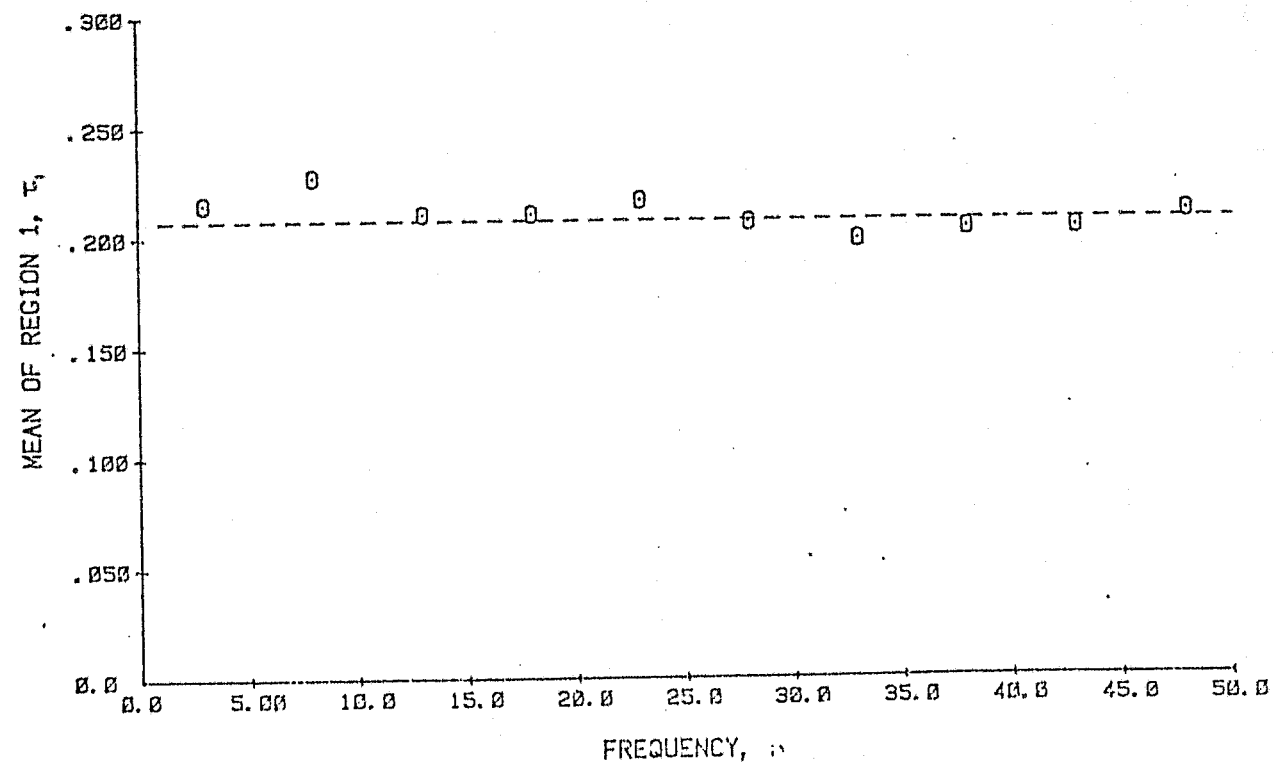
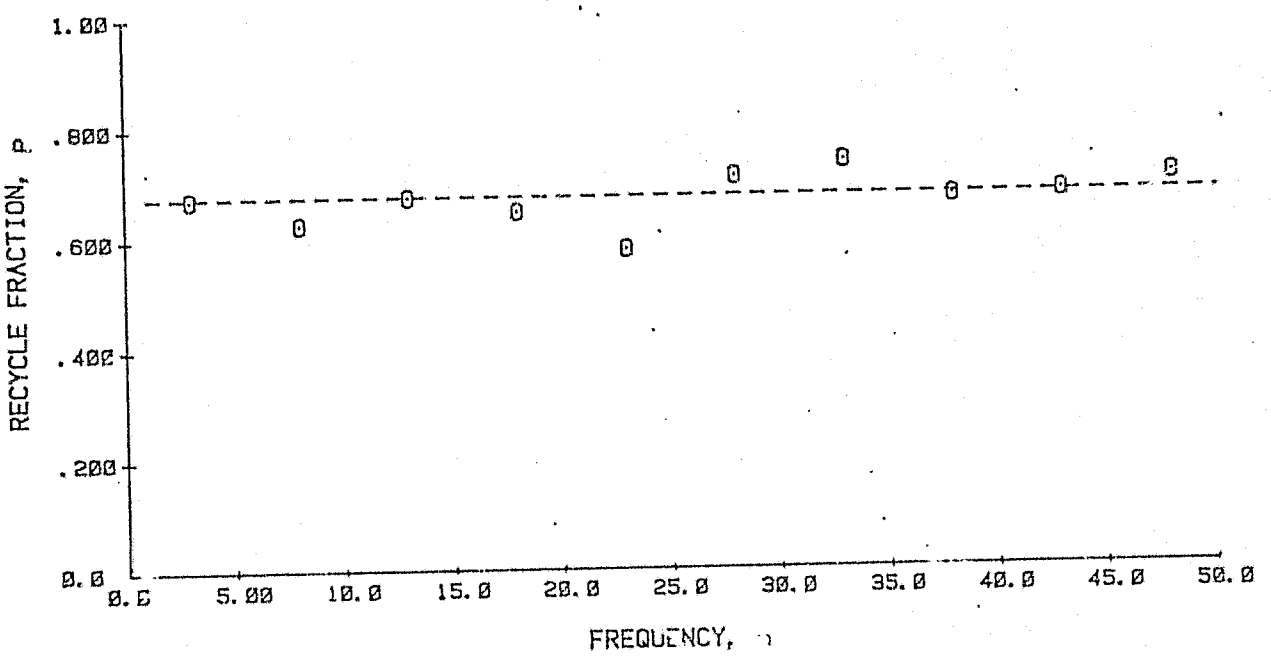


FIGURE 6.13. PARAMETERS OF THE RECYCLE MODEL WITH AXIAL DISPERSION IN BOTH LOOPS - LONG REACTOR RUN 5.



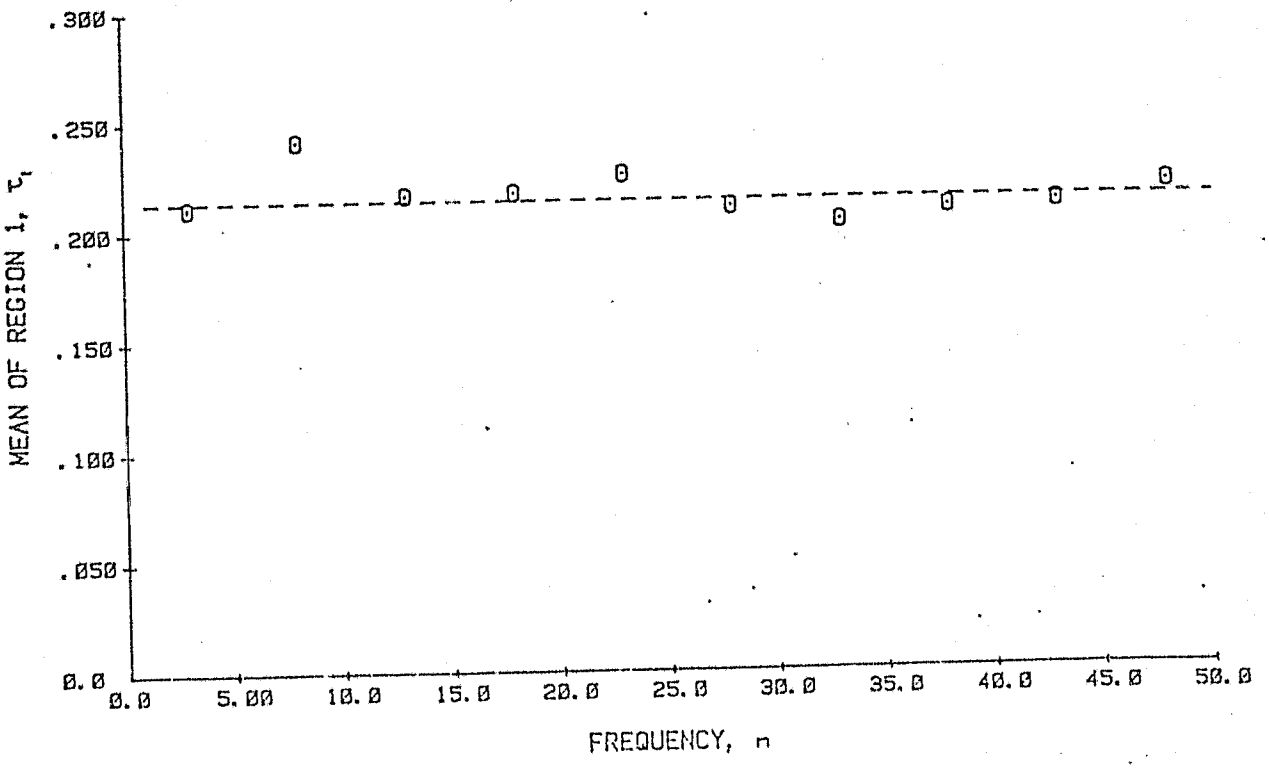
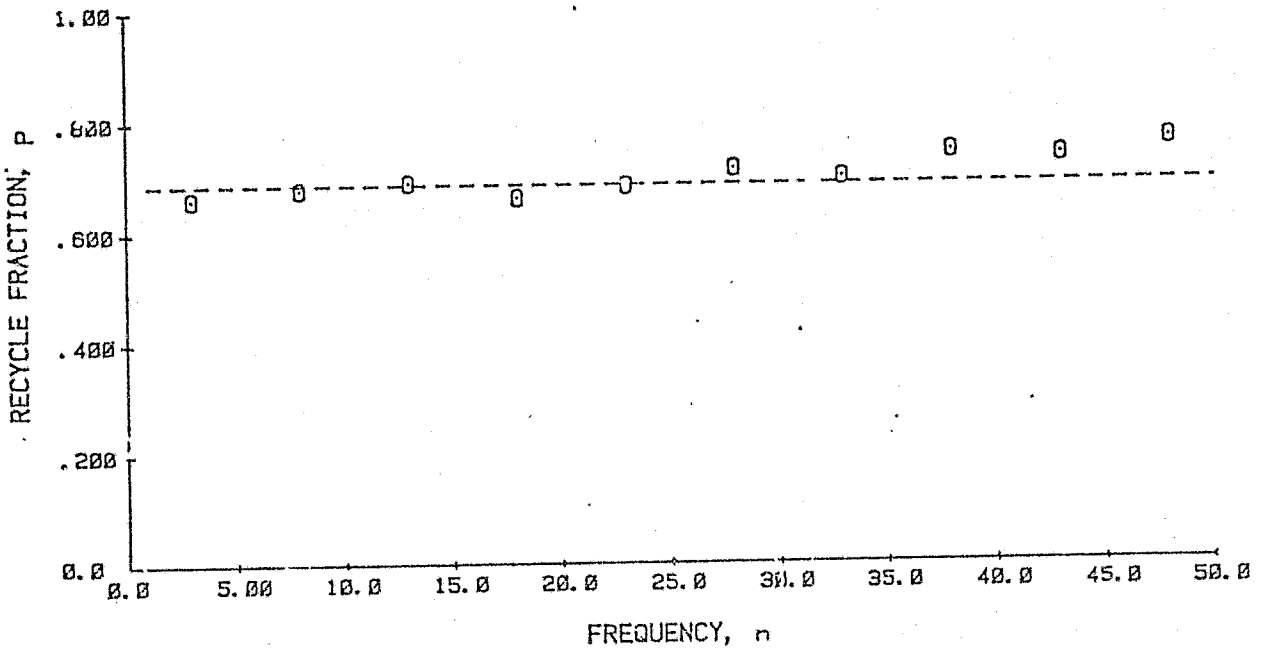


FIGURE 6.14. PARAMETERS OF THE RECYCLE MODEL WITH A GAMMA DISTRIBUTION IN THE FORWARD LOOP AND A CSTR IN THE RECYCLE - LONG REACTOR RUN 5.



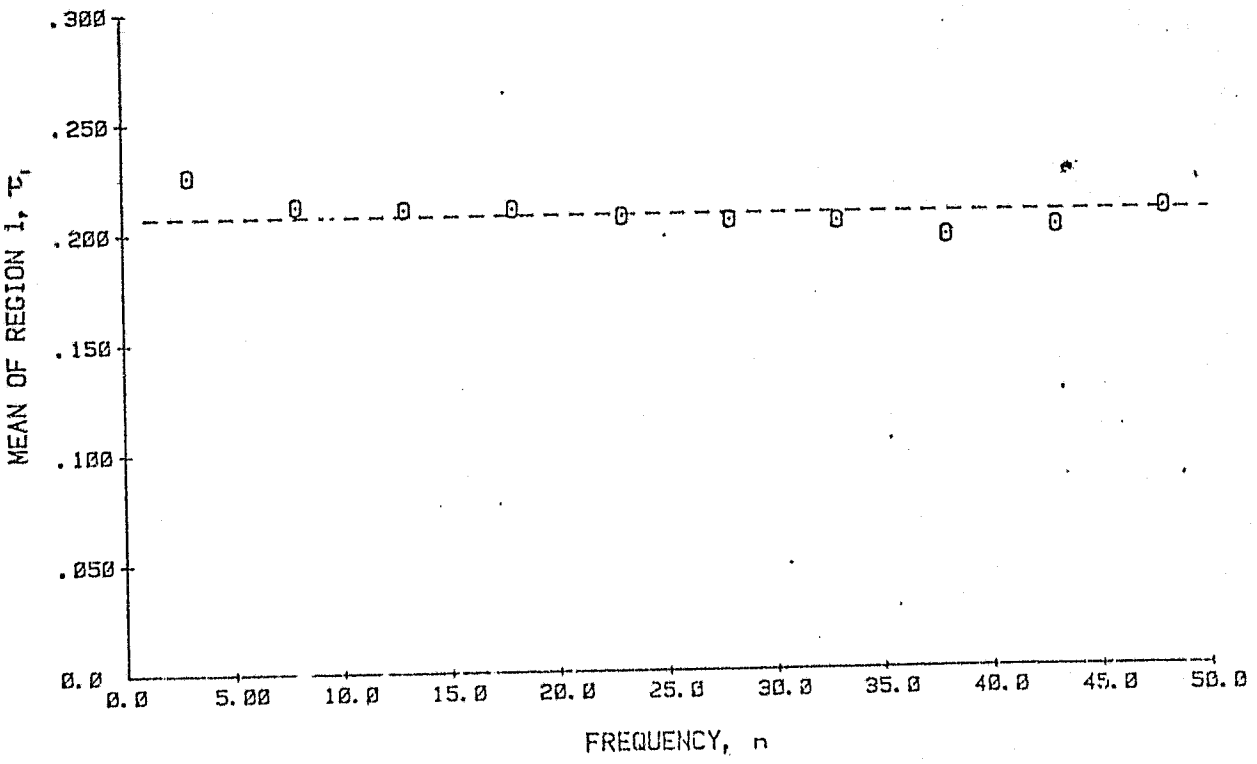
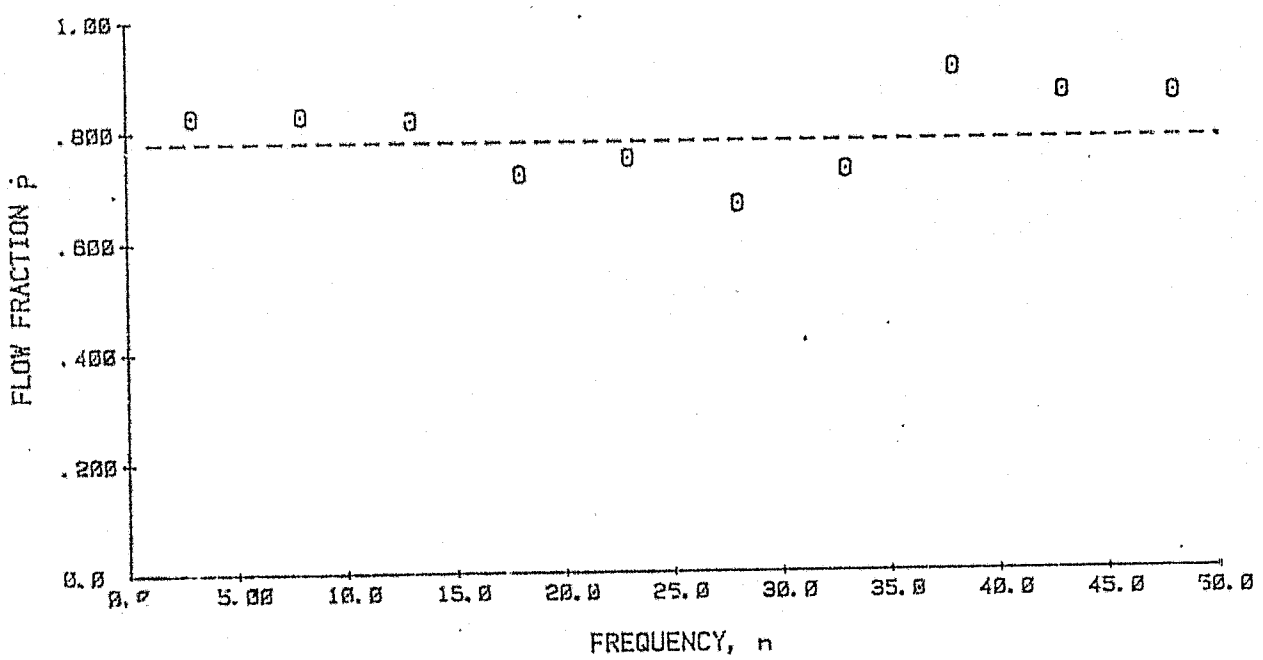
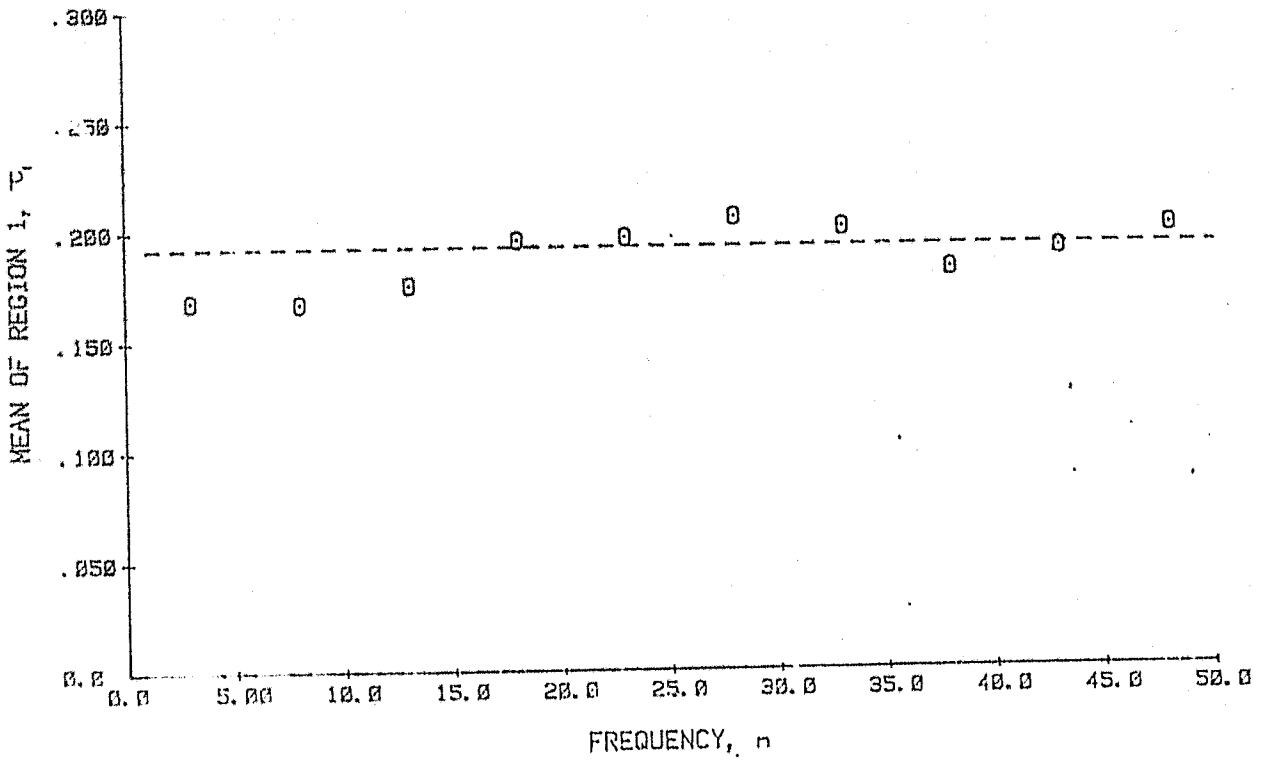


FIGURE 6.15. PARAMETERS OF THE BYPASS MODEL - LONG REACTOR RUN 5.





6.2 SHORT REACTOR

The RTD curves of the short reactor (figure 4.7) do not show the characteristic peaks associated with recycling, as was the case with the long reactor. The amplitude ratio plots also do not show the characteristic natural frequency. The curves are more scattered than in the case of the long reactor. It is therefore expected that there is not enough information in the RTD curves to extract four parameters.

The model parameters from a least-squares fit of the recycle model with a gamma distribution in each loop are given in table 6.5.

TABLE 6.5. MODEL PARAMETERS FOR LEAST-SQUARES FIT OF THE RECYCLE MODEL WITH A GAMMA DISTRIBUTION IN EACH LOOP

RUN	INDEPENDENT VARIABLES				$\sqrt{S^2/N}$	τ_2
	p	τ_1	$1/n_1$	$1/n_2$		
1	0,709	0,290	0,105	4155	0,0031	0,0031
2	0,931	0,197	0,079	-0,274	0,0025	-0,138
3	0,938	0,211	0,039	0,079	0,0048	-0,159
4	0,772	0,303	0,130	-0,877	0,0030	-0,098
5	0,834	0,250	0,082	-1,010	0,0021	-0,102

The above least-squares fit has produced impossible values for some of the parameters (τ_2 and n_2). This is clearly because we are trying to extract too many parameters. In figures 6.17 to 6.23 the regenerated model RTD curves are compared to the experimental curves, using runs 2 and 5 as examples. In figure 6.20 we can see how in the least-squares fit, the model has used a negative τ_2 to fit the two peaks which are actually due to noise only.

Using one CSTR in the recycle loop improves matters somewhat, resulting in very small negative values for τ_2. In the next trial, τ_2 was therefore set equal to zero; i.e. instantaneous recycle. For this model there are only two independent parameters, namely p and σ_1^2/τ_1^2; with the mean residence time τ equal to 1, we have $\tau_1 = 1-p$.

TABLE 6.6. MODEL PARAMETERS FOR LEAST SQUARES FIT OF THE RECYCLE MODEL WITH A GAMMA DISTRIBUTION IN THE FORWARD LOOP AND INSTANTANEOUS RECYCLE

RUN	INDEPENDENT VARIABLES		$\sqrt{S^2/N}$	τ_1
	p	σ_1^2/τ_1^2		
1	0,710	0,10	0,0031	0,290
2	0,609	0,20	0,0028	0,391
3	0,710	0,14	0,0063	0,290
4	0,583	0,22	0,0036	0,417
5	0,588	0,23	0,0057	0,412

The RTD curve fits of figures 6.18 and 6.21 show good fits for this model. However, comparison of the parameters for various runs shows large variations, although the RTD curves of the different runs are similar. Also, a large value of p corresponds with a small value of σ_1^2/τ_1^2 in each case. The conclusion is thus that the two parameters are not truly independent, as they have a large covariance. This is because both the parameters p and σ_1^2/τ_1^2 describe the degree of spread of the RTD curve of this model (both describe mixing).

One could therefore be led to suggest a model containing only one

of the above two parameters, i.e. either setting p=0 (an ordinary stirred-tanks-in-series model) or setting $\sigma_1^2/\tau_1^2=0$ (plug flow with recycle). A simple plug-flow-with-recycle model is however not realistic, considering the geometry, and it would produce an RTD with a series of discrete spikes.

Parameters for a least-squares fit of the tanks-in-series model (using two independent variables) are shown in table 6.7. A moment-matching analysis was also done in this case as only the first two moments are required. Figure 6.22 clearly shows that a tanks-in-series model fits the RTD curve poorly, not being able to model the initial delay, sharp rise and exponential decay.

TABLE 6.7. MODEL PARAMETERS OF TANKS-IN-SERIES MODEL

RUN	PARAMETERS FROM LEAST-SQUARES FIT		PARAMETERS FROM MOMENT ANALYSIS	
	τ	σ^2 / τ^2	τ	σ^2 / τ^2
1	0,839	0,557	1,00	0,746
2	0,875	0,495	1,00	0,638
3	0,893	0,514	1,00	0,640
4	0,844	0,477	1,00	0,684
5	0,858	0,484	1,00	0,656

Probably the simplest model which could reasonably represent the RTD curve is a plug flow region followed by a CSTR. The plug flow would produce the initial delay in the RTD curve and the CSTR would model the exponential decay.

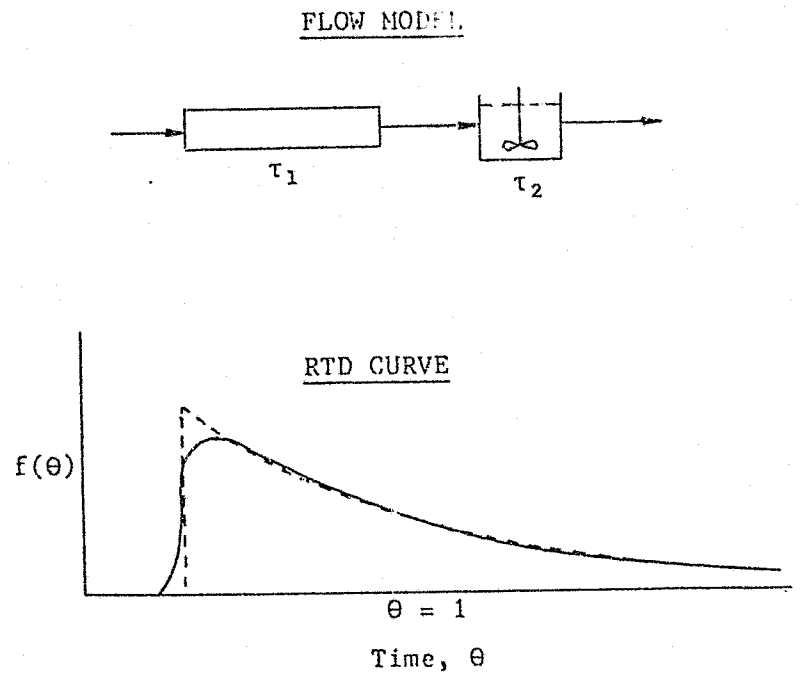


FIGURE 6.16. PLUG FLOW AND CSTR IN SERIES MODEL

The two model parameters can easily be deduced from the slope of the logarithmic plots used in the exponential tail fitting (see section 3.3). The dimensionless RTD function is given by

$$f(\theta) = \begin{cases} 0 & \text{for } \theta < \tau_1 \\ (1/\tau_2)\ \exp[-(1/\tau_2)(\theta - \tau_1)] & \text{for } \theta > \tau_1 \end{cases}$$

Therefore, for $\theta > \tau_1$,

$$f(\theta) = [(1/\tau_2)\ \exp(\tau_1/\tau_2)]\ \exp(-\theta/\tau_2)$$
$$= c\ \exp(-b\theta)$$

b and c are given table 3.10. The values of τ_1 and τ_2 are given in table 6.8.

TABLE 6.8. PARAMETERS OF MODEL WITH PLUG FLOW AND CSTR IN SERIES

RUN	τ_2 (= 1/b)	τ_1 (= 1-τ_2)
1	0,84	0,16
2	0,78	0,22
3	0,78	0,22
4	0,84	0,16
5	0,79	0,21

The simple plug flow/CSTR model can be improved upon by allowing some backmixing in the plug flow region (e.g. gamma distribution) and an alternate bypass route around the CSTR - this results in the "bypass model". In reality then, region 1 of the model represents the turbulent jet of air issuing from the inlet, and region 2 is the remaining well-mixed region of the vessel. The bypass in the model allows for some of the air to short circuit from the point of jet impingement directly out. It must be noted however that the bypass model does not exclude the possibility of recycling in the vessel; it should be interpreted that the circulation in the region surrounding the central jet is so rapid that it can be represented by a CSTR.

The parameters resulting from a least-squares fit of the bypass model are given in Table 6.9.

TABLE 6.8. PARAMETERS OF MODEL WITH PLUG FLOW AND CSTR IN SERIES

RUN	τ_2 (= 1/b)	τ_1 (= 1-τ_2)
1	0,84	0,16
2	0,78	0,22
3	0,78	0,22
4	0,84	0,16
5	0,79	0,21

The simple plug flow/CSTR model can be improved upon by allowing some backmixing in the plug flow region (e.g. gamma distribution) and an alternate bypass route around the CSTR - this results in the "bypass model". In reality then, region 1 of the model represents the turbulent jet of air issuing from the inlet, and region 2 is the remaining well-mixed region of the vessel. The bypass in the model allows for some of the air to short circuit from the point of jet impingement directly out. It must be noted however that the bypass model does not exclude the possibility of recycling in the vessel; it should be interpreted that the circulation in the region surrounding the central jet is so rapid that it can be represented by a CSTR.

The parameters resulting from a least-squares fit of the bypass model are given in Table 6.9.

TABLE 6.9. PARAMETERS FOR LEAST-SQUARES FIT OF THE BYPASS MODEL

RUN	Independent Variables			$\sqrt{S^2/N}$	Dependent variables	
	p	τ_1	σ_1^2/τ_1^2		τ_2	V_1/V
1	0,853	0,244	0,087	0,0042	0,886	0,244
2	0,935	0,236	0,144	0,0025	0,817	0,236
3	0,968	0,183	0,043	0,0049	0,844	0,183
4	0,964	0,219	0,132	0,0032	0,810	0,219
5	0,973	0,199	0,112	0,0043	0,823	0,199

The high values for p show that almost the entire flow from region 1 enters region 2, with only about 4% bypass. The results for run 1 do not correspond with the others as the RTD curve of run 1 differed considerably from the rest and is not considered representative. The bypass model RTD curves were shown to fit the experimental data well in all cases (see figures 6.19 and 6.23).

The plots of the two primary parameters of the bypass model vs frequency (figures 6.24 and 6.25) show larger variations than was the case with the long reactor model. This is to be expected as the RTD curves contain more noise.

FIGURE 6.17. RECYCLE MODEL WITH GAMMA DISTRIBUTIONS IN BOTH LOOPS - SHORT REACTOR RUN 2.

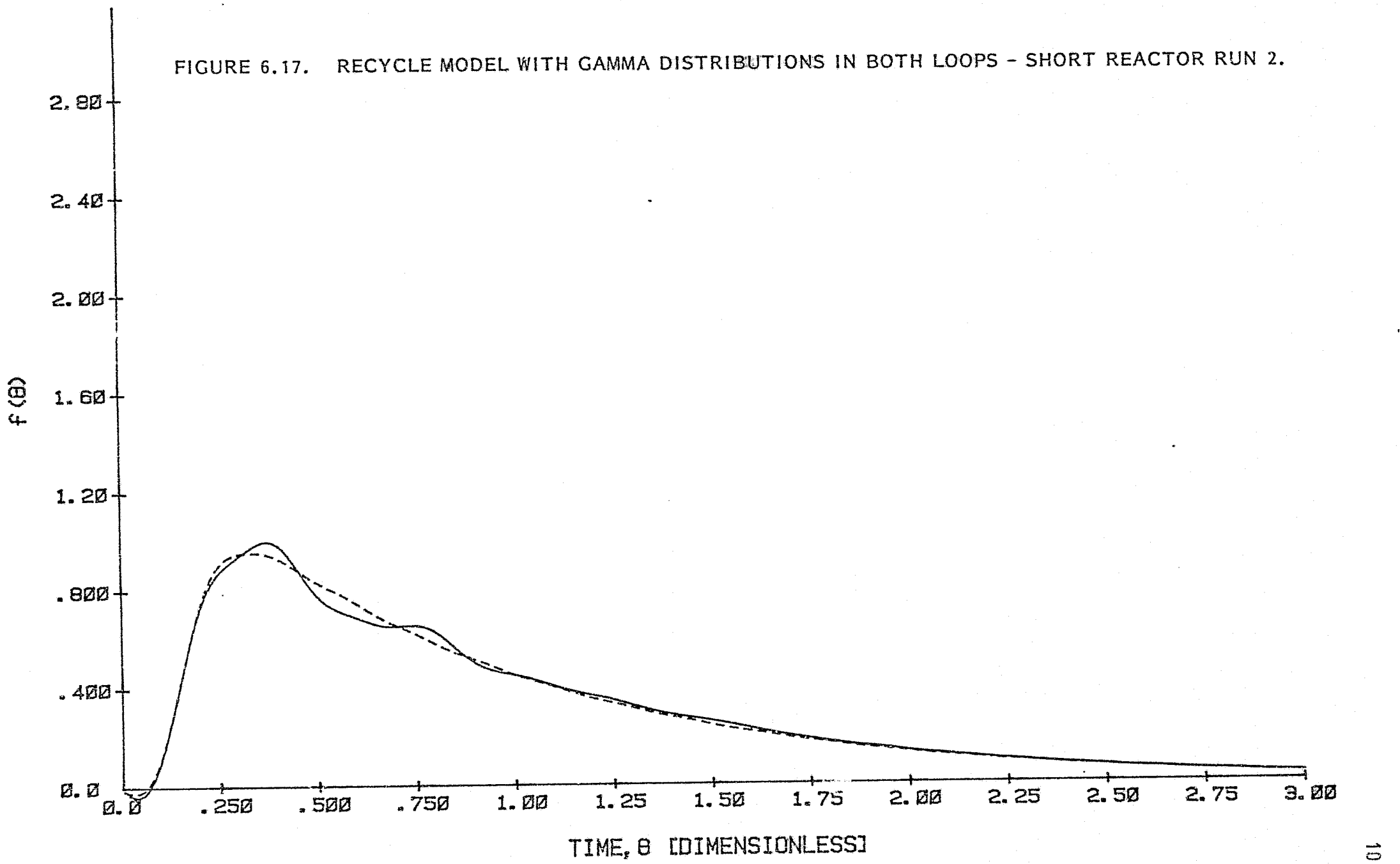


FIGURE 6.18. RECYCLE MODEL WITH A GAMMA DISTRIBUTION IN THE FORWARD LOOP ONLY - SHORT REACTOR RUN 2.

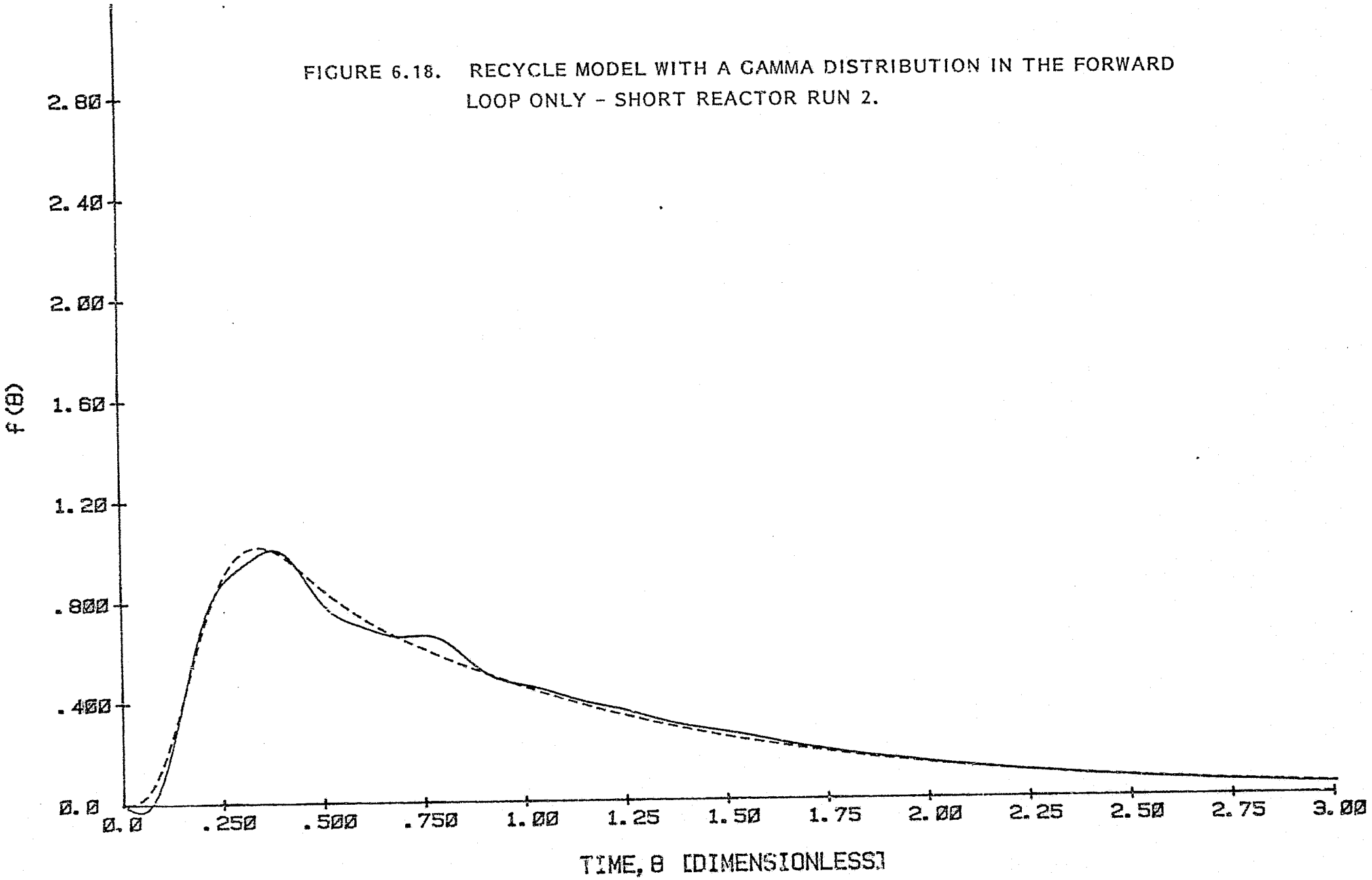


FIGURE 6.19. BYPASS MODEL - SHORT REACTOR RUN 2.

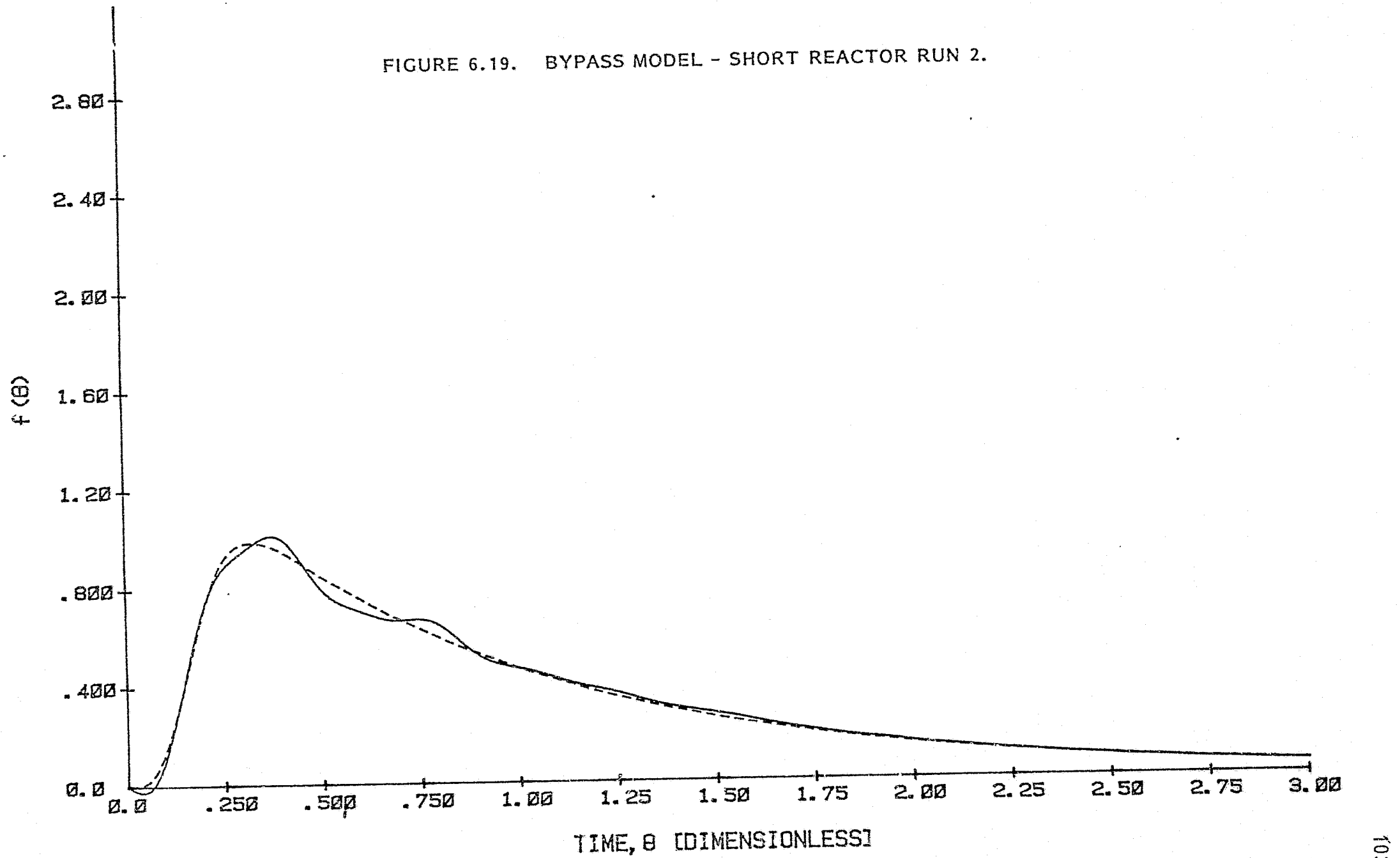


FIGURE 6.20. RECYCLE MODEL WITH GAMMA DISTRIBUTIONS IN BOTH LOOPS - SHORT REACTOR RUN 5.

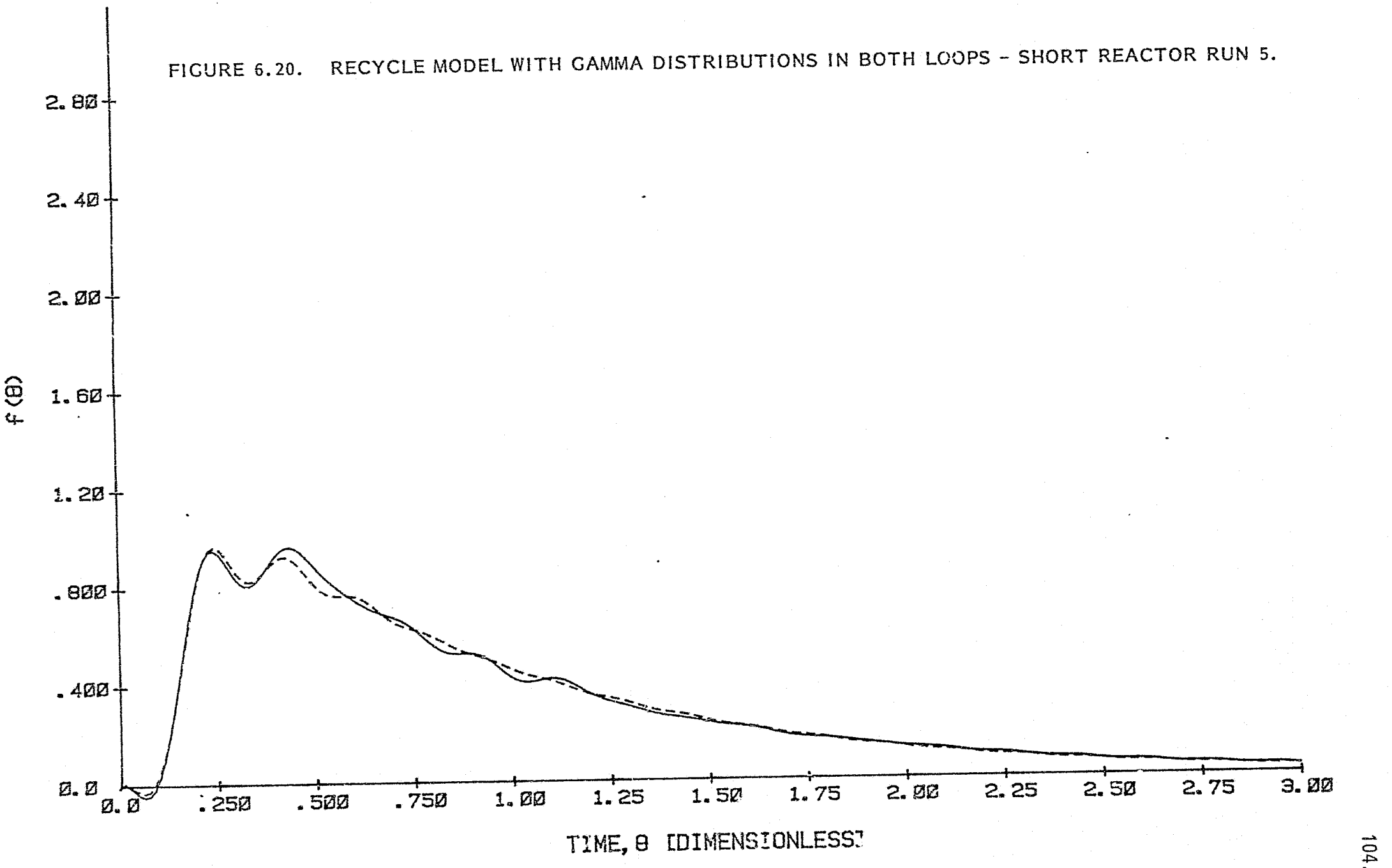


FIGURE 6.21. RECYCLE MODEL WITH A GAMMA DISTRIBUTION IN THE FORWARD LOOP ONLY - SHORT REACTOR RUN 5.

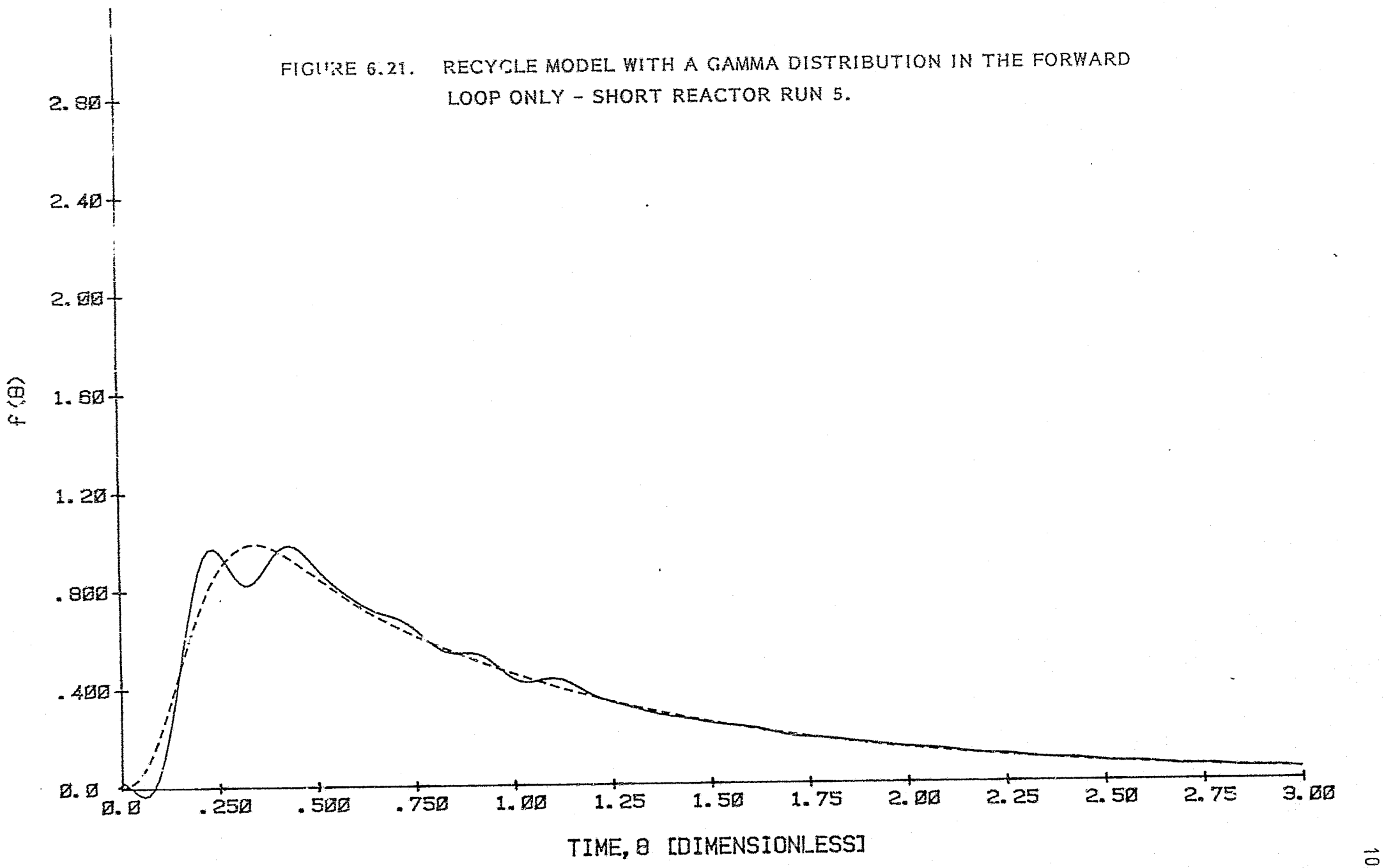
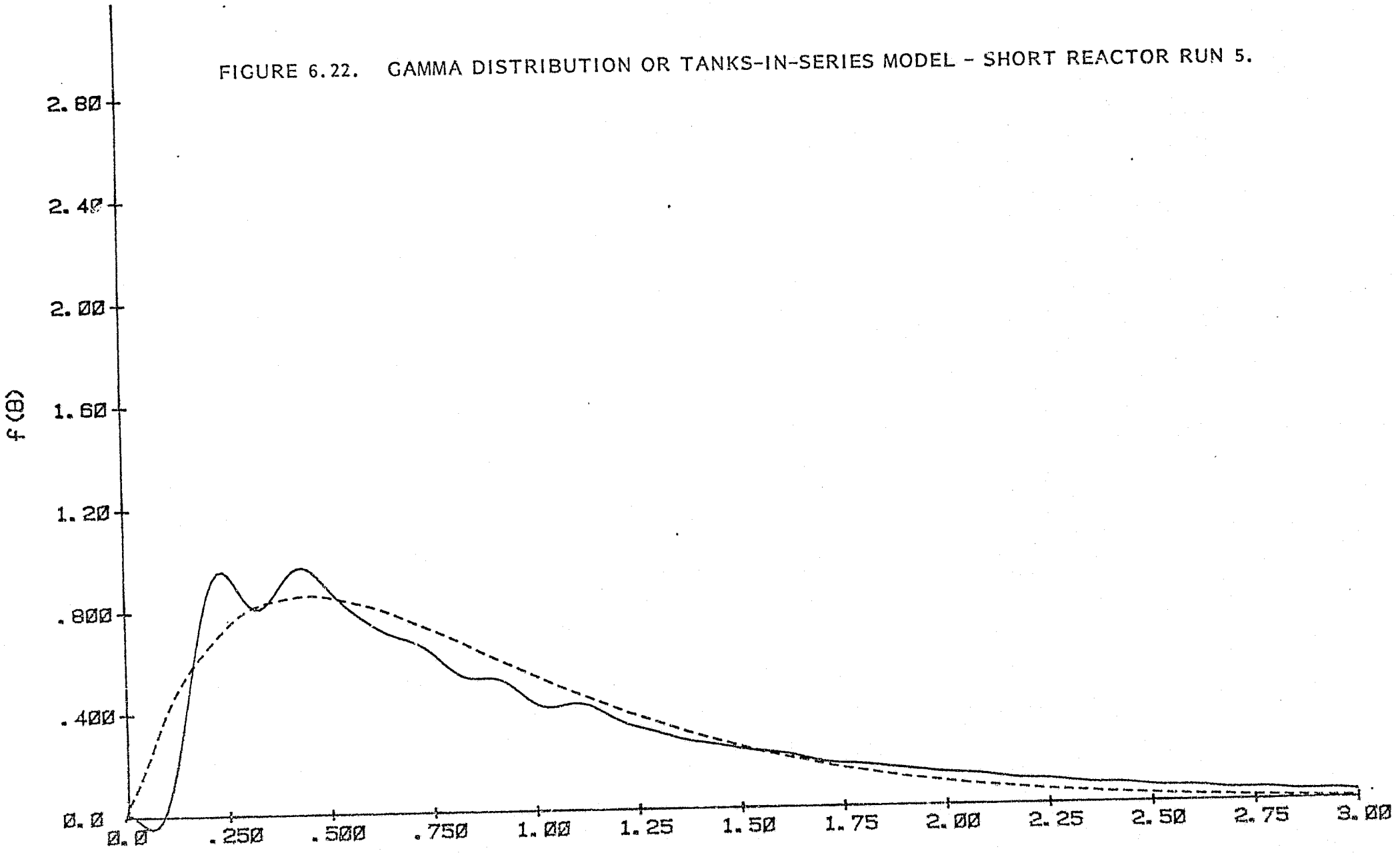


FIGURE 6.22. GAMMA DISTRIBUTION OR TANKS-IN-SERIES MODEL - SHORT REACTOR RUN 5.



Author Rabbitts M C
Name of thesis Analysis and modelling of residence time distribution in a high speed gas reactor 1982

PUBLISHER:
University of the Witwatersrand, Johannesburg
©2013

LEGAL NOTICES:

Copyright Notice: All materials on the University of the Witwatersrand, Johannesburg Library website are protected by South African copyright law and may not be distributed, transmitted, displayed, or otherwise published in any format, without the prior written permission of the copyright owner.

Disclaimer and Terms of Use: Provided that you maintain all copyright and other notices contained therein, you may download material (one machine readable copy and one print copy per page) for your personal and/or educational non-commercial use only.

The University of the Witwatersrand, Johannesburg, is not responsible for any errors or omissions and excludes any and all liability for any errors in or omissions from the information on the Library website.